Materials Science and Engineering R 64 (2009) 33–71

Contents lists available at ScienceDirect

Materials Science and Engineering R

journal homepage: www.elsevier.com/locate/mser

ZnO nanowire and nanobelt platform for nanotechnology

Zhong Lin Wang *

School of Materials Science and Engineering, Georgia Institute of Technology, Atlanta, GA 30332-0245, USA

ARTICLE INFO

Article history:
Available online 9 March 2009

Keywords:
ZnO
Nanowire
Nanobelts
Nanospring
Nanoring
Nanogenerator
Nanopiezotronics
Nanosensor
Nanolaser
LED
Solar cell

ABSTRACT

Semiconducting zinc oxide nanowires (NWs) and nanobelts (NBs) are a unique group of quasi-one-dimensional nanomaterial. This review mainly focuses on the rational synthesis, structure analysis, novel properties and unique applications of zinc oxide NWs and NBs in nanotechnology. First, we will discuss rational design of synthetic strategies and the synthesis of NWs via vapor phase and chemical growth approaches. Secondly, the vapor–solid process for synthesis of oxide based nanostructures will be described in details. We will illustrate the polar surface dominated growth phenomena, such as the formation of nanosprings, nanorings and nanohelices of single-crystal zinc oxide. Third, we will describe the unique and novel electrical, optoelectronic, field emission, and mechanical properties of individual NWs and NBs. Finally, we will illustrate some novel devices and applications made using NWs as ultra-sensitive chemical and biological nanosensors, solar cell, light emitting diodes, nanogenerators, and nano-piezotronic devices. ZnO is ideal for nanogenerators for converting nano-scale mechanical energy into electricity owing to its coupled piezoelectric and semiconductive properties. The devices designed based on this coupled characteristic are the family of piezotronics, which is a new and unique group of electronic components that are controlled by external forces/pressure.

Contents

* Tel.: +1 404 894 8008; fax: +1 404 385 3852.
E-mail address: zhong.wang@mse.gatech.edu.

0927-796X/$ – see front matter © 2009 Elsevier B.V. All rights reserved.
doi:10.1016/j.mser.2009.02.001

1. Introduction

There are three most representing one-dimensional (1D) nanostructures that are being actively studied in nanotechnology: carbon nanotubes [1–5], silicon nanowires [6–9], and ZnO nanowire/nanobelts [10–12]. ZnO is one of the few dominant nanomaterials for nanotechnology. Based on bibliometric data from information-services provider Thomson Reuters [13], the number of publications and the cross-referenced areas based on ZnO nanostructures are as large and as important as literature in quantum computing, carbon nanotube, semiconductor thin films, and dark matter. This review focuses specifically on the synthesis, properties, device fabrications and novel applications of ZnO nanowire and nanobelts.

ZnO, as an important semiconducting material, has a wide range of applications in optics, optoelectronics, sensors, actuators, energy, biomedical sciences and spintronics (Fig. 1) [14]. ZnO exhibit the most splendid and abundant configurations of nanostructures that one material can form. We plan to cover the following three main contents in this review. First, we will demonstrate rationally designed synthesis of ZnO nanowires (NWs) via a vapor–liquid–solid (VLS) or vapor–solid–solid growth process, and chemical approach. Secondly, the vapor–solid process for synthesis of oxide based nanostructures will be described in details with consideration of the formation of Zn-terminated or O-terminated surfaces. We will illustrate the polar surface dominated growth phenomena, such as the formation of nanosprings [15] and nanorings [16] and nanohelices [17]. Third, we will describe the

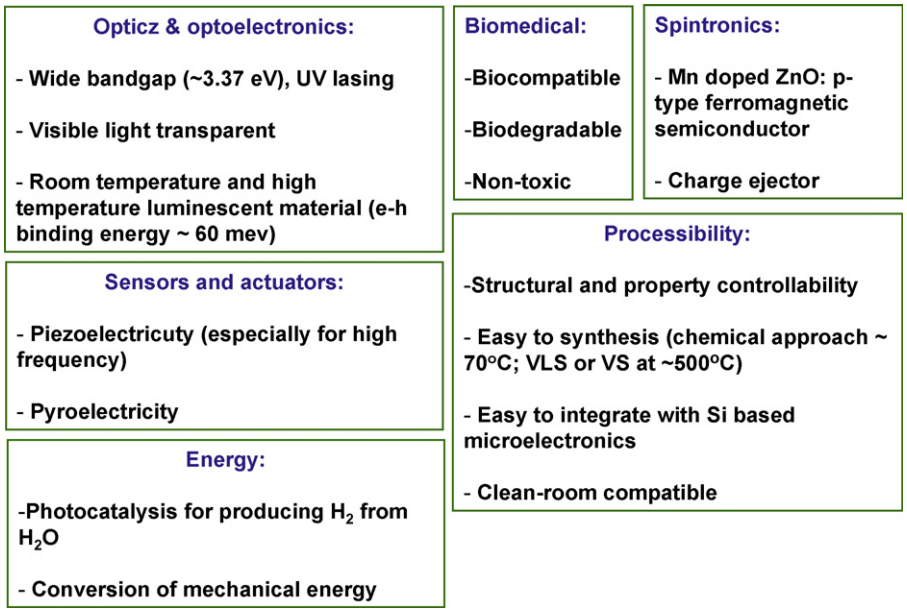

Fig. 1. A summary of applications and properties of ZnO.

unique and novel electrical, optoelectronic, field emission, mechanical and thermal properties of individual NWs. Finally, we will illustrate some novel devices and applications made using NWs as ultra-sensitive chemical and biological nanosensors, field emitters, nanogenerators, and nano-piezotronics. There are a few existing excellent reviews related to nanowire growth and characterization especially about ZnO [18–23]. This review will intend to cover the materials that were not comprehensively covered in these reviews.

2. Crystal structure of ZnO

Under conventional conditions, ZnO has the wurtzite structure, which has a hexagonal unit cell with space group *C*6*mc* and lattice parameters $a = 0.3296$, and $c = 0.52065$ nm. The oxygen anions and Zn cations form a tetrahedral unit. The entire structure lacks of central symmetry. The structure of ZnO can be simply described as a number of alternating planes composed of tetrahedrally coordinated O^{2-} and Zn^{2+} ions, stacked alternatively along the *c*-axis (Fig. 2a).

Although the entire unit cell of ZnO is neutral, the distribution of the cations and anions could take specific configuration as determined by crystallography, so that some surfaces can be terminated entirely with cations or anions, resulting in positively or negatively charged surfaces, called polar surfaces. The polar charge dominated surfaces can give some unique growth phenomena, as will be illustrated later. The most common polar surface is the basal plane. The oppositely charged ions produce positively charged Zn-(0 0 0 1) and negatively charged O-(0 0 0 $\bar{1}$) polar surfaces, resulting in a normal dipole moment and spontaneous polarization along the *c*-axis as well as a divergence in surface energy. To maintain a stable structure, the polar surfaces generally have facets or exhibit massive surface reconstructions, but ZnO ±(0 0 0 1) are exception, which are atomically flat, stable and without reconstruction [24,25]. Understanding the superior stability of the ZnO ±(0 0 0 1) polar surfaces is a forefront research in today's surface physics [26–29].

Another polar surface is the {0 1 $\bar{1}$ 1}. By projecting the structure along [1 $\bar{2}$ 1 0], as shown in Fig. 2b, beside the most typical ±(0 0 0 1) polar surfaces that are terminated with Zn and oxygen, respectively, ±(1 0 $\bar{1}$ 1) and ±(1 0 $\bar{1}$ $\bar{1}$) are also polar surfaces. The {1 0 $\bar{1}$ 1} type surfaces are not common for ZnO, but they have been observed in a nanohelical structure [30]. The charges on the polar surfaces are ionic charges, which are non-transferable and non-mobile. Because the interaction energy among the charges depends on the distribution of the charges, the structure is arranged in such a configuration to minimize the electrostatic energy. This is the main driving force for growing the polar surface dominated nanostructures.

Structurally, ZnO has three-types of fast growth directions: ⟨2 $\bar{1}$ $\bar{1}$ 0⟩ (±[2 $\bar{1}$ $\bar{1}$ 0], ±[$\bar{1}$ 2 $\bar{1}$ 0], ±[$\bar{1}$ $\bar{1}$ 2 0]); ⟨0 $\bar{1}$ $\bar{1}$ 0⟩ (±[0 1 $\bar{1}$ 0], ±[1 0 $\bar{1}$ 0], ±[1 $\bar{1}$ 0 0]); and ±[0 0 0 1]. Together with the polar surfaces due to atomic terminations, ZnO exhibits a wide range of novel structures that can be grown by tuning the growth rates along these directions. One of the most profound factors determining the morphology involves the relative surface activities of various growth facets under given conditions. Macroscopically, a crystal has different kinetic parameters for different crystal planes, which are emphasized under controlled growth conditions. Thus, after an initial period of nucleation and incubation, a crystallite will commonly develop into a three-dimensional object with well-defined, low-index crystallographic faces. Fig. 3a–c shows a few typical growth morphologies of 1D nanostructures for ZnO. These structures tend to maximize the areas of the {2 $\bar{1}$ $\bar{1}$ 0} and {0 1 $\bar{1}$ 0} facets because of lower energy. The morphology shown in Fig. 3d is dominated by the polar surfaces, which can be grown by introducing planar defects parallel to the polar surfaces [31]. Planar defects and twins are usually observed parallel to the (0 0 0 1) plane, but dislocations are rarely seen. A detailed analysis about the defects in ZnO nanostructures can be found from [32].

3. Synthesis of aligned nanowires

Growth of oxide nanostructures has mainly relied on physical vapor phase growth at relatively high temperature and chemical approach at low temperature. With consideration of a few existing reviews about the various growth techniques and their applications [20], we will skip the growth of randomly oriented nanowires but focus on aligned nanowire arrays that will be used for some unique applications.

3.1. Vapor–liquid–solid growth and vapor–solid–solid growth

Growth of aligned nanowires is important for applications such as lasers, light-emitting diodes and field effect transistors. Aligned growth of NWs can be achieved with the use of substrates and catalyst particles or seeds. The large-scale perfect vertical alignment of ZnO nanowires has been firstly demonstrated on

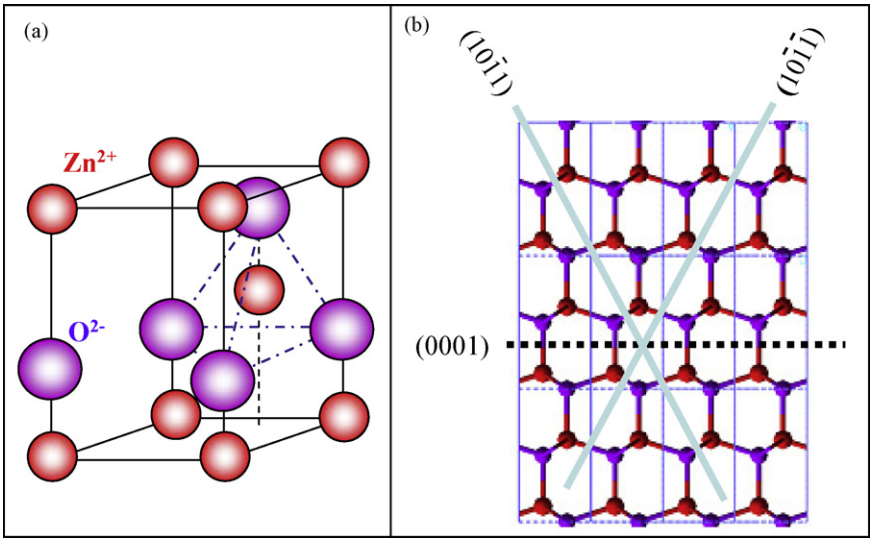

Fig. 2. (a) Wurtzite structure model of ZnO, which has non-central symmetry and piezoelectric effect. (b) The three types of facets of ZnO nanostructures: ±(0 0 0 1), {2 $\bar{1}$ $\bar{1}$ 0} and {0 1 $\bar{1}$ 0}.

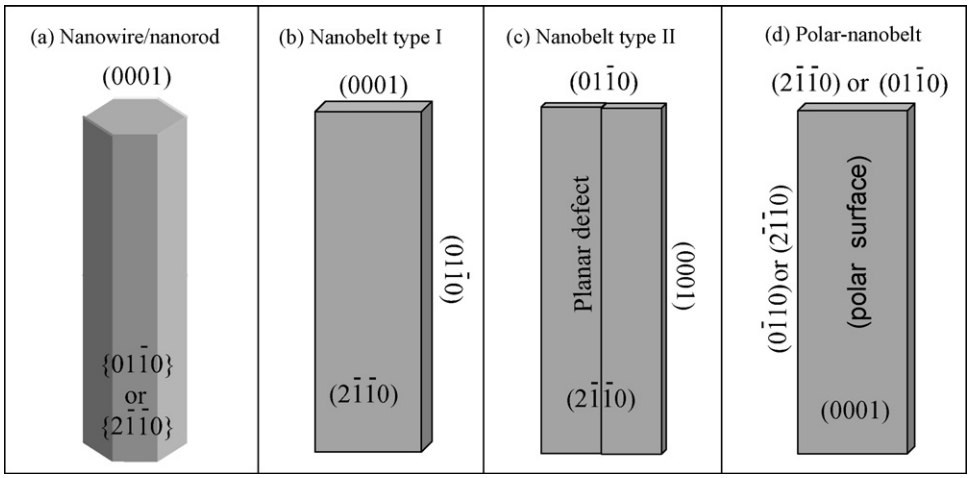

Fig. 3. Typical growth morphologies of one-dimensional ZnO nanostructures and the corresponding facets.

a-plane ((1 1 $\bar{2}$ 0) crystal surface) orientated single-crystal aluminum oxide (sapphire) substrates [33]. Gold nanoparticles were used as catalysts. The growth is initiated and guided by the Au particle and the epitaxial relationship between ZnO and Al_2O_3 leads to the alignment.

Unlike the normal vapor–liquid–solid (VLS) process, a moderate growth rate is required for the alignment since the catalyst needs to be molten, form alloy and precipitate step by step to achieve the epitaxial growth of ZnO on sapphire surface. Therefore, a relatively low growth temperature was always applied to reduce the vapor concentration. Mixing ZnO with carbon powder, which is so-called carbon-thermal evaporation, can reduce the vaporization temperature from 1300 °C to 900 °C,

$$\mathrm{ZnO(s)} + \mathrm{C(s)} \overset{900\,^{\circ}\mathrm{C}}{\longleftrightarrow} \mathrm{Zn}(v) + \mathrm{CO}(v) \quad (1)$$

The above reaction is reversible in a relatively lower temperature. So when the Zn vapor and CO were transferred to the substrate region, they could react and became back to ZnO, which could be absorbed by gold catalyst and eventually formed ZnO NWs through VLS process. The detailed growth conditions can be found in our previous publications.

The typical morphology of the aligned ZnO NWs on sapphire substrate is shown in Fig. 4a, a SEM image recorded at a 30° tilted view. All of the NWs are perpendicular to the substrate surface and the darker dot on the top of each nanowire is the gold catalyst. In this process, the growth spots were dictated by the existence of catalyst. If the applied catalyst was just a thin layer of gold, the distribution of the NWs would be random (Fig. 4a). The catalyst can also be pre-patterned by lithography or self-assembly techniques. For example, a two-dimensional, large-area, self-assembled and ordered monolayer of submicron polystyrene spheres was formed on sapphire substrate as a mask, through which a thin layer of gold was deposited. After etching away the spheres, a hexagonal network of gold layer was achieved (Fig. 4b) [34], catalyzed by which, the as-grown aligned NWs exhibited the same honeycomb-like distribution (Fig. 4c).

Aligned ZnO NWs have been successfully grown on sapphire, GaN, AlGaN and AlN substrates [35] through a VLS process, where the crystal structure of substrate is crucial for the orientation of NWs. Epitaxial relationship between the substrate surface and ZnO nanowires determines whether there will be an aligned growth and how well the alignment can be. The successful alignment of ZnO NWs on sapphire and nitride substrates is attributed to the very small lattice mismatches between the substrates and ZnO. In the case of sapphire, (1 1 $\bar{2}$ 0) plane orientated substrate is always used because the smallest lattice mismatch is along the *c*-axis of Al_2O_3 and *a*-axis of ZnO. The epitaxial relationship between ZnO NW and *a*-plane sapphire substrate are $(0\,0\,0\,1)_{ZnO}\|(1\,1\,\bar{2}\,0)_{Al_2O_3}$, $[1\,1\,\bar{2}\,0]_{ZnO}\|[0\,0\,0\,1]_{Al_2O_3}$. The lattice mismatch between $4[0\,1\,\bar{1}\,0]_{ZnO}$ ($4 \times 3.249 = 12.996$ Å) and $[0\,0\,0\,1]_{Al_2O_3}$ (12.99 Å) is almost zero, which confined the growth orientation of ZnO NWs. Nevertheless, since the (1 1 $\bar{2}$ 0) plane of Al_2O_3 is a rectangular lattice but the (0 0 0 1) plane of ZnO is a hexagonal lattice, this epitaxial relationship can only hold in one direction.

As for the nitride substrates, GaN, AlN and AlGaN all have the same wurtzite structure as ZnO. So, the deposited ZnO NWs are confined to their six equivalent ⟨0 1 $\bar{1}$ 0⟩ directions and only grow along the [0 0 0 1] direction, exactly following the substrate's crystal orientation, as shown in Fig. 4a. In this case, the epitaxial confinement is evenly distributed along the entire 2D atomic plane. As a result, even though the lattice mismatch becomes larger and larger from GaN (1.8%) to AlN (4.3%), the aligned growth was still kept very well and the possibility for ZnO nanorods to undergo lateral growth is rare (Fig. 4b). Therefore, *c*-plane oriented $Al_xGa_{1-x}N$ substrates are ideal for the growth of aligned ZnO NWs.

The growth direction is controlled by the epitaxial relationship between the substrate and NWs; while the aligning quality is controlled by many other factors. We have performed a systematic investigation on the growth conditions, which were attributed to three basic terms: chamber pressure, oxygen partial pressure [36] and thickness of catalyst layer [37].

From the experiment results, we found the oxygen partial pressure and the system total pressure played key roles in the growth of ZnO nanowires. With different oxygen volume percentage and different chamber pressure, the quality and growth behavior of the ZnO nanowires are strongly affected. We have carried out over 100 growth experiments under different growth conditions, which were designed to quantitatively define the best combination of the O_2 partial pressure and the chamber pressure for growth of aligned ZnO nanowires. For consistency, all of the samples were collected at the 880 °C temperature zone, which is 10 cm away from the source materials. The O_2 volume percentage in the chamber varied from 1 to 4 vol%, and the system pressure varied from 1.5 to 300 mbar.

The experimental results are summarized in Fig. 5, which is a "growth diagram" for the O_2 volume percentage in the chamber and system pressure, under which the optimum conditions for growing aligned ZnO nanowires are presented. The term of "growth diagram" used here is given a new meaning of representing the "road map" for controlled synthesis of nanowires.

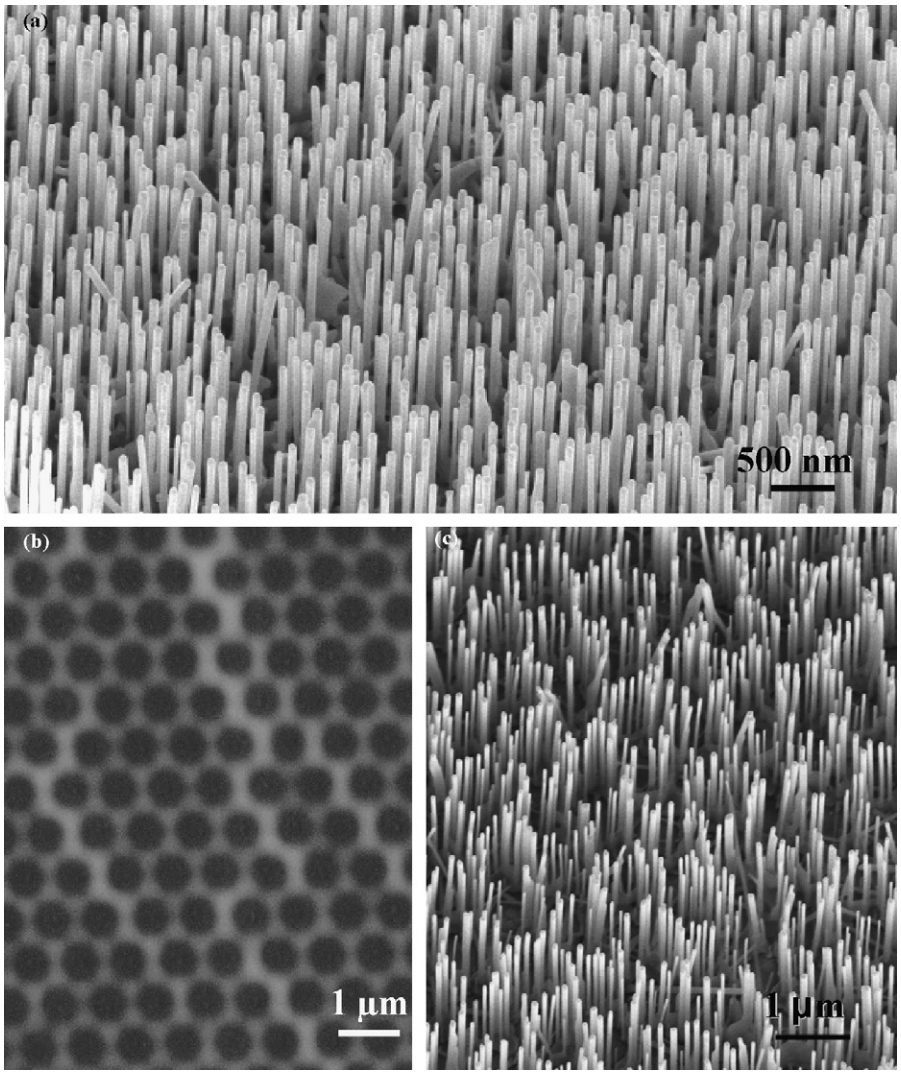

Fig. 4. (a) SEM image of aligned ZnO nanowires grown on sapphire substrate using a thin layer of gold as catalyst. (b) SEM images of gold catalyst patterns using PS sphere monolayer as mask. (c) SEM image of aligned ZnO nanorods grown with a honeycomb pattern. From [34].

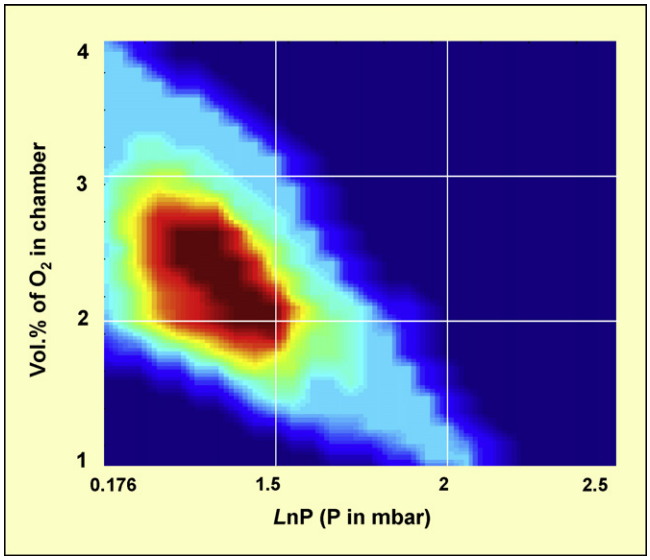

Fig. 5. "Phase diagram" that correlates oxygen volume percent in the growth chamber (e.g. partial pressure) and the growth chamber pressure (plotted in logarithm and *P* is in unit of mbar) for growing aligned ZnO nanowires. The point matrix was broadened and smoothed by MatLab to form a quasi-continuous phase diagram. From [36].

This phase diagram was determined for the data received from vapor phase growth. As shown in Fig. 5, the horizontal axis is the logarithm of the total chamber pressure; the vertical axis is the oxygen volume percentage in the chamber, and the quality of the grown ZnO nanowires is represented by different colors. The quality of the nanowires is characterized by their uniformity, density, length, and alignment. In the phase diagram, dark red represents the best growth condition, where a perfect alignment of ZnO nanowires with a high density and uniform length and thickness were achieved. The growth is good in the red area, where the density is lower and the nanowires are shorter. In the green and light blue area, the growth is poor, where only a little amount of short nanowires was found. No growth was found in the dark blue region. This phase diagram provides the road map for growing high quality aligned ZnO nanowires.

The growth of morphology of ZnO can be very diverse for several reasons. First, ZnO itself has many unique nanostructures, such as nanowires, nanobelts and nanorings, which are formed owing to the three quasi-sable $\{0\,0\,0\,1\}$, $\{1\,1\,\bar{2}\,0\}$ and $\{0\,1\,\bar{1}\,0\}$ surfaces and the corresponding growth directions. Second, Zn and ZnO both have hexagonal structure and can co-existence in a synthesis process. Zn can serve as catalyst that leads to the growth of ZnO nanostructure, or alternatively, oxidation of Zn can also form ZnO nanostructures [38]. Fig. 6 shows cylindrically arranged

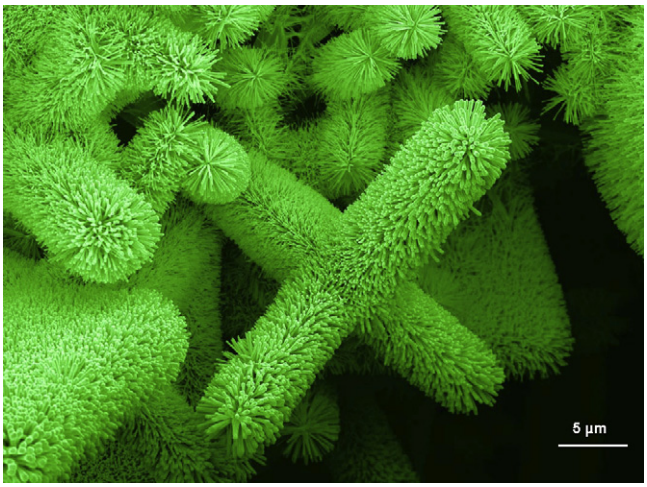

Fig. 6. Nanowire arrays grown by a vapor–solid process.

NWs grown by a vapor–solid process. The core of the cylinder fiber is likely made of Zn.

3.2. Hydrothermal based chemical approach

3.2.1. Method

Hydrothermal synthesis is a good approach for synthesis of ZnO nanowires with the use of ZnO seeds in the forms of thin films or nanoparticles [39,40]. We have recently reported a chemical approach for receiving density controlled growth of aligned ZnO NWs arrays without using ZnO seeds [41]. By adjusting the precursor concentration, the density of ZnO NW arrays could be controlled within one order of magnitude (number of ZnO NWs per 100 μm^2) with one NW growing from one spot site. This novel synthesis technique does not require ZnO seeds or external electrical field, and it can be carried out at low temperatures and large scale on any substrates regardless crystalline or amorphous.

For simplicity of description, we use Si substrate to describe the experimental procedure and to illustrate the effects of various experimental parameters on the growth. A piece of Si(1 0 0) wafer substrate was cleaned by a standard cleaning progress. First, the wafer was ultrasonicated consecutively in acetone, ethanol, IPA (isopropyl alcohol) and de-ionized water each for 10 min, then blew dry by dry nitrogen gas and then baked on hotplate at 200 °C for 5 min to get rid of any adsorbed moisture. Then, a 50 nm thick layer of Au was deposited on top of the Si wafer by magnetron plasma sputtering, which is expected to act as an "intermediate-layer" to assist the growth. Between the Si wafer and Au layer, 20 nm of Ti was deposited as an adhesion layer to buffer the large lattice mismatch between Si(1 0 0) surface with native oxide on and Au(1 1 1) surface and to improve the interface bonding. Then the substrate was annealed at 300 °C for 1 h. The next step is to prepare the nutrient solution. The nutrient solution was composed of a 1:1 ratio of zinc nitrate and hexamethylenetetramine (HMTA). The substrate was put face down at the top of the nutrient solution surface. Due to surface tension, the substrate could float at the top of the solution surface.

The annealing process helps the as-deposited Au layer to form a uniform crystalline thin layer on the surface of Si substrate, which is critical in the oriented growth of aligned ZnO NWs. The chemistry of the growth is well documented [42–44]. Zinc nitrate salt provides Zn^{2+} ions required for building up ZnO NWs. Water molecules in the solution provide O^{2-} ions. Even though the exact function of HMTA during the ZnO NW growth is still unclear, it is believed to act as a weak base, which would slowly hydrolyze in the water solution and gradually produce OH^-. This is critical in the synthesis process because, if the HMTA hydrolyzes very fast and produces a lot of OH^- in a short period of time, the Zn^{2+} ions in solution would precipitate out very quickly due to the high pH environment, which would have little contribution to the ZnO NW oriented growth, and eventually results in fast consumption of the nutrient and prohibits further growth of ZnO NWs.

$$(CH_2)_6N_4 + 6H_2O \leftrightarrow 4NH_3 + 6HCHO \quad (2)$$

$$NH_3 + H_2O \leftrightarrow NH_3{\cdot}H_2O \quad (3)$$

$$NH_3{\cdot}H_2O \leftrightarrow NH_4^+ + OH^- \quad (4)$$

$$Zn^{2+} + 2OH^- \leftrightarrow Zn(OH)_2 \quad (5)$$

$$Zn(OH)_2 \xrightarrow{\Delta} ZnO + H_2O \quad (6)$$

The growth process of ZnO NWs can be controlled through the five chemical reactions listed above. All of the five reactions are actually in equilibrium and can be controlled by adjusting the reaction parameters, such as precursor concentration, growth temperature and growth time, in order to push the reaction equilibrium forward or backward. In general, precursor concentration determines the NW density (Fig. 7a–c). Growth time and temperature control the ZnO NW morphology and aspect ratio.

The density of ZnO NWs on the substrate could be controlled by the initial concentration of the zinc salt and HMTA. To explore the relationship between the precursor concentration and the density of the ZnO NW arrays, a series of experiments were performed by varying the precursor concentration but keep the ratio constant between the zinc salt and HMTA. Experimental results show that the density of the NW arrays is closely related to the precursor concentration. Detailed analysis of the measured data is shown in Fig. 7d (red line). From 0.1 mM to 5 mM, the ZnO NWs density, defined as number of NWs per 100 μm^2, increases dramatically, possibly for the following reasons. Zinc chemical potential inside the solution body increases with zinc concentration. To balance the increased zinc chemical potential in solution, more nucleation sites on the substrate surface will be generated. So, the density of ZnO NWs increases. When further increasing the zinc concentration, the density of ZnO NWs remains approximately steady with a little tendency of decrease. The steady/saturated density may be understood from the nucleation and growth process. The NW density is decided by the number of nuclei formed at the very beginning of the growth, which continued to grow and form nanorods (shorter NWs). The arrival of more ions on the substrate may not initiate new nuclei at a later stage because of two possible reasons. One, with consideration the critical size required for a nucleus to grow into a crystal, no new nanorods would form if the sizes of the nuclei are smaller than the critical size. Second, due to the existence of the first group of grown nanorods, the newly arrived ions on the substrate have higher probability to reach the existing NWs rather than to the newly formed nuclei, thus, the size of the nuclei may not exceeds the critical size and they will eventually dissolve into the solution body. In such cases, a continuous increase in solution concentration may not increase the density of the NWs when its density is larger than the saturation density. This also explains why the grown NWs in our experiments have fairly uniform height. Even though the density of the ZnO NW remains steady at high precursor concentration level, the surface coverage percentage increases slightly due to the lateral growth of the NWs (Fig. 7d, blue line).

3.2.2. Patterned growth of vertically aligned nanowire array

To grow high-quality patterned ZnO NW arrays, we need an approach that can meet the following three requirements. First, the growth has to be at low temperature so that the NWs can be

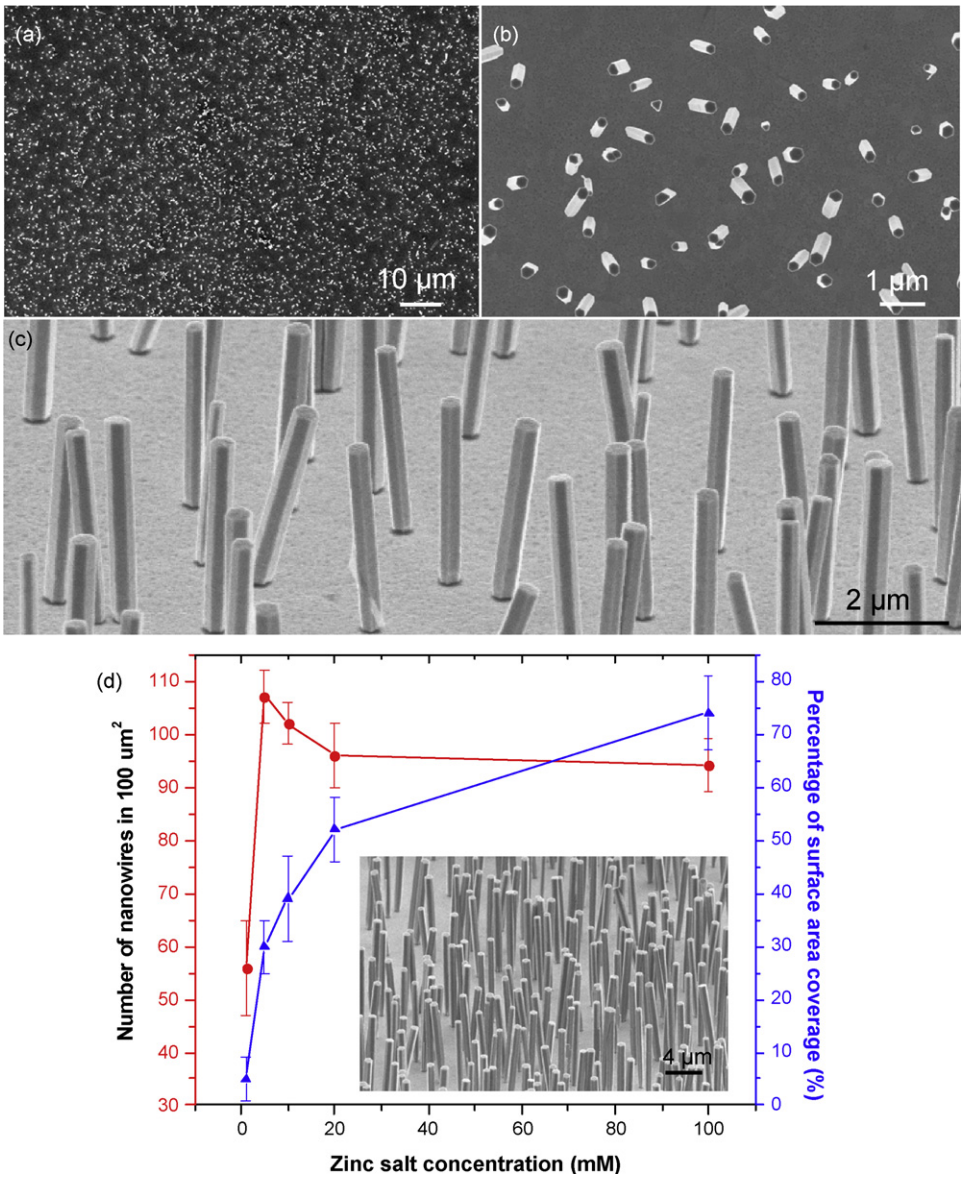

Fig. 7. A general view of as grown ZnO nanowire arrays at 5 mM, growing 24 h at 70 °C: (a) top view; (b) enlarged top view; (c) with a 60° tilt. (d) Density varied with concentration: plot of ZnO nanowire density in a 100 μm^2 area (red line) and plot of area percentage covered by ZnO nanowires (blue line). Each data point was obtained from 4 different areas. Inset is a typical image of ZnO nanowires grown at 5 mM. From [41]. (For interpretation of the references to color in this figure legend, the reader is referred to the web version of the article.)

integrated with general substrates. Second, the NWs have to be grown following a designed pattern, with a high degree control in size, orientation, dimensionality, uniformity and possibly shape. Finally, the catalyst may need to be eliminated for integrating with silicon based technology. Our approach is based on electron-beam lithography and a low temperature hydrothermal method to achieve patterned and aligned growth of ZnO NWs at <100 °C on general inorganic substrates, such as Si and GaN, without using a catalyst [45]. For the epitaxial growth, the Si doped n-type GaN substrate used here was fabricated by growing 2 μm thick GaN on *c*-plane sapphire by metal organic chemical vapor deposition. Then the GaN substrate was also cleaned by the standard cleaning progress.

The substrate was then spun on a 50 nm thick layer of PMMA. Then the substrate was baked on a hotplate at 180 °C for 2 min. The patterned was defined by an array of circle with 100 nm in diameter, and 1 μm in pitch. The dose used here was ranged from 300 $\mu C/cm^2$ to 600 $\mu C/cm^2$. After electron beam exposure, the substrate was developed in a mixture of 1:3 (in volume) ratio of IPA (isopropyl alcohol) and MIBK (methyl isobutyl ketone) for 1 min. No oxygen plasma treatment was performed.

Now the substrate is ready for hydrothermal growth of ZnO nanowire arrays. The nutrient solution used here was composed of 5 mmol/L 1:1 ratio of zinc nitrate and HMTA (hexamethylenetetramine). The patterned GaN substrate was put floating on top of the nutrient solution surface. The whole system was heated up to 70 °C for 24 h for growing multiple ZnO nanowires out of one single spot on Si wafer, and to 95 °C for 24 h for both one ZnO nanorod in one single spot on Si wafer on and GaN substrate. Fig. 8 shows the aligned ZnO NW array grown on a GaN on sapphire substrate. The as grown NWs have a complete control in size, dimension and orientation.

3.2.3. *Patterned growth of laterally aligned nanowire array*

The laterally aligned NWs were grown by using different materials to activate or inhibit the growth of nanowires [46]. Two materials are used here: ZnO seeds for the growth, and Cr layer for preventing the local growth. The first step for the growth is to

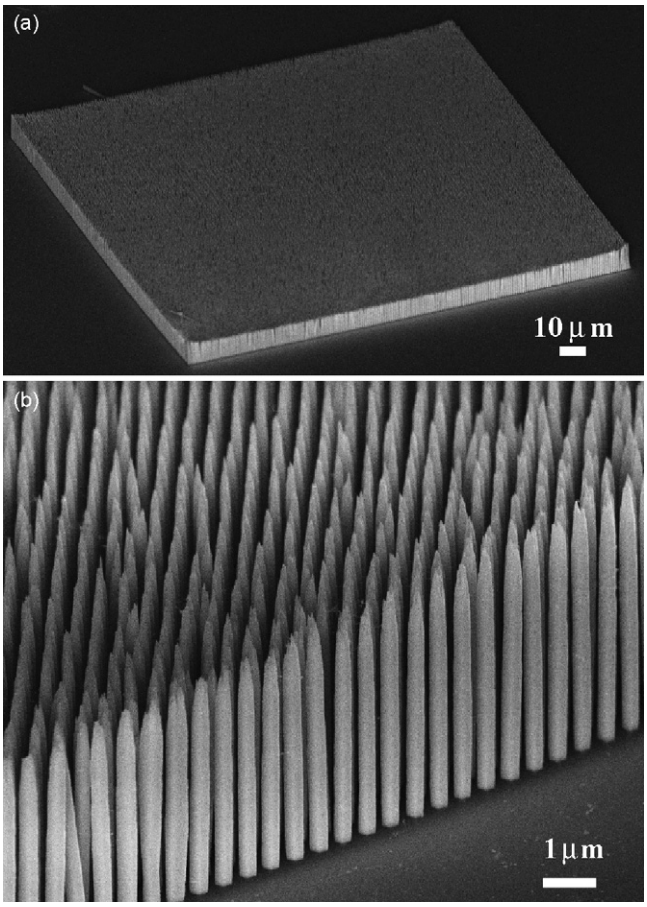

Fig. 8. (a) Low magnification and (b) high magnification SEM images of the ZnO NW arrays grown on a GaN substrate using a hydrothermal approach. From [45].

fabricate a ZnO strip pattern covered with Cr at top (Fig. 9a). A (1 0 0) Si wafer was firstly cleaned in sequence with HF acid solution, acetone, isopropyl alcohol and ethanol. A photoresist was spun coated on the substrate to get a uniform layer. Then a pattern was produced using optical lithography. ZnO strips with Cr on top were achieved after lifting-off with aceton. Finally, the substrate

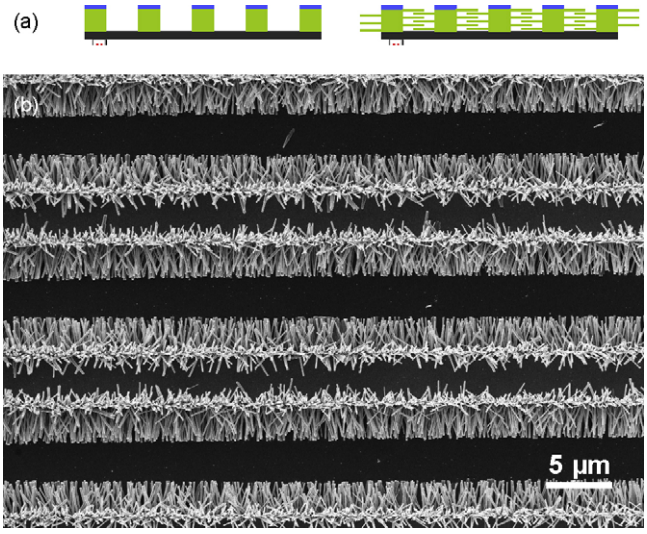

Fig. 9. (a) Schematic steps for growing patterned and laterally aligned ZnO NW arrays. (b) SEM image of ZnO nanowire arrays grown laterally on Si substrate. From [46].

was put into growth solution and aged for 12 h at 80 °C. To achieve uniform control over the growth rate by the concentration of the solution, the substrate was floated upside down on the solution surface with the patterned side facing downwards. Fig. 9b is the laterally grown ZnO NW arrays on Si substrate. It can be seen that ZnO NW arrays grew from the lateral sides of the pattern with a good alignment. More than 70% nanowires are parallel to the substrate. Only a small fraction of disordered ZnO nanowires grew at the edge of the pattern. ZnO NWs have a diameter less than 200 nm and a length of about 4 μm. Hexagonal cross-section of nanowires implies that *c*-axis of ZnO NW is along its length direction.

3.2.4. Competitive lateral and vertical growth

ZnO nanostructures can have three possible growth directions: [0 0 0 1], $\langle 1\,1\,\bar{2}\,0\rangle$ and $\langle 0\,1\,\bar{1}\,0\rangle$. By controlling the growth conditions, the growths along the three directions are competitive so that a complex growth configuration can be formed. Fig. 10 shows a structure that is the result of faster [0 0 0 1] growth with slower growth along the six fold symmetric $\langle 0\,1\,\bar{1}\,0\rangle$ growth. Nanowires are formed if the growth along $\langle 1\,1\,\bar{2}\,0\rangle$ and $\langle 0\,1\,\bar{1}\,0\rangle$ are inhibited.

4. Nanobelts and polar surface induced novel growth configurations

4.1. Vapor–solid synthesis of nanobelts

Vapor–solid growth process is a simple and effective method for the growth of oxide nanostructures without using catalyst [47]. There are two approach for vaporizing the source material, thermal vaporization and laser ablation. The thermal vaporization technique is a simple process, in which powder source material(s) is vaporized at elevating temperature and then the resultant vapor phase(s) condenses under certain conditions (temperature, pressure, atmosphere, substrate, etc.) to form the desired product(s). The morphology and phase structure of the synthesized product(s) depend on the source materials, growth temperature, temperature gradient, substrate, gas flow rate and pressure.

Thermal evaporation of ZnO powders (purity: 99.99%; melting point: 1975 °C) at 1400 °C resulted in ultra-long ZnO nanobelts (Fig. 11a). The as-synthesized oxide nanobelts are pure, structurally uniform, single crystalline and most of them free from dislocations. A ripple-like contrast appeared in the TEM image is due to strain resulted from the bending of the belt. Occasionally, some planar defects, such as twins and stacking faults are found, but there is no line defect. Point defects, such as oxygen vacancies, should be present, which greatly affect the transport properties of the NBs. The NBs have a rectangular-like cross-section with typical widths of 30–300 nm, width-to-thickness ratios of 5–10 and lengths of up to a few millimeters. High-resolution TEM (HRTEM) and electron diffraction studies show that the ZnO nanobelts are structurally uniform and single crystalline (Fig. 11b).

4.2. Nanospirals and nanosprings

Due to differences in surface energies among (0 0 0 1), $\{0\,1\,\bar{1}\,0\}$ and $\{2\,\bar{1}\,\bar{1}\,0\}$, freestanding nanobelts and nanowires of ZnO are usually dominated by the lower energy, non-polar surfaces such as $\{0\,1\,\bar{1}\,0\}$ and $\{2\,\bar{1}\,\bar{1}\,0\}$. Recently, by introducing doping, such as In and/or Li, ZnO nanobelts dominated by the (0 0 0 1) polar surfaces have been grown. The nanobelt grows along $[2\,\bar{1}\,\bar{1}\,0]$ (the *a*-axis), with its top/bottom large surface $\pm(0\,0\,0\,1)$ and the side surfaces $\pm(0\,1\,\bar{1}\,0)$. Due to the small thickness of 5–20 nm and large aspect ratio of ~1:4, the flexibility and toughness of the nanobelts are extremely high. A polar surface dominated nanobelt can be

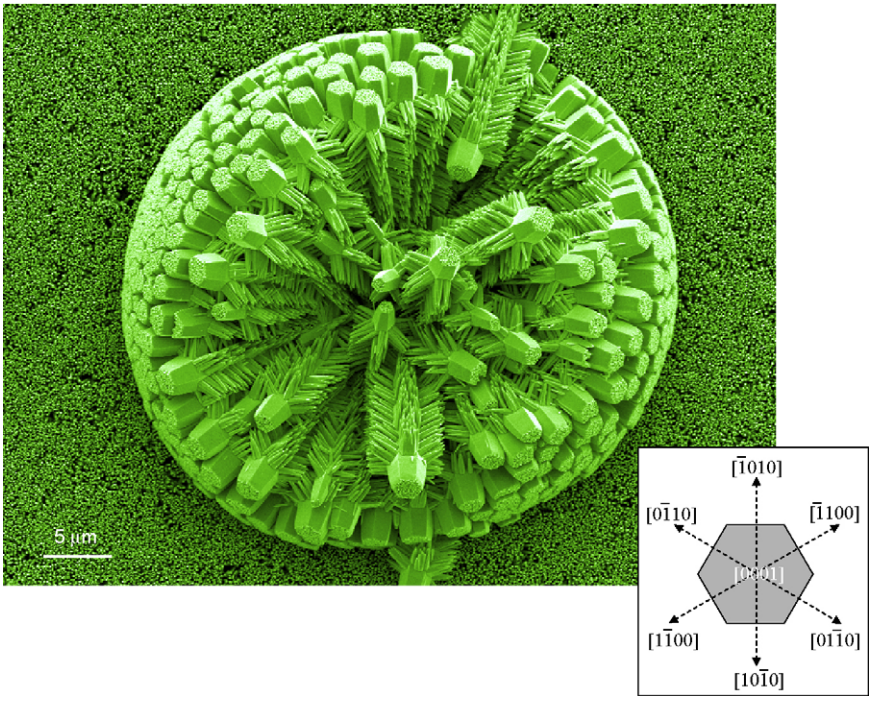

Fig. 10. Hierarchical nanostructure of ZnO (courtesy of Dr. Jun Liu, Pacific Northwestern National Lab).

approximated to be a "capacitor" with two parallel charged plates (Fig. 12a). The polar nanobelt tends to roll over into an enclosed ring to reduce the electrostatic energy (Fig. 12b) [12]. A spiral shape is also possible for reducing the electrostatic energy (Fig. 12c) [15]. The formation of the nanorings and nanohelixes can be understood from the nature of the polar surfaces. If the surface charges are uncompensated during the growth, the spontaneous polarization induces electrostatic energy due to the dipole moment, but rolling up to form a circular ring would minimize or neutralize the overall dipole moment, reducing the electrostatic energy. On the other hand, bending of the nanobelt produces elastic energy. The stable shape of the nanobelt is determined by the minimization of the total energy contributed by spontaneous polarization and elasticity. If the nanobelt is rolled loop-by-loop, the repulsive force between the charged surfaces stretches the nanospring, while the elastic deformation force pulls the loops together; the balance between the two forms the nanospring that has elasticity (Fig. 12d). The nanospring has a uniform shape with radius of ~500–800 nm and evenly distributed pitches. Each is made of a uniformly deformed single-crystal ZnO nanobelt.

4.3. Seamless nanorings

By adjusting the raw materials with the introduction of impurities, such as indium, we have synthesized a nanoring structure by the VS process (Fig. 13a) [16]. The as-synthesized sample is composed of many freestanding nanorings, with typical diameters ~1–4 μm, thin and wide shells of thicknesses ~10–30 nm. SEM images recorded at high-magnification clearly present the perfect circular shape of the complete rings, with uniform shape and flat surfaces. TEM image (Fig. 13b) indicates that the nanoring is a single-crystal entity with circular shape, although there is diffraction contrast due to non-uniform deformation along the circumference. The single-crystal structure referred here means a complete nanoring that is made of a single crystalline ribbon bent evenly at the curvature of the nanoring. Electron

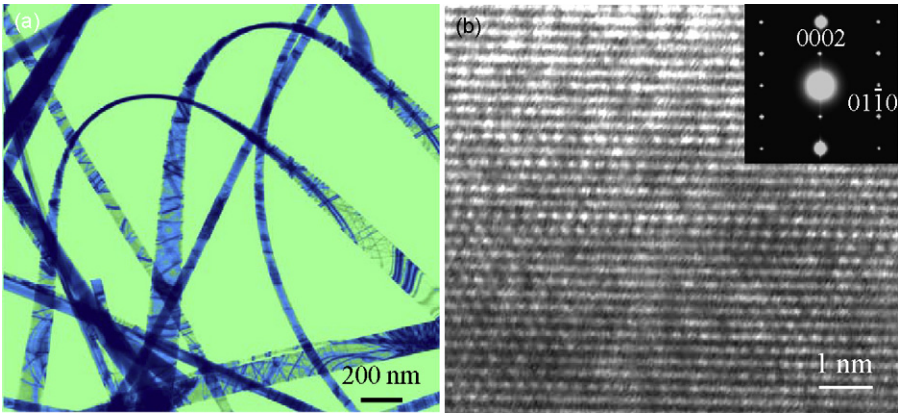

Fig. 11. TEM image of the as-synthesized ZnO nanobelts and a high-resolution TEM image recorded with the incident electron perpendicular to the top surface of the nanobelt. From [10].

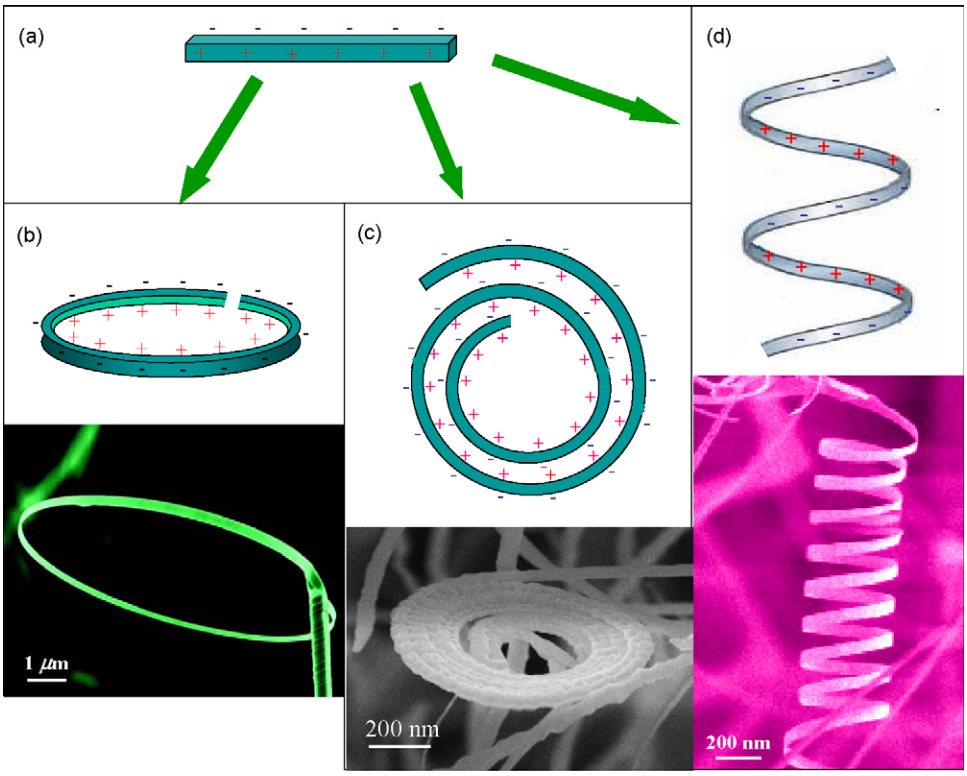

Fig. 12. Nanosprings of ZnO nanobelts. (a) A model of the polar surface dominated ZnO nanobelts. (b) Inward bending of the nanobelt results in the formation of a nanoring. (c) The formation of a nano-spiral. (d) The formation of a nanospring. From [12].

diffraction pattern recorded from the center of the nanoring shows that the radial direction of the nanoring is $[1\,\bar{2}\,1\,0]$, tangential direction $[1\,0\,\bar{1}\,0]$ and nanoring axis [0 0 0 1]. The nanoring is made of co-axial, uni-radius, epitaxial-coiling of a nanobelt. The trace of the coiling nanobelt is seen through the side of the nanoring. The interface between the loops is coherent, epitaxial and chemically bonded. The entire nanoring is a single crystal, although the quality of the crystallinity varies slightly across the width of the nanoring.

The growth of the nanoring structures can be understood from the polar surfaces of the ZnO nanobelt [16]. The polar-nanobelt, which is the building block of the nanoring, grows along $[1\,0\,\bar{1}\,0]$, with side surfaces $\pm(1\,\bar{2}\,1\,0)$ and top/bottom surfaces $\pm(0\,0\,0\,1)$, and have a typical width of ~15 nm and thickness ~10 nm. The nanobelt has polar charges on its top and bottom surfaces (Fig. 13c). If the surface charges are uncompensated during growth, the nanobelt may tend to fold itself as its length getting longer to minimize the area of the polar surface. One possible way is to interface the positively charged (0 0 0 1)-Zn plane (top surface) with the negatively charged (0 0 0 1)-O plane (bottom surface), resulting in neutralization of the local polar charges and the reduced surface area, thus, forming a loop with an overlapped end (Fig. 13c). The radius of the loop may be determined by the initial folding of the nanobelt at the initial growth, but the size of the loop cannot be too small to reduce the elasticdeformation energy. The total energy involved in the process comes from polar charges, surface area and elastic deformation. The long-range electrostatic interaction is likely to be the initial driving force for folding the nanobelt to form the first loop for the subsequent growth.

The presence of planar defect within the nanobelt is the key for leading to the fast growth of the nanobelt along $[1\,0\,\bar{1}\,0]$, because it lowers the energy in the wurtzite-structured lattice [31]. As the growth continues, the nanobelt may be naturally attracted onto the rim of the nanoring due to electrostatic interaction and extends parallel to the rim of the nanoring to neutralize the local polar charge and reduce the surface area, resulting in the formation of a self-coiled, co-axial, uni-radius, multi-looped nanoring structure (Fig. 13d). The self-assembly is spontaneous, which means that the self-coiling along the rim proceeds as the nanobelt grows. The reduced surface area and the formation of chemical bonds (short-range force) between the loops stabilize the coiled structure. The width of the nanoring increases as more loops winding along the nanoring axis, and all of them remain in the same crystal orientation. Since the growth was carried out in a temperature region of 200–400 °C, "epitaxial sintering" of the adjacent loops forms a single-crystal cylindrical nanoring structure, and the loops of the nanobelt are joined by chemical bonds as a single entity (Fig. 13e). A uni-radius and perfectly aligned coiling is energetically favorable because of the complete neutralization of the local polar charges inside the nanoring and the reduced surface area. Theoretical calculation shows consistent result.

The nanobelt that rolls over to form a nanoring usually has planar defects in the volume, which run along the entire length of the nanobelt. High-resolution TEM indicates that, besides the stacking fault inside the nanobelt, a stacking fault of a different type is formed at the interface between the adjacent loops, which is introduced to match the lattices of the Zn-terminated and the oxygen-terminated (0 0 0 1) polar surfaces [48] (Fig. 14a). The interface between the loops is coherent, epitaxial and chemically bonded. The details of the planar defects can be revealed by high-resolution transmission electron microscopy (Fig. 14b). The experimentally observed image can be quantitatively fitted by image simulation based on a proposed atomic model (Fig. 14c). A good match between the calculated and the observed images has been received.

4.4. Superlattice structured nanohelix

Helix is the most fundamental structural configuration of DNAs, proteins, and bio-functional groups, such as cytoplasm and periplasm [49]. We have reported a new and distinctive helical

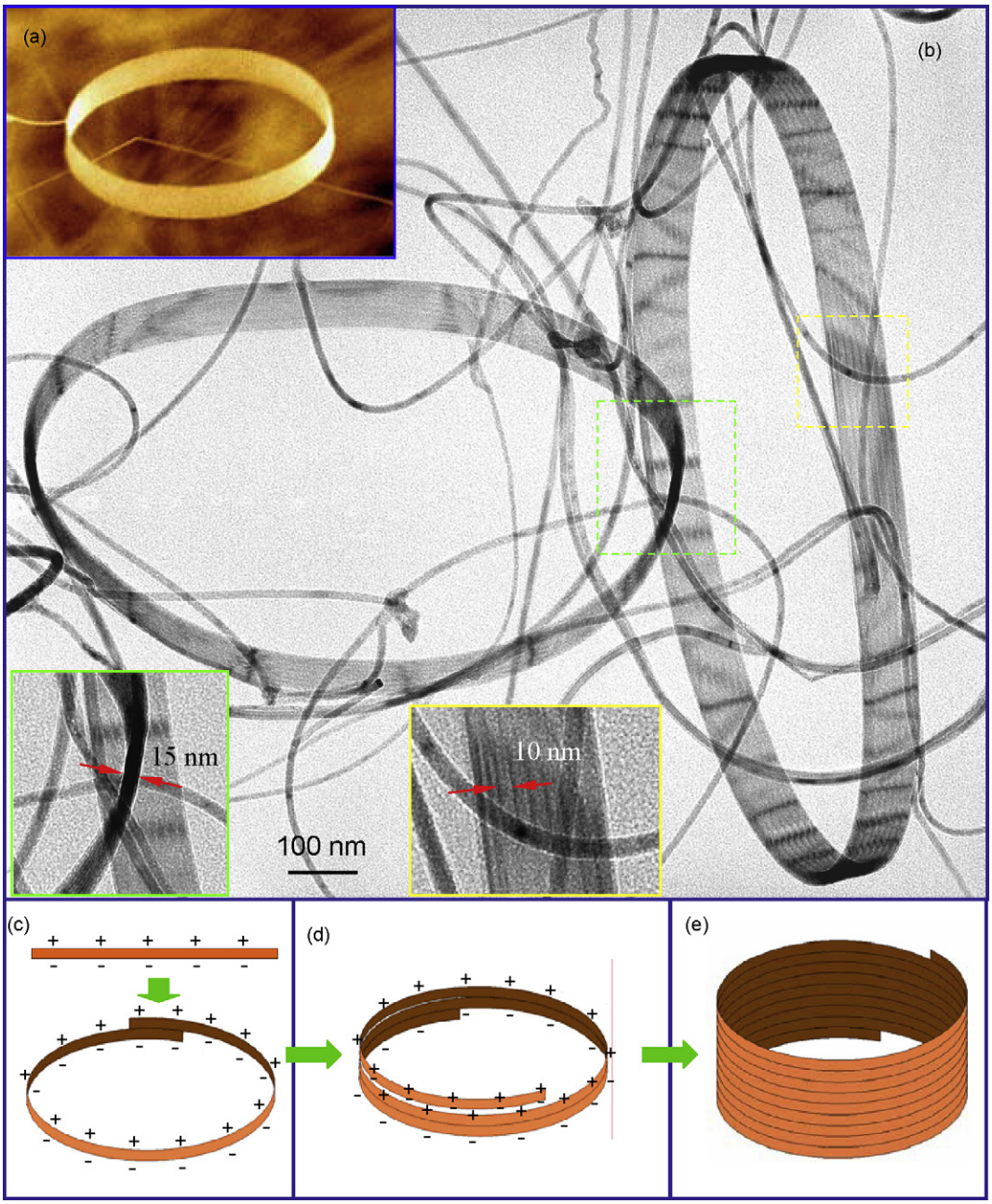

Fig. 13. (a) SEM image of single-crystal seamless nanoring of ZnO. (b) Low magnification TEM image of the ZnO rings and ZnO nanobelts. The nanobelts have uniform shape and their widths are ~15 nm, which is about the same as the thickness of the ring shell, as measured from the tilted image inserted in the figure. The thickness of the nanobelt composing the ring is measured to be 10 nm. (c–e) Proposed growth model showing the initiation and formation of the single-crystal nanoring via self-coiling of a polar nanobelt. The nanoring is initiated by folding a nanobelt into a loop with overlapped ends due to long-range electrostatic interaction among the polar charges; the short-range chemical bonding stabilizes the coiled ring structure; and the spontaneous self-coiling of the nanobelt is driven by minimizing the energy contributed by polar charges, surface area and elastic deformation. From [16].

structure of ZnO, made of a superlattice-structured nanobelt that is formed spontaneously in a solid–vapor growth process [17]. The ZnO nanohelixes were grown by a solid–vapor process. SEM images recorded at high-magnification clearly present the perfect shape and superior uniformity of the nanohelixes (Fig. 15a). The diameters of the nanohelixes are in the range of 300–700 nm, the widths of the nanobelts are 100–500 nm, but the pitch distances are rather spread from 500 to 2500 nm.

The nanobelt that coils into a nanohelix is composed of superlattice-structured stripes with a uniform periodicity of ~3.5 nm. High-resolution TEM clearly displays the superlattice-structure of the nanobelt with a periodic alternating arrangement of two types of stripes (Fig. 15b), which are oriented epitaxially in the following orientation relationship: Stripe I: growth direction $[1\,\bar{1}\,0\,0]$, top and bottom surfaces $\pm(0\,0\,0\,1)$ (polar-surfaces); Stripe II: growth direction $[2\,\bar{1}\,\bar{1}\,2]$, top and bottom surfaces $\pm(0\,1\,\bar{1}\,0)$ (non-polar-surfaces). The corresponding electron diffraction pattern of the nanobelt shows that the growth directions of the two types of stripes have a small rotation of $\alpha \approx 4^\circ$, indicating that the adjacent stripes rotate in the plane of the nanobelt for the same magnitude of the angle when forming the superlattice. The two stripes are coherent by aligning $(0\,\bar{1}\,1\,0)$ of Stripe I with $(0\,0\,0\,2)$ of Stripe II at a lattice mismatch of 2.9%, and $(\bar{2}\,1\,1\,0)$ of Stripe I with $(\bar{2}\,1\,1\,0)$) of Stripe II without lattice mismatch, thus, the interface energy is likely to be low.

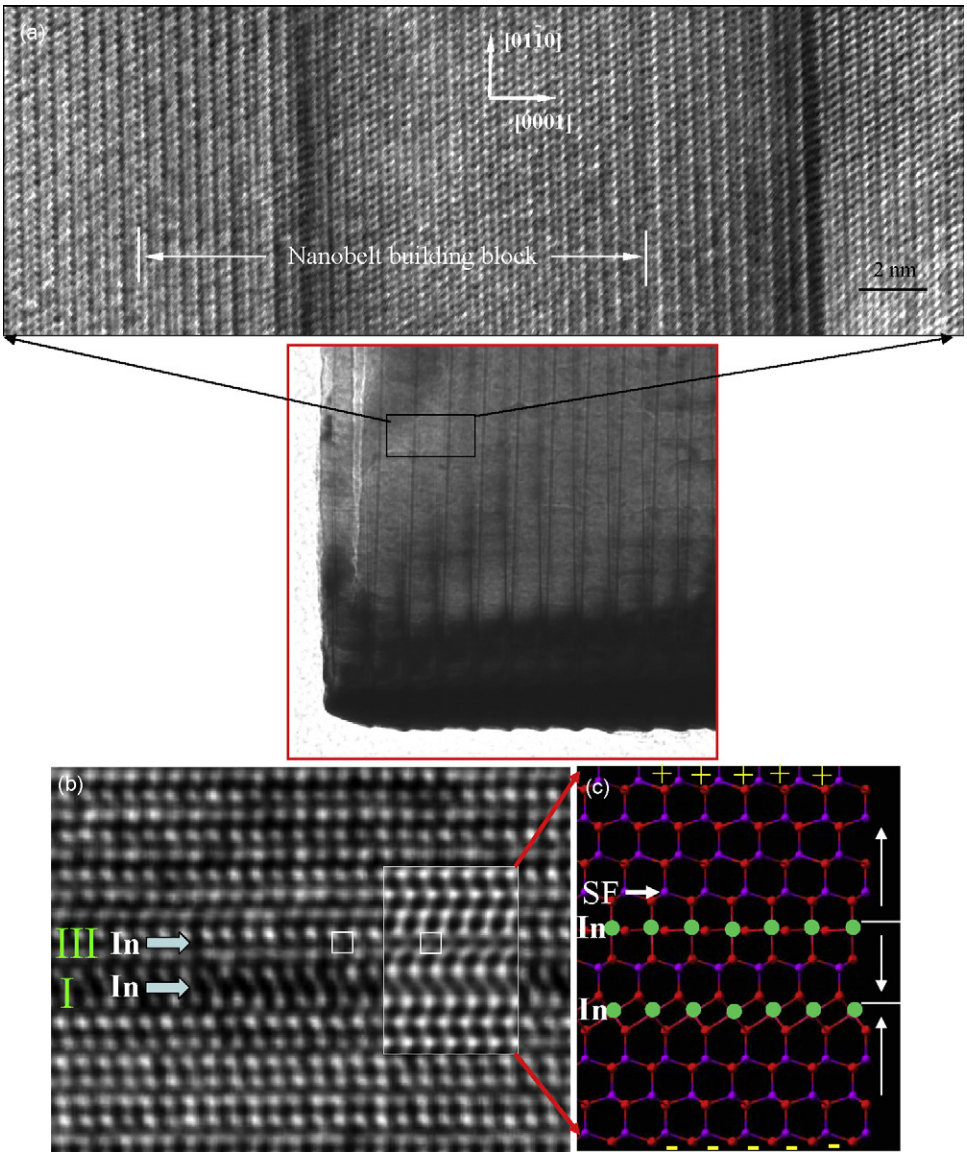

Fig. 14. (a) High-resolution TEM image recorded from the nanoring when the incident electron beam is parallel to the ring-plane, showing stacking faults inside the nanobelt and at the interface between the coiled loops. The width of the nanobelt is indicated. (b) HRTEM image recorded from a broken nanoring, the inset is a simulated image based on the model depicted in (c). Two inversion domain boundaries and a stacking fault have been identified in the image. From [16].

The initiation of the nanohelix is a direct result of superlattice formation. From the SEM image presented in Fig. 16a, a straight stiff-nanoribbon is directly connected to the starting point of a nanohelix. TEM examination shows that the joining point between the nanoribbon and the nanohelix is the place where the superlattice is created (Fig. 16b). The stiff-nanoribbon is a single crystal object dominated by large *c*-plane surfaces (Fig. 16c). The superlattice is formed spontaneously and abruptly across the entire width of the nanoribbon. An enlarged local area shows the co-existence and spontaneous formation of periodically arranged two alternating stripes at the transverse interface where the structural transformation occurred (Fig. 16d). At the transverse interface, the lattice mismatch between $(0\,\bar{1}\,1\,0)$ of the nanoribbon with $(0\,0\,0\,2)$ of Stripe II is 2.9%, and there is no mismatch between $(\bar{2}\,1\,1\,0)$ of the nanoribbon with $(\bar{2}\,1\,1\,0)$ of Stripe II, thus, the interface energy is likely to be low. Therefore, the interface mismatch edge dislocations with a Burgers vector of $[0\,\bar{1}\,1\,0]$, if exist, are expected to separate by 3.45 nm, which matches well to the periodicity of the superlattice (~3.5 nm). In fact, mismatch edge dislocations have been identified at the turning point between the nanoribbon and the superlattice, suggesting that the site of the mismatch dislocation could be the nucleation site of Stripe II. This observation suggests that the superior uniformity in periodicity of the superlattice may be resulted from the lattice mismatch as defined by crystal structure.

The formation of the nanohelix is a result of transforming a fully *c*-plane dominated stiff-nanoribbon (starting point) into a superlattice-structured, partially polar-surface dominated flexible nanobelt (middle section). The starting stiff-nanobelt is thick (~40 nm), straight and is dominated by $(0\,0\,0\,1)$ polar surfaces. If the width of the nanoribbon (see Fig. 17a) is rather large, the electrostatic energy of the polar-surfaces diverges with the extension of its length. A possible way of reducing the electrostatic energy is to transform the polar-surface into a non-polar-surface, provided the interface mismatch energy is reasonably low. A possible choice is to form superlattice-structured stripes almost parallel to the growth direction of the nanobelt, one of which preserves the same orientation of the stiff-nanoribbon with *c*-plane dominated surfaces (Stripe I), and the other has $(0\,1\,\bar{1}\,0)$ (*a*-plane) non-polar-surfaces (Stripe II). An introduction of argon gas

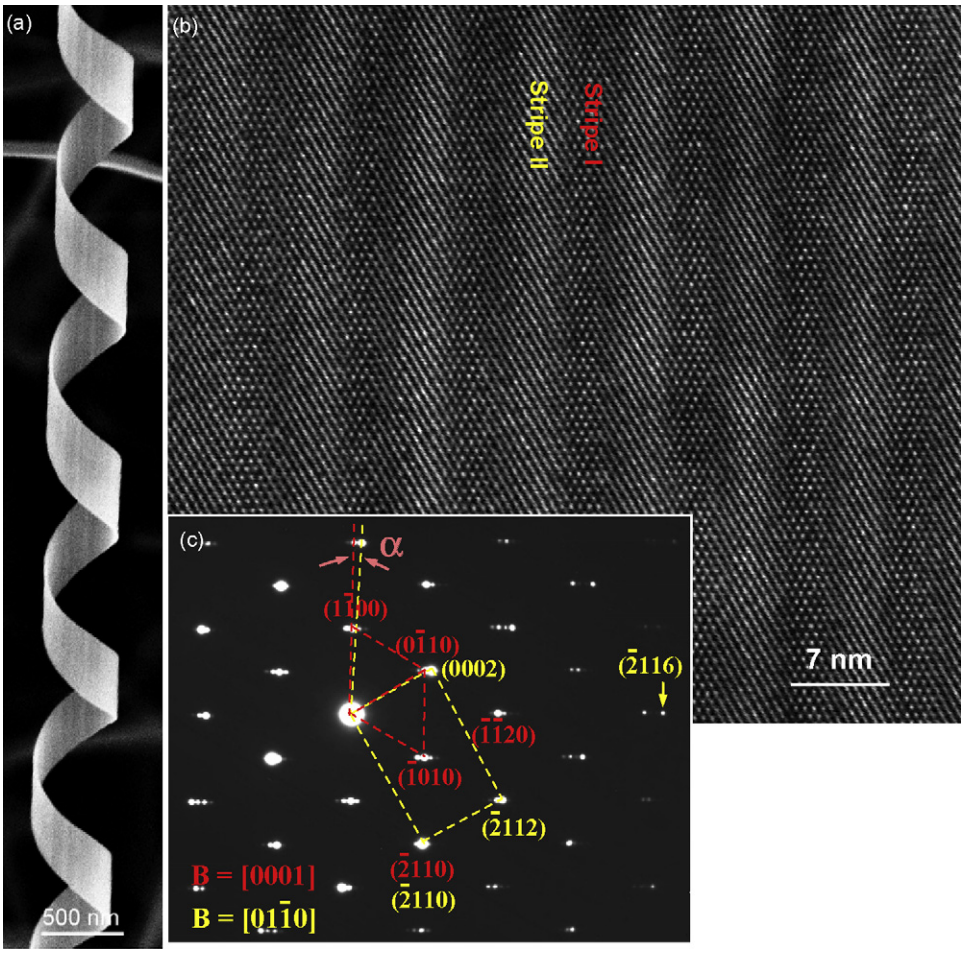

Fig. 15. ZnO nanohelixes. (a) Typical SEM images of a ZnO nanohelix. (b) High-magnification TEM image and (c) the corresponding electron diffraction pattern of a ZnO nanohelix with the incident beam perpendicular to the surface of the nanobelt, respectively, showing the lattice structure of the two alternating stripes. The diffraction pattern is composed of two sets of fundamental patterns: as labeled and indexed in red for Stripe I and yellow for Stripe II. A careful examination of the image indicate that the true interface between the stripes is not edge-on in reference to the incident electron beam, but at a relatively large angle. From [17]. (For interpretation of the references to color in this figure legend, the reader is referred to the web version of the article.)

at a later stage during the growth may be the initiation of superlattice formation. The two stripes have a coherent and epitaxial interface with small lattice mismatch and possibly low interface energy. A schematic top-view and cross-sectional view of the superlattice-structured nanobelt as well as the 3D structure of the nanohelix are given in Fig. 17c, where the *c*-axes (polar directions) across the nanobelt and the surface polar charges are indicated. The switching in *c*-axis may indicate the formation of piezoelectric domains. An important fact is that the width of the nanobelt increases after the structural transformation from a single-crystal *c*-plane dominated stiff-nanoribbon (in green) into a superlattice-structured flexible-nanobelt; the stripes may not be exactly parallel to the growth direction of the nanobelt, and a small in-plane rotation for an angle of α exists between the growth directions of the two adjacent stripes, which may induce the geometrical curvature required for rigidly twisting its shape. The polar charges remaining on the surfaces of Stripe I also help to bend the nanobelt into a ring structure especially with the reducing of the nanobelt thickness. Thus, the accumulation of rigid structure rotation/twisting across the width of the superlattice nanobelt and a continuous growth of the stripes along the length of the nanobelt may result in the formation of a helical structure, which could be left-handed or right-handed. The nanohelix ends by fully transforming into a non-polar surface dominated nanoribbon (in blue).

4.5. Deformation-free nanohelix

We have found a nanohelical structure that has radius as small as ~50 nm (Fig. 18a), much smaller than the nanospring as presented in Fig. 8 [30]. In order to understand this structure, the intrinsic crystal structure of the nanohelixes has been investigated. TEM image presents the uniform shape and contrast of the nanohelix (Fig. 18b). High-resolution TEM (HRTEM) imaging reveals that the nanohelix has an axial direction of [0 0 0 1], although the growth direction of the nanowire changes periodically along the length. Detailed HRTEM images from the regions labeled *c* and *d* in Fig. 18b are displayed in Fig. 18c and d, respectively, which show that the nanowire that constructs the nanohelix grows along [0 1 $\bar{1}$ 1]. Because the incident electron beam is parallel to [2 $\bar{1}$ $\bar{1}$ 0], the two side surfaces of the nanowire are $\pm$(0 1 $\bar{1}$ $\bar{2}$). No dislocations were found in the nanohelixes. It is important to note that the image recorded from the "twist" point of the nanohelix shows no change in crystal lattice (Fig. 18b), and the traces of the two sides are visible, indicating the non-twisted single-crystal structure of the entire nanohelix.

The nature of the $\pm${1 0 $\bar{1}$ $\bar{1}$} and $\pm$(0 1 $\bar{1}$ $\bar{2}$) planes can be understood from the atomic model of ZnO. By projecting the structure along [1 $\bar{2}$ 1 0], beside the most typical $\pm$(0 0 0 1) polar surfaces that are terminated with Zn and oxygen, respectively, {1 0 $\bar{1}$ $\bar{1}$} are also polar surfaces. From the structure information

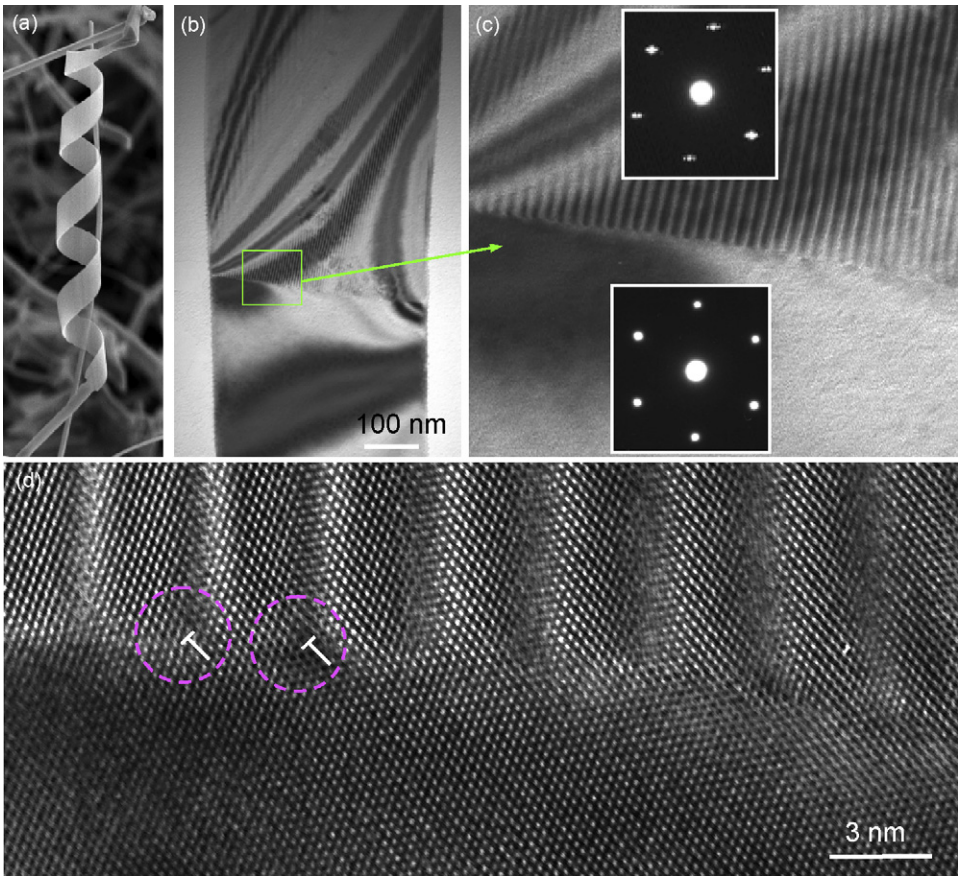

Fig. 16. Initiation and formation process of a nanohelix. (a) A low-magnification SEM image of a ZnO nanohelix showing its starting point and finishing end. (b) A low-magnification TEM image from the starting-point of a nanohelix, showing a distinct and sharp contrast change across a transverse line and an increase in nanobelt width. (c) An enlargement of the boxed area in (b) and the corresponding diffraction patterns from the single crystal region and the superlattice-structured region. The bottom-segment is a *c*-plane dominated single-crystal stiff-nanoribbon, while the top-segment is a superlattice-structured flexible-nanobelt. (d) High-magnification TEM image recorded from the interfacial region of the segments, showing a clear cutting-line from where the structural transformation occurs across the entire width of the nanobelt. Mismatch edge dislocations are identified in the circled regions directly linked to Stripe II. From [17].

provided by Fig. 10, the structure of the nanowire that self-coils to form the nanohelix can be constructed (Fig. 19). The nanowire grows along $[0\,1\,\bar{1}\,1]$, the two end surfaces being $\pm(0\,0\,0\,1)$, side surfaces being non-polar $\pm(0\,1\,\bar{1}\,\bar{2})$ (represented by yellow), Zn^{2+}-terminated $(1\,\bar{1}\,0\,1)$ and $(\bar{1}\,0\,1\,1)$ (represented by red), and O^{2-}-terminated $(\bar{1}\,1\,0\,\bar{1})$ and $(1\,0\,\bar{1}\,\bar{1})$ (represented by green) surfaces (see Fig. 19b and c).

The structure model presented in Fig. 11a is the basic building block/segment for constructing the nanohelix via a self-coiling process during the growth. Because there are a totally of six crystallographically equivalent $\langle 0\,\bar{1}\,1\,1\rangle$ directions: $[0\,1\,\bar{1}\,1]$, $[\bar{1}\,1\,0\,1]$, $[\bar{1}\,0\,1\,1]$, $[0\,\bar{1}\,1\,1]$, $[1\,\bar{1}\,0\,1]$, and $[1\,0\,\bar{1}\,1]$, and there is a 60° rotation between the two adjacent directions, thus, there are six equivalent orientations to stack the building block along the $[0\,0\,0\,1]$ axial direction without introducing deformation or twist. A realistic three-dimensional model of the nanohelix is presented in Fig. 19c, which is a stacking of the building blocks around the $[0\,0\,0\,1]$ axis following the sequences of the six directions described above. The interface between the two building blocks is perfectly coherent and the same piece of crystal, without mismatch, translation or twist.

The distribution of the polar charges is best seen through the top and bottom views of the model (Fig. 19c). If viewing the nanohelix from bottom-up, the non-polar $(0\,\bar{1}\,1\,2)$, Zn^{2+}-terminated $(1\,\bar{1}\,0\,1)$ and $(\bar{1}\,0\,1\,1)$ are seen. The six growth directions of the building blocks are indicated. It is important to point out that there is no deformation introduced in the hexagonal screw-coiling stacking process, thus, no dislocations are needed to accommodate deformation. If viewing the nanohelix from top-down, the non-polar $(0\,\bar{1}\,1\,2)$, and the O^{2-}-terminated $(\bar{1}\,1\,0\,\bar{1})$ and $(1\,0\,\bar{1}\,\bar{1})$ surfaces are seen.

4.6. Self-catalyzed growth structures

Asymmetric crystal structure of a material may introduce anisotropic growth structure. As we have shown for ZnO, the $(0\,0\,0\,1)$ surface is terminated with Zn, and the $(0\,0\,0\,\bar{1})$ surface is terminated with O. The former is catalytically active, while the latter is relatively inert, possibly resulting in anisotropic growth phenomena. In this section, we use the formations of nanocombs as an example to illustrate the self-catalysis effect.

"Comb-like" structures have been observed for wurtzite structured materials, such as ZnO [50], ZnS [51] and CdSe [52]. The comb structures (Fig. 20a and b) are ZnO and have the comb-teeth growing along $[0\,0\,0\,1]$, the top/bottom surfaces being $\pm(0\,1\,\bar{1}\,0)$, and side surfaces $\pm(2\,\bar{1}\,\bar{1}\,0)$. Using convergent beam electron diffraction (CBED) [53], which relies on dynamic scattering effect and is an effective technique for determining the polarity of wurtzite structure, we have found that the comb structure is an asymmetric growth along Zn-$[0\,0\,0\,1]$ (Fig. 20b) [54]. This conclusion is received by comparison the experimentally observed CBED pattern and the theoretically calculated pattern by matching the fine detailed structure features in the $(0\,0\,0\,2)$ and $(0\,0\,0\,\bar{2})$ diffraction disks (Fig. 20d and e). The positively charged

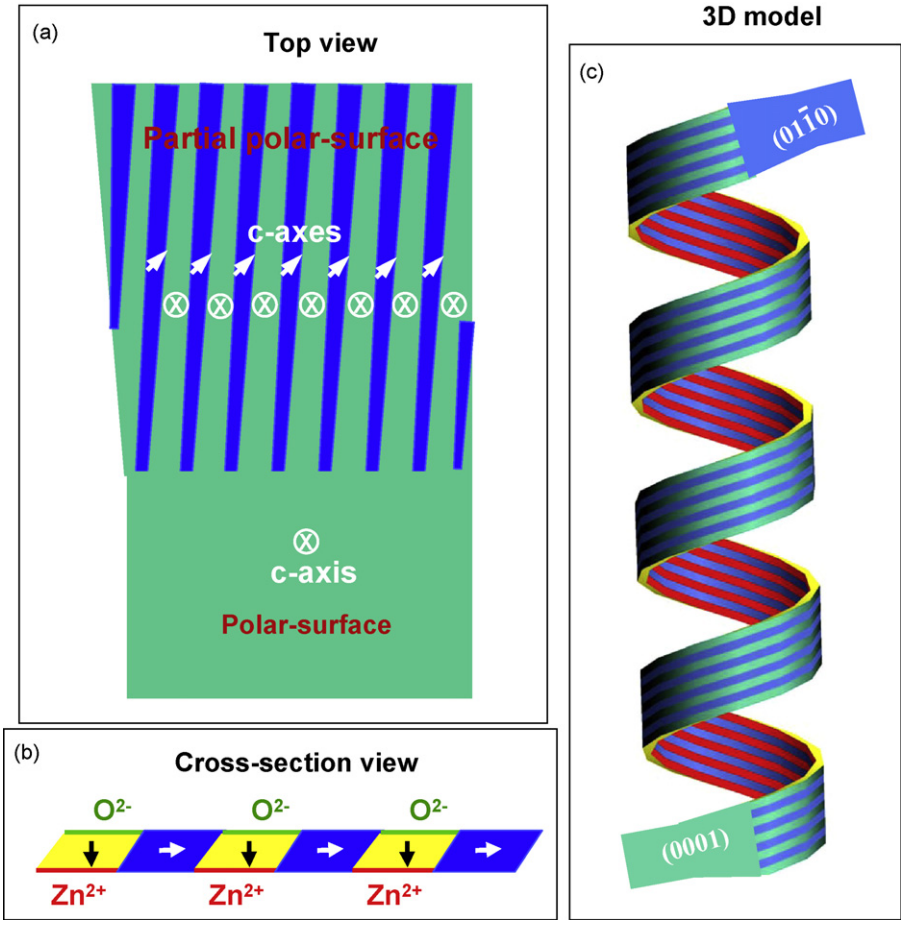

Fig. 17. (a and b) Schematic models showing the top-view and cross-sectional view of the nanobelt for illustrating the corresponding directions of the *c*-axes and the distribution of polar charges (in green for O^{2-} and red for Zn^{2+}) and non-polar surfaces (in blue). (c) A three-dimensional (3D) structure model of a nanohelix, showing its initiating point and finishing end. The periodicity of the superlattices may result in the formation of periodic piezoelectric domains. From [17].

Zn-(0 0 0 1) surface is chemically active and the negatively charged O-(0 0 0 $\bar{1}$) surface is relatively inert, resulting in a growth of long fingers along [0 0 0 1].

5. Fundamental properties of nanowires and nanobelts

5.1. Mechanical properties of nanobelts and nanowires

5.1.1. In situ resonance of a nanobelt

Atomic force microscopy (AFM) is powerful in characterizing the mechanical properties of nanostructures. Using the tip of an AFM to deflect a carbon nanotube, the displacement of the nanotube is directly related to the force acting on the tip, from which the Young's modulus of a carbon nanotube was measured [55]. Based on the electric-field-induced resonant excitation, an alternative technique has been developed for measuring the mechanical properties of individual nanowire-like structures by *in situ* transmission electron microscopy (TEM) [56,57]. Using this method, mechanical properties of carbon nanotubes [58], silicon nanowire [59] and silicon carbide–silica composite nanowires have been quantified.

To carry out the mechanical property measurements of a nanobelt, a specimen holder for a TEM was built for applying a voltage across a nanobelt and its counter electrode. Mechanical resonance can be induced if the applied frequency matches the natural resonance frequency of the nanobelt. Due to the mirror symmetry of the nanobelt (Fig. 21a), there are two distinct fundamental resonance frequencies corresponding to the vibration in the thickness and width directions, which are given from the classical elasticity theory as [60]

$$\nu_x = \frac{\beta_1^2 T}{4\pi L^2}\sqrt{\frac{E_x}{3\rho}}, \tag{7}$$

$$\nu_y = \frac{\beta_1^2 W}{4\pi L^2}\sqrt{\frac{E_y}{3\rho}}, \tag{8}$$

where $\beta_1 = 1.875$ for the first harmonic resonance; E_x and E_y are the bending modulus if the vibration is along *x*-axis (thickness direction) and *y*-direction (width direction), respectively; ρ is the density, L is the length, W is the width and T is the thickness of the nanobelt. The two modes are decoupled and they can be observed separately in experiments.

Changing the frequency of the applied voltage, we found two fundamental frequencies in two orthogonal directions transverse to the nanobelt [61]. Fig. 21b and c shows the harmonic resonance with the vibration planes nearly perpendicular and parallel to the viewing direction, respectively. For calculating the bending modulus, it is critical to accurately measure the fundamental resonance frequency (ν_1) and the dimensional sizes (L and T or W) of the investigated ZnO nanobelts. To determine ν_1, we have checked the stability of resonance frequency to ensure one end of nanobelt is tightly fixed, and the resonant excitation have been carefully checked around the half value of the resonance frequency. The specimen holder can be rotated about its axis so that the nanobelt can be aligned perpendicular to the electron

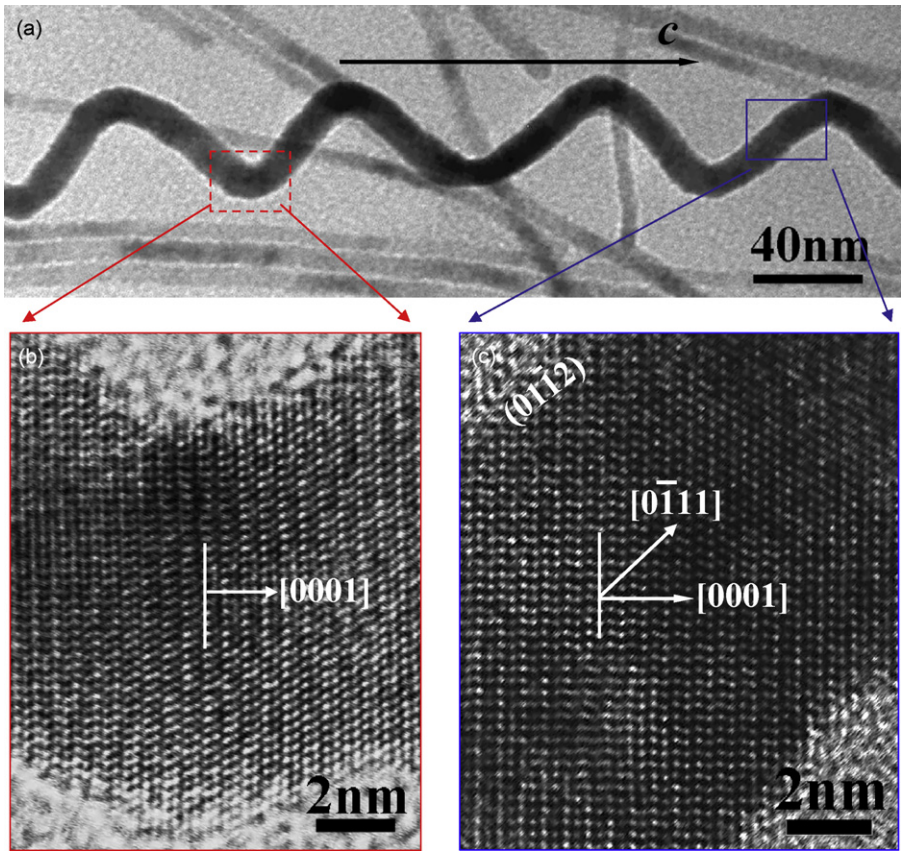

Fig. 18. (a) SEM image of a left-handed nanohelix. (b) A bright-field TEM image of a nanohelix. No significant strain contrast is found (apart from the overlap effect between the nanohelix and nanowires). (c and d) HRTEM images recorded from the c and d areas labeled in (a), respectively, showing the growth direction, side surfaces and dislocation-free volume. From [30].

beam, so the real length (L) of the nanobelt can be measured. The projection direction along the beam is determined by electron diffraction pattern, so that the true thickness and width can be determined because the normal direction of the nanobelt is [2 $\bar{1}$ $\bar{1}$ 0]. Based on the experimental data, the bending moduli of the ZnO nanobelts can be calculated using Eq. (7) or (8). The bending modulus of the ZnO nanobelts was ~52 GPa. Our experiments clearly shows that the nanobelt can be effective nanoresonators exhibiting two orthogonal resonance modes, which can be used as probes for SPM operated in tapping and scanning modes.

5.1.2. Mechanical behavior of aligned nanowire array

For the aligned ZnO NWs, we have recently demonstrated an AFM based technique for measuring the elastic properties of individual ZnO NW without destructing the specimen [62,63]. By simultaneously recording the topography and lateral force image in AFM contact mode when the AFM tip scans across the aligned nanowire arrays, the elastic modulus of individual NWs is determined. This technique allows a measurement of the mechanical properties of individual NWs of different lengths in an aligned array without destructing or manipulating the sample.

The principle for the AFM measurement is illustrated in Fig. 22a. In AFM contact mode, a constant normal force is kept between the tip and sample surface. The tip scans over the top of the ZnO NW and the tip's height is adjusted according to the surface morphology and local contacting force. Before the tip meets a NW, a small lateral force is observed (Fig. 22a-I). When the tip comes in contact with a NW, the lateral force increases almost linearly as the NW is elastically bent from its equilibrium position (Fig. 22a-II and III). At the largest bending position, as illustrated in Fig. 22d, the tip crosses the top of the NW, then the NW is released; the lateral force drops suddenly and reaches the ordinary level (Fig. 22a-V).

The elastic modulus is derived based on the following calculation. From the geometrical relationship illustrated in Fig. 22a-IV, when a vertical NW experiences a lateral force f parallel to the scanning direction, the force f can be expressed as:

$$f = 3EI\frac{x}{L^3}, \tag{9}$$

where E and I are the elastic modulus and momentum of inertia of the NW, x is the lateral displacement perpendicular to the NW, and L is the length of the NW. From Hook's law, the spring constant is $K = f/x$. For a ZnO NW with a hexagonal cross-section, its momentum of inertia is $I = (5(31/2)/16)a^4$, where a is the radius of the NW. Therefore, the elastic modulus is given by:

$$E = \frac{16L^3K}{15\sqrt{3}a^4}, \tag{10}$$

The displacement and the lateral force were determined from the topography image and the corresponding lateral force image, as shown in Fig. 22b and c, respectively. To ensure that the center of the conical tip touches the center of the NW as assumed in theoretical calculation, both curves were read from the center of the NW as indicated in the images by dashed lines. Taking a line scan across the middle point of a spot in the topography image, a curve for the scanner retracting distance versus the NW lateral displacement was obtained, as shown in Fig. 22d. Likewise, the maximum maximal lateral force for bending the NW was

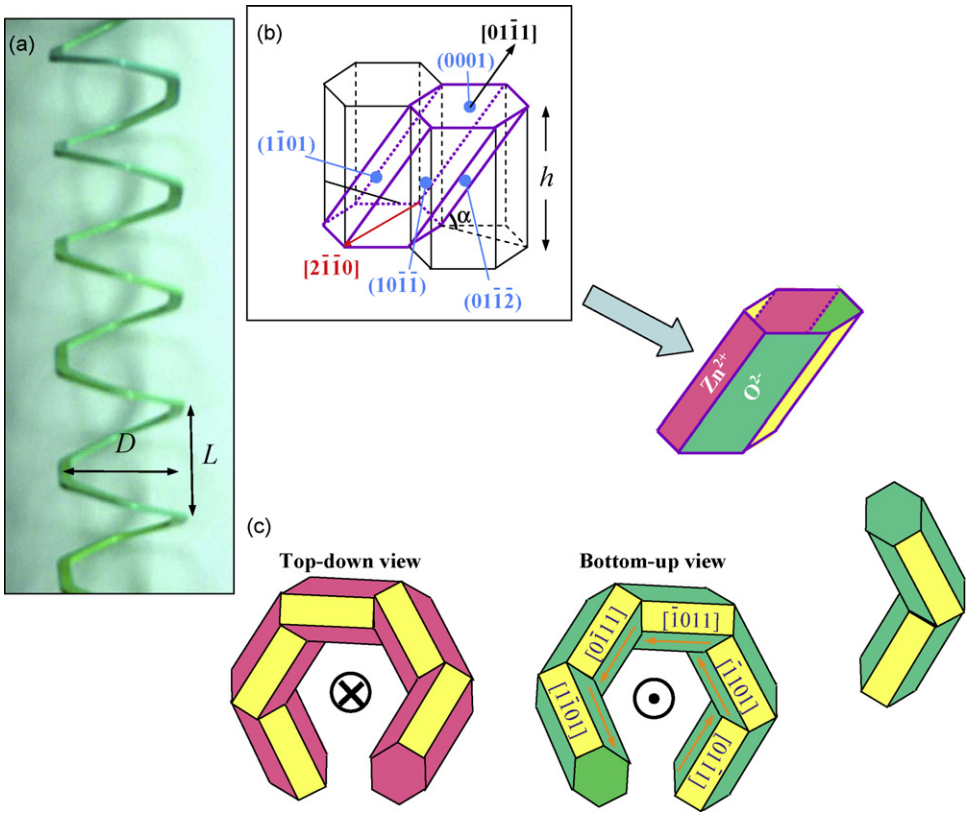

Fig. 19. (a) Structure of the deformation-free nanohelix. (b) The fundamental building block of the nanowire (in purple) for constructing the nanohelixes, and its growth direction and surfaces. The fundamental building block with Zn^{2+}-terminated polar surfaces (red) and O^{2-}-terminated surfaces (green) and the non-polar surfaces (yellow), bottom-up and top-down views of the nanohelical model. (c) A model of the nanohelical structure. From [30].

measured by taking a scanning profile at the corresponding line in the lateral force image. Combining the measured x_m and f_m from the two line profiles, the spring constant $K = f_m/x_m$ was obtained. For the ZnO nanowires grown on sapphire surfaces with an average diameter of 45 nm, the elastic modulus was determined to be 29 ± 8 GPa. This technique provided a direct observation on the mechanical properties of aligned NWs, which is of great importance for their applications in electronics, optoelectronics, sensors, and actuators.

5.1.3. Mechanical properties of a bridged nanobelt

Atomic force microscopy (AFM) is a common technique for characterizing the mechanical behavior of nanostructures [55,64]. One of the most important strategies is deforming a NW that is supported at the two ends using an AFM tip, which pushes the NW at its middle point. Quantifying the middle-point force–displacement curve gives the elastic modulus. The accuracy of this measurement is, however, limited by the size of the tip and the accuracy of positioning the AFM tip right at the middle of the 1D nanostructure due to the unavoidable hysteresis of the piezoceramic actuator of the AFM cantilever. We have demonstrated a new approach for quantifying the elastic deformation behavior of a NW by fitting the image profile measured using atomic force microscopy (AFM) in contact mode along the entire length of a bridged/suspended NB/NW/nanotube under different load forces (Fig. 23a) [63]. The profile images of the NB recorded the deformation of all of the points along its length under different applied forces (Fig. 23b). One profile could contain up to 650 points, and each point on the suspended portion of NB in the images can be regarded as a mechanical measurement. Consistently fitting the measured deformation profiles can uniquely determine if the measured data are best fit by either the clamped–clamped beam model (CCBM) or the free-free beam model (FFBM) without pre-assumption (Fig. 23c), and it eliminates the uncertainty in defining the central point of the suspended beam, thus, greatly increased the precision and reliability of the measurement for elastic modulus.

5.1.4. Elastic property of a nanohelix

The transverse spring constant of the nanohelix, a quantity for describing the stiffness of the nanohelix perpendicular to its axial direction, has been measured by AFM using the force–displacement (F–Z) curve. Through the static compression of a nanohelix lying on a silicon substrate with an AFM tip (Fig. 24a) and careful calibration of the sensitivity S of the photo-detector [65], which is the inverse of the slope of the F–Z curve, the transverse spring constant K_{Helix} of the nanohelix is measured to be: 3.9, 4.6, 4.5 an 5.3 N/m for the 1–4 cycles respectively. The measured K_{Helix} is close to the theoretically estimated, transverse spring constant of 4.2 N/m. Therefore, the elastic modulus E of the nanohelix is derived from the measured spring constant to be 42, 49, 48 and 57 GPa for the four cycles respectively [17], which agrees well with the elastic modulus measured for straight ZnO nanobelts by mechanical resonance using in situ TEM [66].

5.1.5. Super-elasticity of a nanohelix

The mechanical property of a ZnO nanohelix was studied using a nano-manipulator inside a focused ion beam microscope [67]. In the FIB system, the nanohelix was picked up by welding its one end using platinum (Pt) deposition onto the tip of a tungsten nano-probe (~100 nm in diameter at the tip), which was mounted on the nanomanipulator. The manipulation experiments were carried out via extending or compressing the nanohelix using the nano-probe tip. For the in situ manipulation inside the FIB system, the

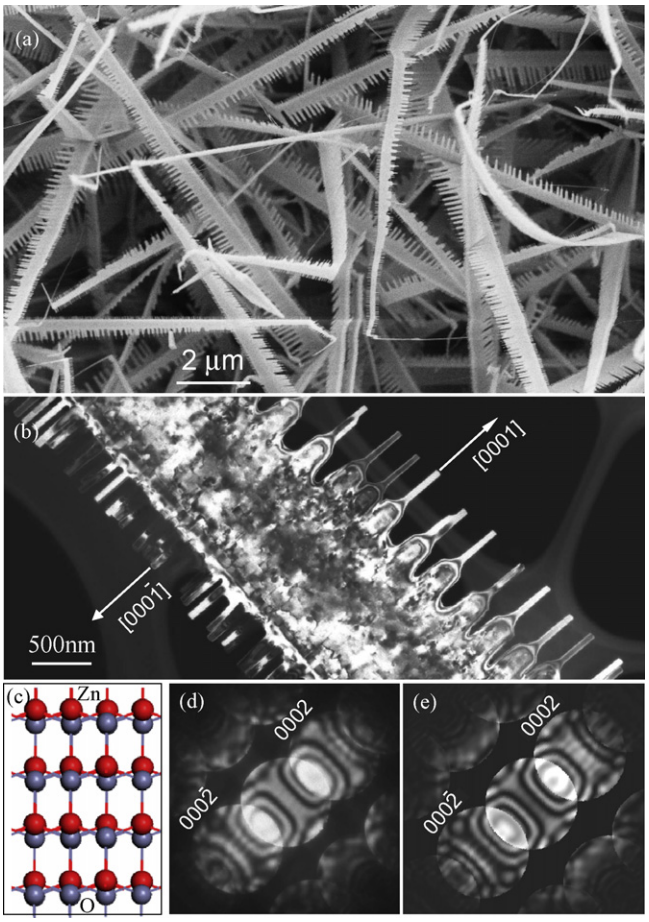

Fig. 20. Self-catalyzed growth of cation terminated polar surfaces. (a) SEM image of "comb-like" cantilever arrays of ZnO, which is the result of surface polarization induced growth due to the chemically active (0 0 0 1)-Zn. (b) High-resolution TEM recorded from the tip of the comb-teeth, showing possible evidence of Zn segregation at the growth front, which is likely to be effective for driving self-catalyzed growth. (c) Structure model of ZnO projected along [0 1 $\bar{1}$ 0], showing the termination effect of the crystal. (d and e) Experimentally observed and theoretically simulated convergent beam electron diffraction patterns for determining the polarity of the nanocombs, respectively. From [55].

extension or compression of nanohelix by a tungsten nanoprobe was recorded continuously through SEM imaging. Fig. 25 shows a series of snap shot SEM images displaying a mechanical loading process by the nanoprobe onto a nanohelix. In Fig. 2a, two nanohelices have been transferred onto a Si substrate and entangled to each other with a cross-knot position, as indicated by an arrowhead. The white arrowhead points to one end of a nanohelix that was welded onto the tungsten nanoprobe using the ion beam induced Pt deposition. To avoid or reduce the damage from the ion beam, the lowest current available for Pt deposition was used. Despite the entanglement between the two nanohelices, the two nanohelices can be easily distinguished in Fig. 25a. The dimensions of the welded nanohelix are approximately 1 μm in diameter, 2.2 μm a pitch, and 220 nm in width. To pull the welded nanohelix out of the cross-knot, the nanoprobe gradually extended the welded nanohelix away from the other one. In reference to the position marked by the arrowhead, it is amazing to find that the welded nanohelix can be pulled to almost straightened shape, while its twist cycles are preserved. The enlarged image in Fig. 25c reveals that the extended nanohelix has reached an extreme extension, for which the width of the nanobelt decreased to ~190 nm, less than the original width of 220 nm, indicating a curly bending of the nanobelt across its width under external mechanical stretching.

A continued stretching manipulation of the nanoprobe has led to the sliding of the cross-knot from its original position in Fig. 25b to an un-knotted position as marked in Fig. 25d. The entangled position was pointed by a dashed arrowhead. Obviously the stretched nanohelix has begun to recover its shape from the extreme extension displayed in Fig. 25b and c. Further manipulation has pulled the welded nanohelix completely away from the unwelded one, as shown in Fig. 25e. A careful comparison to the nanohelix dimensions presented in Fig. 25a indicates that the nanohelix has an almost identical dimensionality including pitch and radius, suggesting a complete elastic recovery, i.e., a super-elasticity (shape memory) behavior.

The nanohelix can be fractured under the manipulation of an AFM tip [67]. Fig. 26a and b are respectively an AFM topography image of a nanohelix after being compressed by the AFM tip and a corresponding SEM image. The measured force–displacement curves for a group of nanohelices are shown in Fig. 26c. A common factor for the fracture of the nanohelices is that the force–displacement presents two sharp drops at F_1 and F_2, the values of which depend on the size of the nanohelix A complete fracture of the nanohelix follows the sharp drop at F_2.

The proposed fracture process is presented in Fig. 26d. The nanohelix deformation process was represented by four instant cross-sectional views perpendicular to the axis of the nanohelix upon the AFM tip compression, a deformation process with four

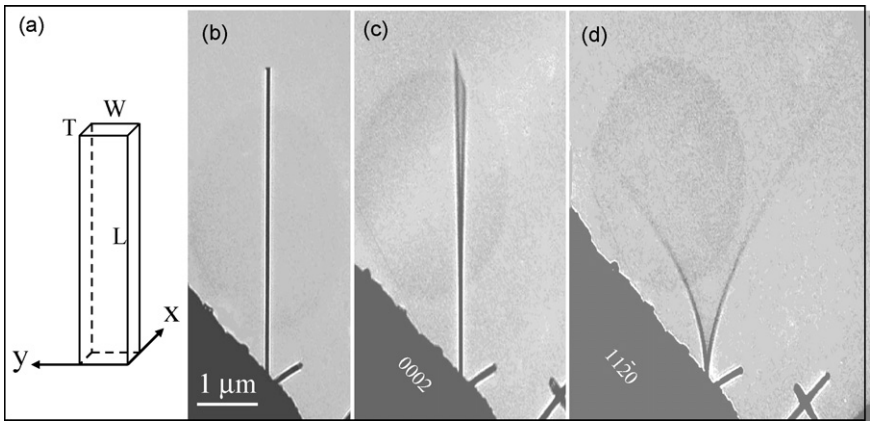

Fig. 21. Measuring the bending modulus of a nanobelt. (a) Geometrical shape of a nanobelt. (b) A ZnO nanobelt at stationary. (c and d) Mechanical resonance of the nanobelt along two orthogonal directions, respectively, closely perpendicular to the viewing direction (ν_x = 622 kHz), and nearly parallel to the viewing direction (ν_y = 691 kHz). From [62].

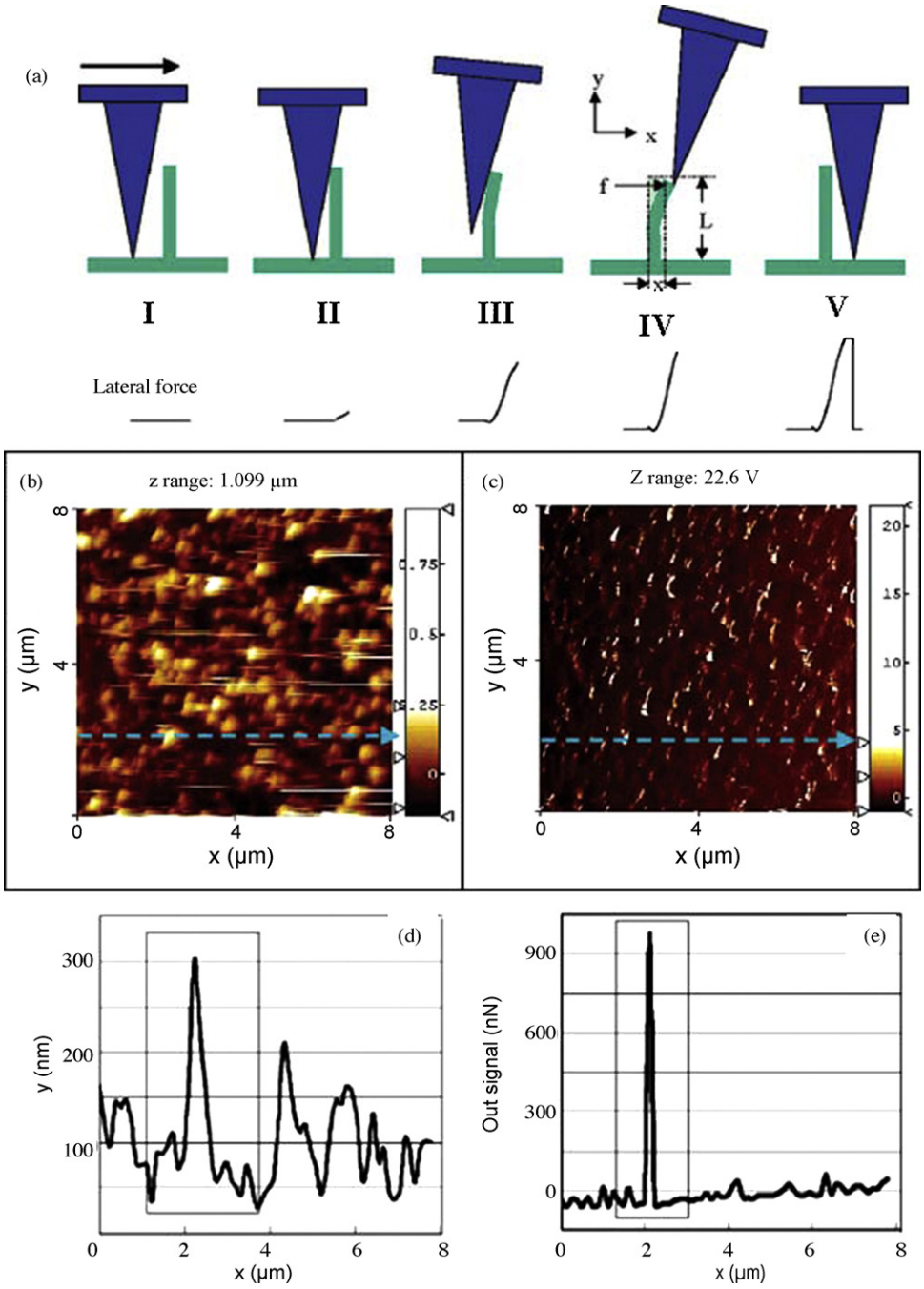

Fig. 22. (a) Procedures for measuring the elastic modulus of aligned nanowire arrays in the AFM contacting mode. (b) Topography image and (c) lateral force image of the aligned ZnO NWs received in AFM contacting mode. (d and e) Line scanning profile along the dashed lines in b and c, respectively. From [63].

stages I, II, III and IV [67]. The four stages illustrate a two-step fracture process, i.e., a pre-buckling (stretching resistant) and then buckling (bending resistant) process. The pre-buckling step is an elastic compression from stage I to stage II, representing compressing a circular nanohelix into an elliptical cross-section shape. Further compression will likely result in the initiation of the buckling. The buckling stage is the steps III and IV. As the deformation transited from a stretching energy dominant to bending energy dominant, there is a sudden softening of the nanohelix, leading to a force drop at a steep rate at the vicinity of F_1. A continuous compressing leads to the eventual fracture of the nanohelix at the tip contact point at a force F_2. Because of the pyramid shape of the AFM tip with a tip radius of ~50 nm, a local fracture resulted from the buckled plastic deformation by the tip is revealed in Fig. 26b. Take nanohelix #1 ($N_2 = 1$) as an example (dark-lined force–displacement curve in Fig. 26c) at $F_1 = 0.61$ μN with a displacement of 115 nm, the force drop occurred as a buckling deformation being initiated (from stage II to III) as a result of transition from stretching resistant deformation to bending dominant. The bending resistance will lead to a later sustained force curve until the tip displacement reached 270 nm, then an eventual fracture occurred at 0.91 μN (IV stage of Fig. 26d).

5.2. Field emission properties

The sharp geometrical shape of nanotubes and nanowires indicates that they might be ideal object for superior field emission. The growth of aligned nanotubes and nanowires has

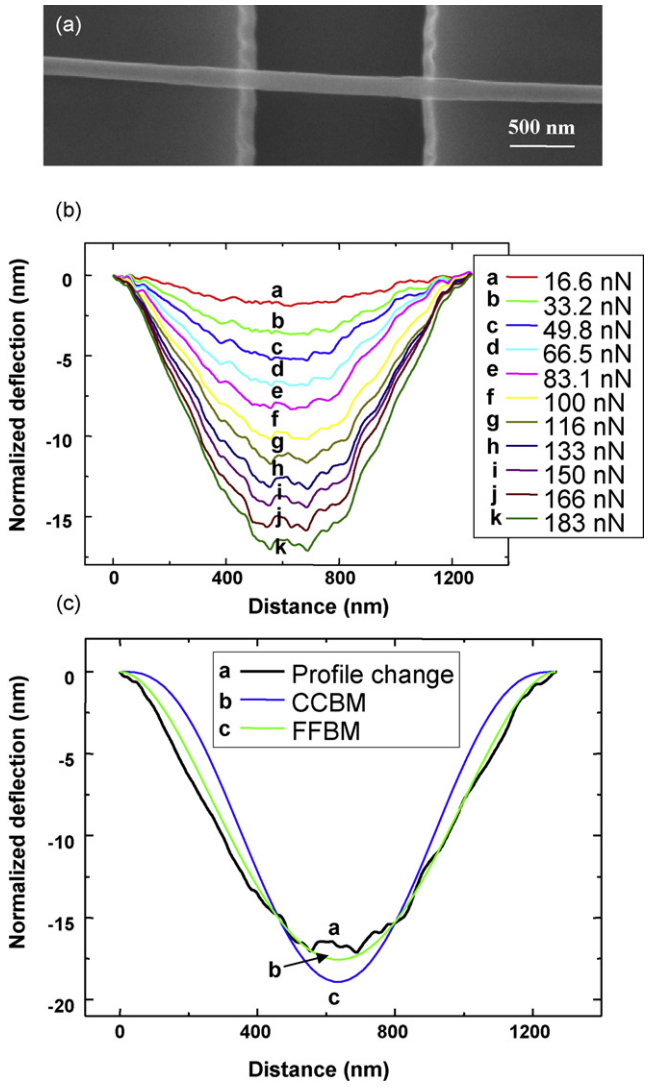

Fig. 23. (a) SEM image of one NB bridged over a trench. (b) The normalized AFM image profile after removing the surface roughness by subtracting the curve acquired at 106 nN; the force is also normalized in reference to the "zero setting point" of 106 nN. (c) Curve fitting using the CCBM and FFBM for the image profiles of NB 1 acquired under normalized force of 183 nN. From [64].

stimulated a great interest in exploring the applications of 1D nanostructure for field emission. The unique geometrical shape of nanobelts is ideal for field emission. Nanowires of refractory materials [68,69] are potential candidates for field emission applications.

The field emission property was measured on the aligned ZnO NWs with five different densities [70]. All of them were grown on the same substrate and measured one after the other under the exact same condition. Typical top-view SEM images of the five samples are shown in Fig. 27a, where they are identified from I to V with a density of 108, 86, 64, 45 and 28 NWs/μm^{-2}, respectively. The FE I–V curves are shown in Fig. 3b. The counter electrode (the tungsten needle tip) was only 0.03 mm^2, which was much smaller than the size of the sample. However, considering the density of the aligned NWs, the number of NWs covered under the counter electrode was at the order of 10^6–10^7, which is big enough to show a representative universal property. Therefore, the total current received was determined by the size of the tungsten tip so that the measured emission current for samples of different grown areas can be compared directly. The highest density NWs were not very effective emission sources (the curve composed by diamond dots). The emission was turned on by the electric field around 20 V/μm and the emission current increased to ~20 μA when the electric field ramped up to 25 V/μm. This was believed to be caused by the screening effect due to the very small space between the NWs. However, from SEM observation, the agglomeration of the NW tips largely reduced the sharp emitting surfaces. Therefore, in this case, the self-attracting phenomenon in high-density NWs would also be responsible for their low emission efficiency.

The highest emission efficiency was observed on samples II and III, which had medium densities (86 and 64 μm^{-2}) and marked by triangular and cross dots in Fig. 27b, respectively. Their turn-on electric field was 8–10 V/μm and the emission current sharply jumped up to ~20 μA at a field of 10–13 V/μm. When the NW density was decreased to 45 μm^{-2} and lower, the emission efficiency became very low, as shown by the star and circle dots in Fig. 27b. Their highest emission current only reached 1–2 μA under the electric field of 25 V/μm (500 V).

5.3. Optical property

5.3.1. Photoluminescence

Optical properties of NWs and NBs are important for many of their technological applications. The ZnO nanobelts produced by the tin film catalyst are rather narrow, thin and uniform (Fig. 28a) [71]. Electron diffraction pattern and high-resolution TEM image show that the nanobelts grow along [0 0 0 1], its top surfaces are $(2\,\bar{1}\,\bar{1}\,0)$ and the side surfaces are $(0\,\bar{1}\,1\,0)$. The average diameter of the nanobelts is 5.5 nm with a standard deviation of ±1.5 nm, indicating a very good size uniformity.

To examine the size induced quantum effect of the ultra-thin ZnO nanobelts, photoluminescence (PL) measurements were performed at room temperature using a Xe lamp with an excitation wavelength of 330 nm (Fig. 28b). In comparison to the PL from nanobelts of an average width of ~200 nm, the 6 nm nanobelts have a 14 nm shift in the emission peak, which possibly indicate quantum confinement due to the reduced size of the nanobelts (Fig. 29).

5.3.2. Nanolaser

Room temperature UV lasing in ZnO nanowires has been demonstrated very recently [33]. PL spectra of the ZnO nanorods were measured on a fluorescence spectrophotometer using a Xe lamp with an excitation wavelength of 325 nm at room temperature. Fig. 19 shows the PL spectrum of the ZnO nanorods with a diameter in the range 60 ± 80 nm. Three emitting bands, including a strong ultraviolet emission at around 386 nm, a very week blue band (440 ± 480 nm), as well as an almost negligible green band (510 ± 580 nm), were observed. The UV emission must be contributing to the near band edge emission of the wide bandgap ZnO. It has been suggested that the green band emission corresponds to the singly ionized oxygen vacancy in ZnO and results from the recombination of a photogenerated hole with the single ionized charge state of this defect. The stronger the intensity of the green luminescence, the more singly ionized oxygen vacancies there are. Thus the almost negligible green band in Fig. 19 shows that there is a very low concentration of oxygen vacancies in the well-aligned ZnO nanorods. The observation of blue band emission (440 ± 480 nm) of ZnO film has been also reported using cathodeluminescence.

5.3.3. Light emitting diode

Light emitting diode (LED) based on n-ZnO NWs/p-GaN film hybrid heterojunction can be fabricated by growing n-type ZnO nanowires array directly on p-GaN wafer [72–74]. The grown NWs have a uniaxial orientation of ⟨0 0 0 1⟩ with an epitaxial orientation relationship with the GaN substrate, for (n-ZnO NWs)/(p-GaN film) hybrid heterojunctions. LEDs have been fabricated by building

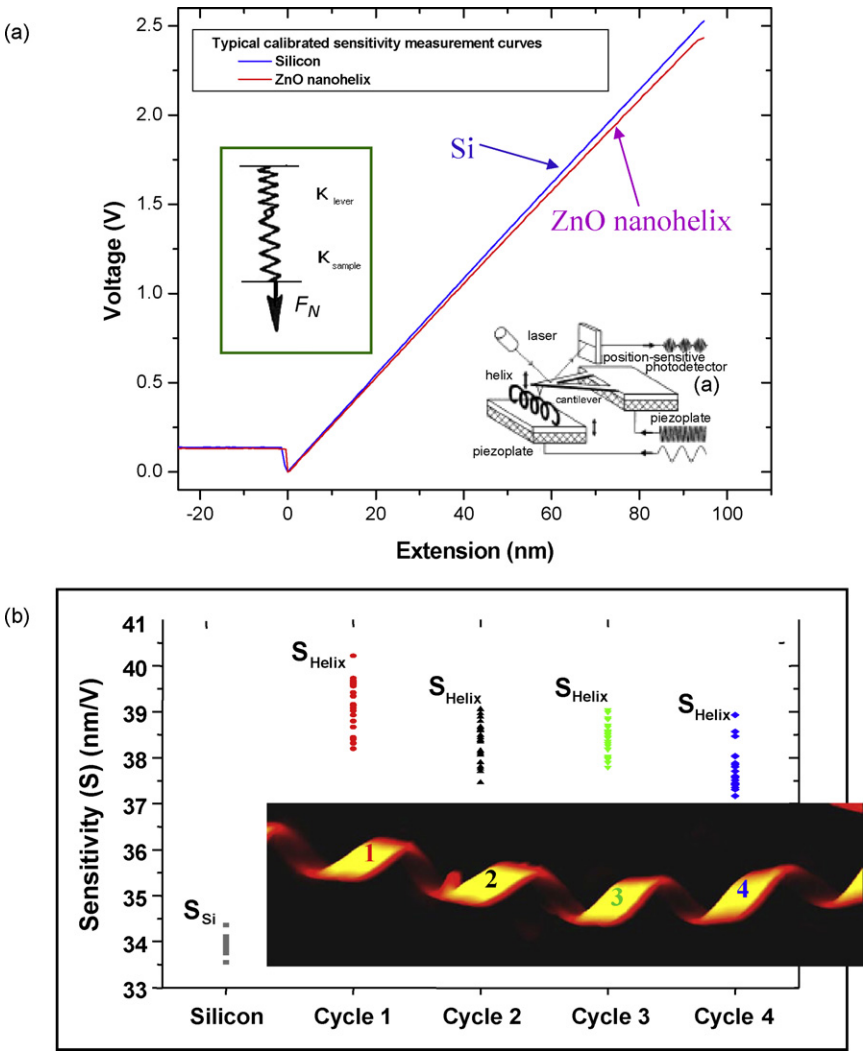

Fig. 24. Measuring the elastic spring constant of a ZnO nanohelix. (a) Driving voltage-extension curve of an AFM tip as it is compressing a nanohelix. The inset is a schematic of the experimental set up. AFM contact mode measurement of the sensitivity (S) of the photo-detector for the silicon substrate and the four cycles of a ZnO nanohelix as indicated by 1–4 in the inserted AFM image. The sensitivity S of the photo-detector is the inverse of the slope of the force–displacement (F–Z) curve, which is directly related to the elastic property. The measurement was done by positioning the tip on the surface of the up most middle-point of the cycle of the helix. Each dot represents one measurement. (b) The measured sensitivity for different cycles of the nanohelix. The sensitivity S_{Si} for silicon is significantly lower than those for the ZnO nanohelix (S_{Helix}). The inset is an AFM image of the nanohelix that was measured. From [17].

electrodes at the p- and n-side. A plot of electroluminescence (EL) intensity versus forward bias by fixing at 400 nm emission wavelength is shown in Fig. 30 [75]. The junction gives blue light emission.

5.3.4. Dye-sensitized solar cell

Dye-sensitized solar cell (DSSC) made of organic–inorganic heterojunctions [76,77] has been fabricated by using the large surface area offered by nanowire array. Vertically aligned ZnO NWs with heights of ~10 μm were grown on an ITO coated glass substrate through hydrothermal approach as the electron collector for DSSC. Then, NWs were immersed in a 0.5 mmol l^{-1} solution of $(Bu_4N)_2Ru(dcbpyH)_2(NCS)_2$ (N719 dye, Dyesol) in ethanol for 1 h. An electrode coated with a thin layer (~200 nm) of Pt served as the anode of DSSC. DSSC was assembled by applying a 30 μm thick Bynel spacer between the ITO substrate and the silicon counter electrode. Liquid electrolyte composed the mixture of 0.5 M LiI, 50 mM I_2 and 0.5 M 4-tertbutylpyridine in 3-methoxypropionitrile and infiltrated into the internal volume of DSSC by capillary effect. The DSSC was then heated to 120 °C to soften the spacer and seal the edges to prevent the leakage of electrolyte. The I–V characteristic of the device can give the efficiency of the DSSC (Fig. 31) [78]. An efficiency of ~1.5% has been achieved [79].

5.4. Nanosensors

5.4.1. UV sensors

ZnO has great promise for optical applications, such as UV detection. However, due to the presence of point defects and confined dimensionality, the UV sensitivity of ZnO NWs and NBs is limited. We have recently demonstrate that the UV response of a ZnO NB based sensor has been enhanced by close to five orders of magnitude after functionalizing its surface with a polymer that has a high UV absorption ability [80]. This giant enhancement in photoconductance is attributed to the energy levels introduced by the polymer lying in the corresponding band gap and in the conduction band of ZnO, which served as a "hopping" state and increased the excitation probability of an electron to the conduction band. This exciting discovery will greatly impact the applications of ZnO NWs/NBs for UV detection.

The devices based on ZnO NB were fabricated by aligning a ZnO NB across two metal electrodes. Different kinds of polymers

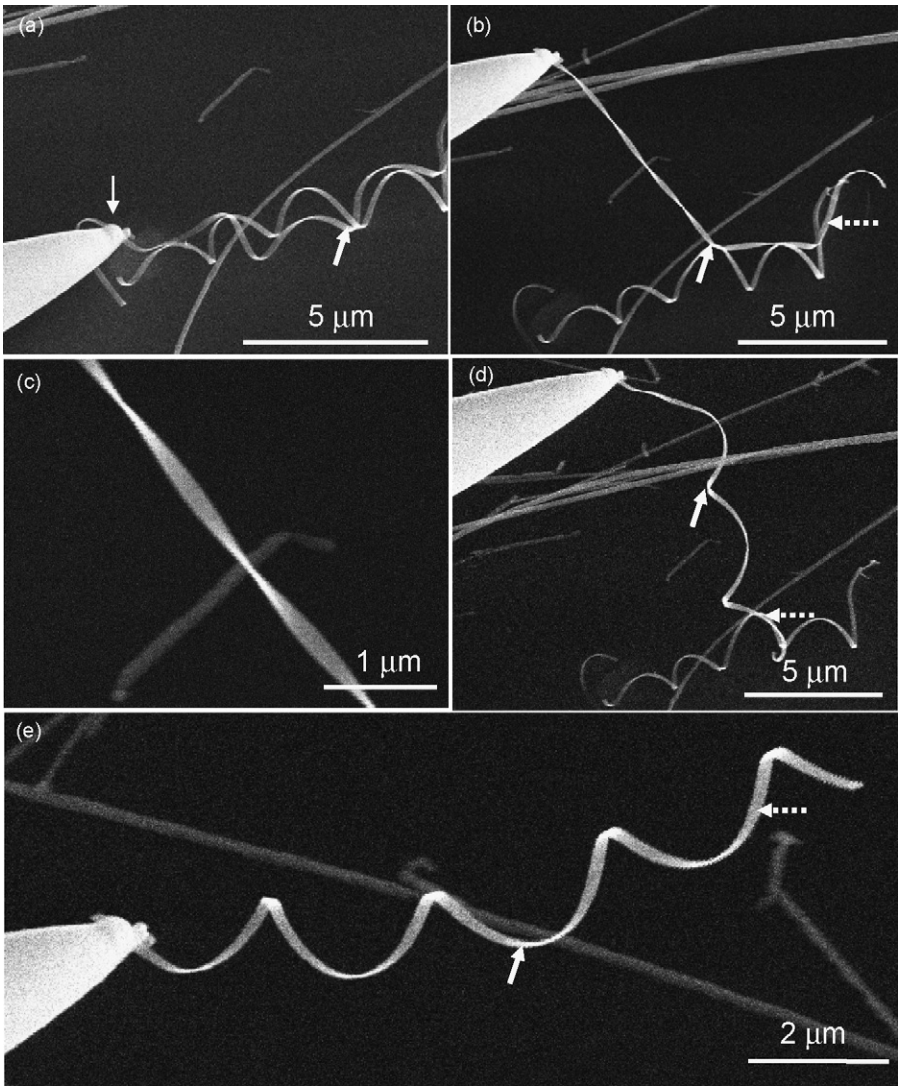

Fig. 25. A manipulation process of a nanohelix upon an extremely large axial stretching and shape recovery process. The nanohelix was deposited on silicon substrate. (a) One end of a nanohelix was welded with Pt onto a tungsten nanoprobe. (b) An attempt for extracting the welded nanohelix out of the entangled nanohelices. (c) An enlarged SEM image showing the extremely stretched nanohelix. (d) A continuous extraction led to an initial release of the welded nanohelix from the entangled cluster and a recovery of the nanohelix shape. (e) A complete restoring of the nanohelix shape after the manipulation in (b) and (c), suggesting a super-elasticity (shape memory) behavior. From [67].

with different UV absorption abilities and wavelengths were used in the experiment to test their effects on enhancing UV response of the ZnO NB (Fig. 32a), including polystyrene sulfate (PSS), poly(styrene-co-maleic acid) (PS-co-MAc), anionically charged poly(N-isopropylacrylamide) (PNIPAM), carboxy-methylcellulose (CMC). For the layered coating, these polymers are all negatively charged or modified to possess negative charges. A scanning electron microscopy (SEM) image of these functionalized ZnO NBs is shown in the inset of Fig. 32b. The blur edge of NBs in the figure indicates successful coating of polymers onto the NBs.

Soci et al. [81] have proposed that the high sensitivity UV detection of ZnO NW was due to the presence of oxygen-related hole-trapping states at the NW surface. This process can also be applied to explain our observation (Fig. 32c). The first layer of coated polymer is cationically charged PDADMAC. The free electrons might be trapped by the positively charged sites at the surface. Upon UV illumination, these immobilized electrons can trap the photon-generated holes, and thus reduces the electron–hole recombination rates in ZnO NB and increases the carrier lifetime. This mechanism accounts for the enhanced UV response for ZnO NB coated with PS-co-Mac, PNIPAM, and CMC.

5.4.2. Gas sensors

Owing to the large surface-to-volume ratio, the conductance of the nanowires is very sensitive to the change in surface chemistry. As a molecule being adsorbed on nanowire surfaces, charge transfer can occur between the adsorbate and the adsorbent. The adsorbed molecule can significantly modify the dielectric property at the surface, which greatly affects the surface conductance. Therefore, nanowires/nanobelts can result in a huge improvement in gas sensing performances [82].

Fig. 33 illustrates the dynamic response of ZnO nanowires to 2 and 4 ppm concentration squared pulses of nitrogen dioxide at 200 °C working temperature with 40% relative humidity (RH) [83]. The current flowing through the sample decreases, as was expected for an n-type semiconductor, because of extractions of electrons from the conduction band. The response and recovery times are of the order of minutes and the recovery of the air conductance value after the gas tests is complete, proving that the gas reaction between nitrogen dioxide and the ZnO nanowire

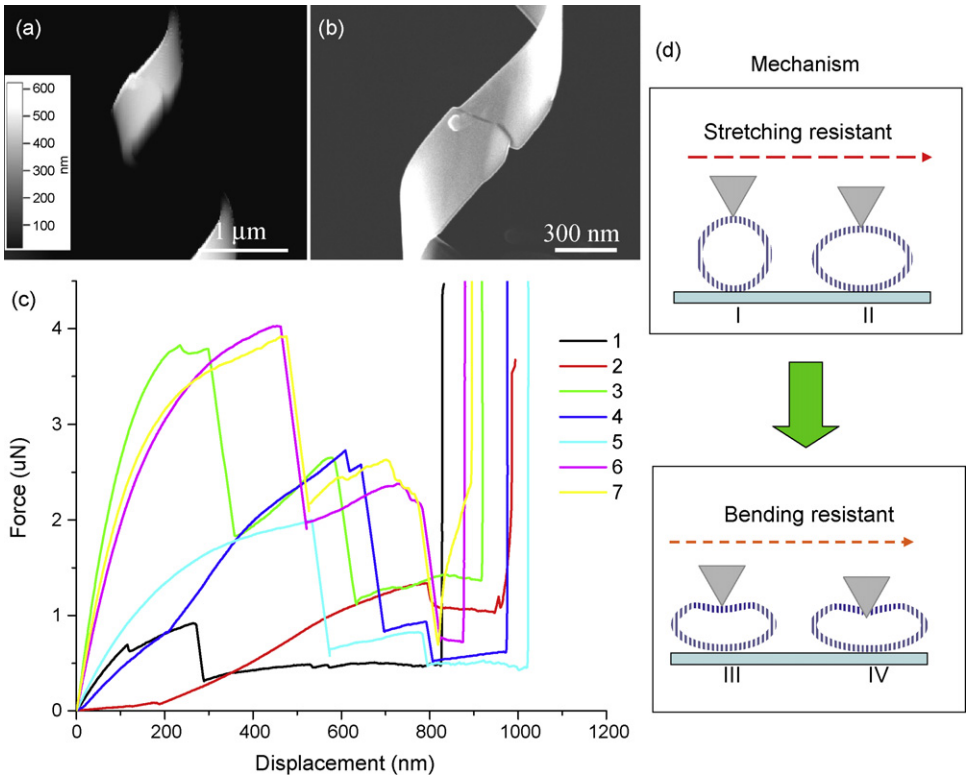

Fig. 26. A two-step fracture process of nanohelices upon transversal compression by an AFM tip. Subparts (a and b) are respectively an AFM topography image after the tip induced fracture over a nanohelix and the corresponding SEM image of the fractured part. (c) Force–displacement curves for seven nanohelices recorded during AFM tip compression and fracture process. (d) A schematic model of the two-step fracture process of the nanohelix upon transverse compression by an AFM tip. From [67].

surface is reversible at this operating temperature. ZnO nanowires have been utilized for fabricating conductometric sensors for ethanol [84] and NH_3 [85], ionization based gas sensors [86], intracellular pH sensor [87] and electrochemical sensors [88].

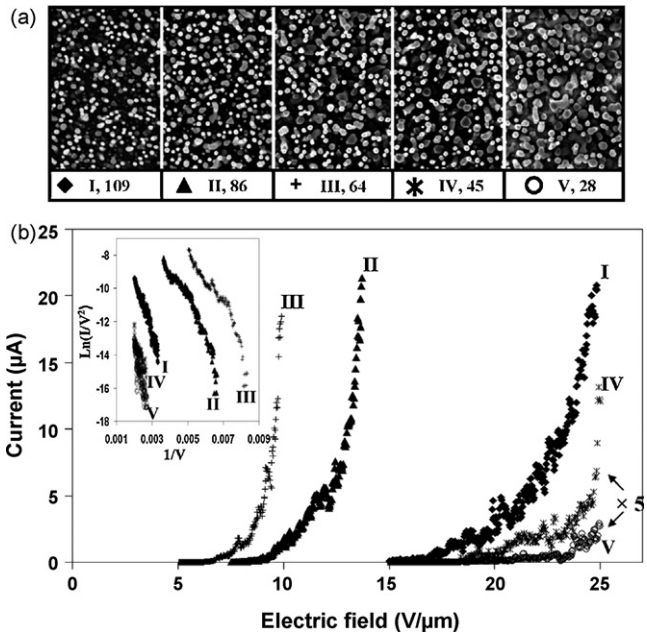

Fig. 27. Field emission. (a) Top-view SEM images of the aligned ZnO nanowire arrays with five different densities. Curve IV and V are magnified by 5 times for better illustration. (b) The corresponding field emission I–V characteristics and the converted *F–N* curves. From [70].

5.5. Piezoelectric properties

Piezoelectricity is due to the atomic scale polarization. To illustrate the piezoelectricity, one considers an atom with a positive charge that is surrounded tetrahedrally by anions (Fig. 34a). The center of gravity of the negative charges is at the center of the tetrahedron. By exerting a pressure on the crystal along the cornering direction of the tetrahedron, the tetrahedron will experience a distortion and the center of gravity of the negative charges will no longer coincide with the position of the positive central atom, an electric dipole is generated. If all of the tetrahedra in the crystal have the same orientation or some other mutual orientation that does not allow for a cancellation among the dipoles, the crystal will have a macroscopic dipole. The two opposite faces of the crystal have opposite electric charges.

The piezoelectricity refers to a reverse process in which a contraction or elongation is created to the crystal once it is positioned in an electric field. Crystals can only be piezoelectric if they are non-central symmetric to ensure the non-compensation among the dipoles created by the tetrahedra. Piezoelectric effect can convert a mechanical vibration into an electric signal or vice versa. It is widely used in resonators, controlling tip movement in scanning probe microscopy, sensors for vibration waves in air and under sea etc.

Piezoelectricity is an intrinsic property of ZnO, and the piezoelectricity is not induced by the polar surfaces. The magnitude of the piezoelectric effect depends on the growth direction of the nanobelt. The piezoelectric coefficient of ZnO nanobelt has been measured by atomic force microscopy using a conductive tip [89]. After coating (1 0 0) Si wafer with a 100 nm Pd, ZnO nanobelts were dispersed on the conductive surface. Then the whole surface was coated with another 5 nm Pd coating, which served as an electrode on ZnO nanobelt to get uniform electric field

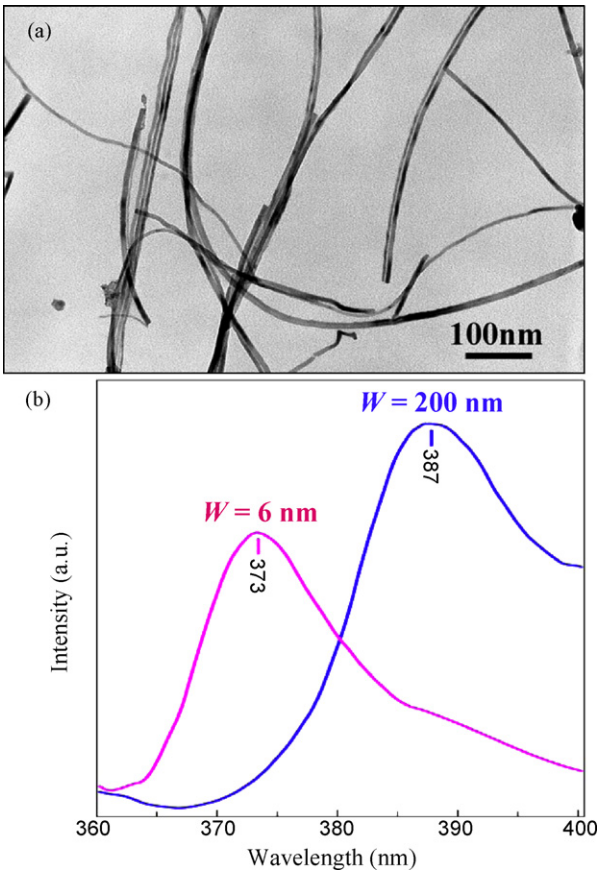

Fig. 28. (a) Low magnification TEM image showing the size uniformity of ZnO nanobelts. (b) Photoluminescence spectra acquired from the $W = 200$ nm wide ZnO nanobelts and the $W = 6$ nm wide ZnO nanobelts. From [71].

and avoid electrostatic effect. Extra care was taken to ensure that top and bottom surface of the nanobelt was not short circuited after Pd deposition. The ZnO nanobelt was located by a commercially available AFM under tapping mode. Piezoresponse force microscopy (PFM) is used to measure the effective piezoelectric coefficient (d_{33}) of individual (0 0 0 1) surface dominated

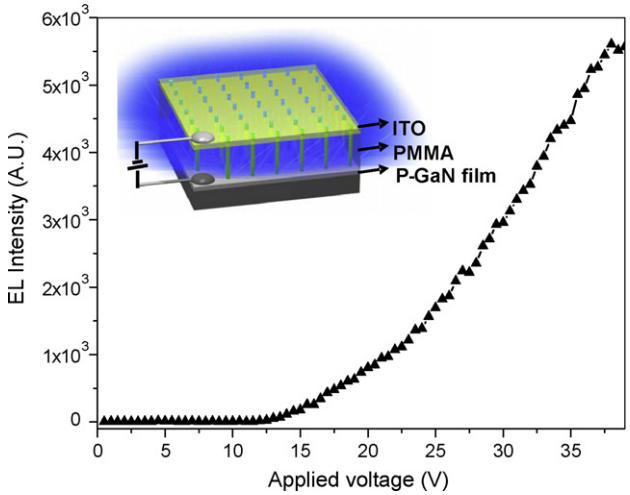

Fig. 30. A plot of electroluminescence (EL) intensity vs forward bias by fixing at 400 nm emission wavelength. The inset is a schematic illustration of the (n-ZnO NWs)/(p-GaN film) hybrid heterojunction LED device. From [75].

zinc oxide nanobelt lying on conductive surface. Based on references of bulk (0 0 0 1) ZnO and x-cut quartz, effective piezoelectric coefficient d_{33} of ZnO nanobelt is found to be frequency dependent and varies from 14.3 pm/V to 26.7 pm/V (Fig. 34b), which is much larger than that of the bulk (0 0 0 1) ZnO of 9.93 pm/V. The results project the applications of ZnO nanobelts as nanosensors and nanoactuators.

5.6. Nanogenerators

Exploring renewable, sustainable and green energy resources is the most critical challenge to sustainable development of human civilization. At the large-scale, besides the well known energy resources that power the world today, such as petroleum, coal, hydraulic, natural gas and nuclear, active research and development are being taken in exploring alternative energy resources such as solar, geothermal, biomass, nuclear, wind, and hydrogen. At a much smaller scale, energy and technologies are desperately needed for independent and continuous operations of implantable

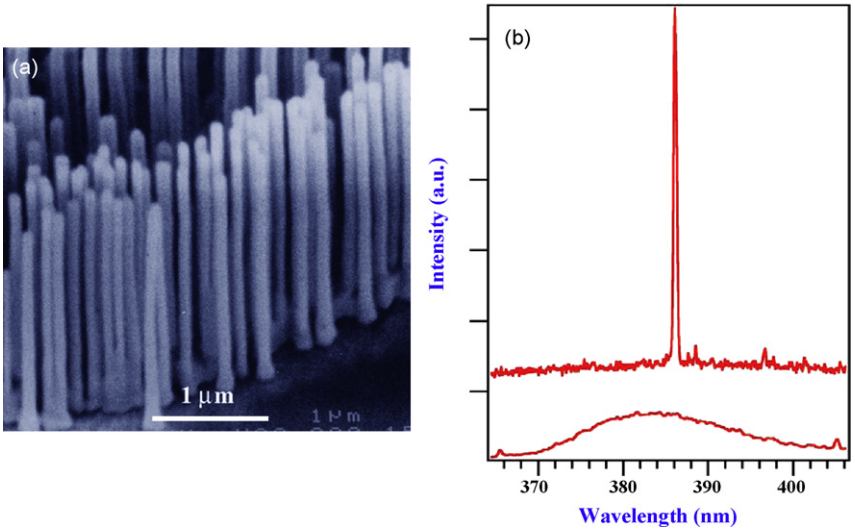

Fig. 29. (a) SEM image of aligned ZnO nanowire arrays grown on sapphire substrate coated with a 3 nm thick layer of Au. (b) Emission spectra from nanowire arrays at pump power of 20 and 100 kW/cm^2. The spectra are offset for easy comparison. Stimulated emission from the nanowires was collected in the direction along the nanowire's end-plane normal (the symmetric axis) with a monochromator. All experiments were carried out at room temperature (courtesy of Dr. Peidong Yang [33]).

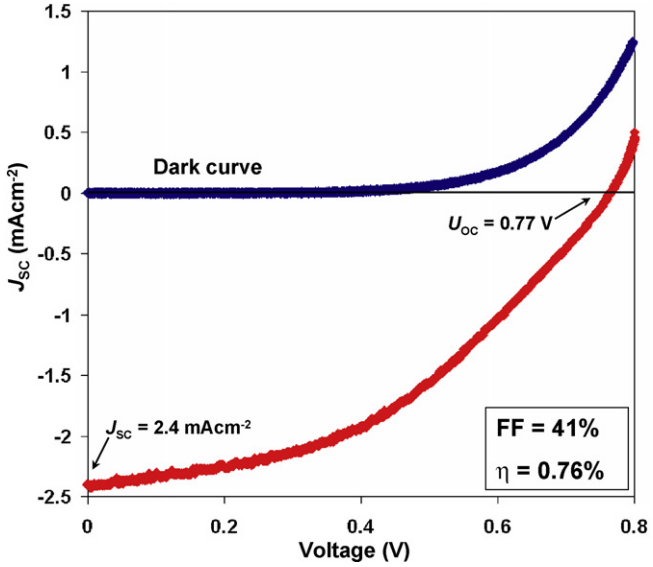

Fig. 31. *J–V* (I–V) curve recorded from a DSSC under simulated sunlight. The blue curve is the I–V curve when there is no sunlight illumination, which is a good calibration about the response of the SC. By illuminating with sunlight, the open circuit voltage is 0.77 V and the short circuit current is 240 μA (red curve). The fill factor of this DSSC is 41% at the operation point U = 0.471 V and I = 170 μA. The energy conversion efficiency was calculated to be 0.76%. From [78]. (For interpretation of the references to color in this figure legend, the reader is referred to the web version of the article.)

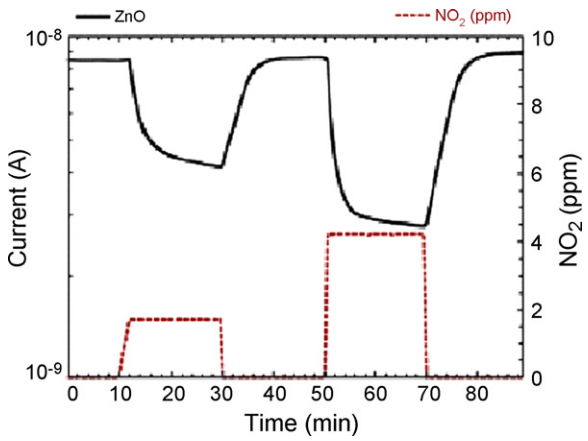

Fig. 33. Dynamic response of zinc oxide nanowires to 2 and 4 ppm concentration square pulses of nitrogen dioxide at 200 °C working temperature with 40%RH (courtesy of E. Comini, C. Baratto, G. Faglia, M. Ferroni and G. Sberveglieri [83]).

biosensors, ultra-sensitive chemical and bimolecular sensors, nanorobotics, micro-electromechanical systems, remote and mobile environmental sensors, homeland security and even portable personal electronics. A nanorobot, for example, is proposed to be a smart machine that may be able to sense and adapt to the environment, manipulate objects, taking actions and perform complex functions, but a key challenge is to find a power source that can drive the nanorobot without adding much weight. An implanted wireless biosensor, for example, requires a power source, which may be provided directly or indirectly by charging of a battery. It is highly desired for wireless devices and even required for implanted biomedical devices to be self-powered without using battery. Therefore, it is desperate to develop nanotechnology that harvests energy from the environment for self-powering these nanodevices [90,91].

The concept of the NG was first introduced by examining the piezoelectric properties of ZnO nanowires (NWs) using an atomic

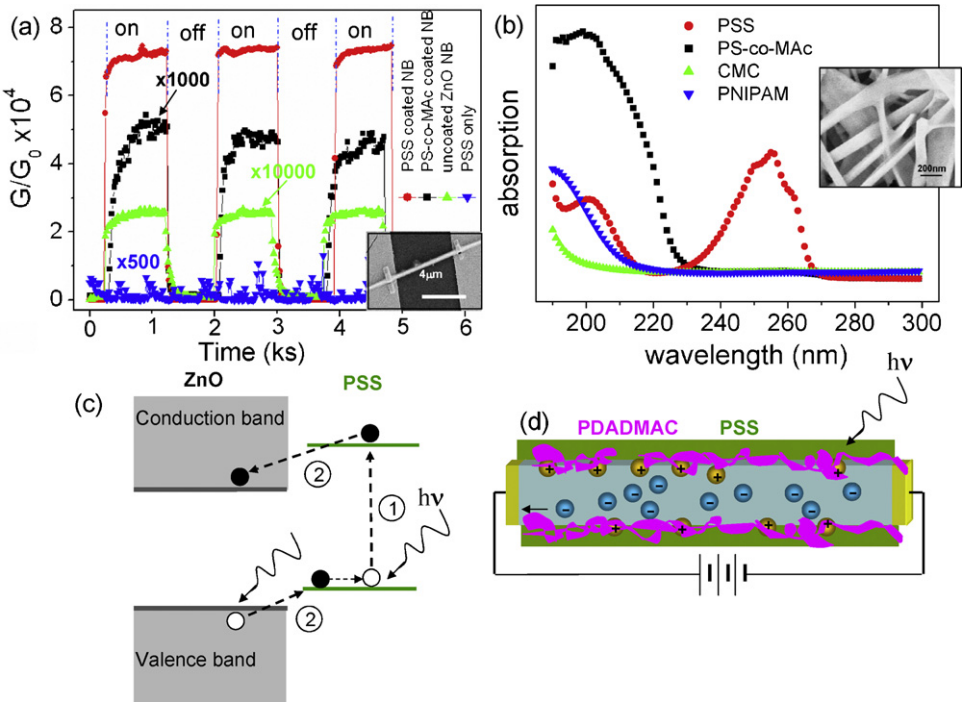

Fig. 32. UV detector. (a) Normalized conductance responses of a single functionalized ZnO NB device (see inset) upon UV illumination being tuned on and off: bare ZnO NB without coating (green line, magnified by 10,000), PS-co-MAc coated ZnO NB (dark line, magnified by 1000), PSS coated ZnO NB (red line), PSS polymer only (blue line, magnified by 500). Inset is an SEM image of a typical device. The applied voltage remained at 1 V for all of the measurements. (b) UV absorption spectra of PSS (red line), PS-co-MAc (dark line), PNIPAM (blue line), CMC (green line). Inset is an SEM image of a polymer coated ZnO NB sample. (c) Schematic illustration of the electron–hole generation process with facilitation of transition states from the molecular energy states in PSS. (d) Schematically illustration of photon induced carrier transportation process in a ZnO NB by UV illumination. From [80].

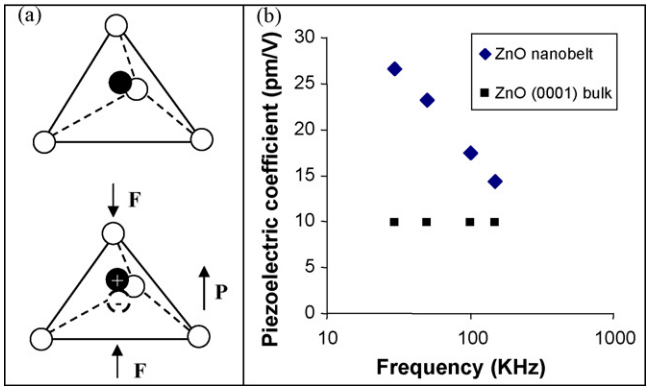

Fig. 34. (a) Schematics showing piezoelectric effect in tetrahedrally coordinated cation–anion unit. (b) Experimentally measured piezoelectric coefficient d_{33} for ZnO and its comparison to that of the bulk (courtesy of Prof. Scott Mao and Minhua Zhao, University of Pittsburgh). From [89].

force microscope (AFM) [92,93]. The measurements were performed by AFM using a Si tip coated with Pt film. In the AFM contact mode, a constant normal force of 5 nN was maintained between the tip and sample surface (Fig. 35b). The tip scanned over the top of the ZnO NW, and the tip's height was adjusted according to the surface morphology and local contacting force. In the corresponding voltage output image for each contact position, many sharp output peaks were observed (Fig. 35c). Note the voltage signal was inverted for display purpose, it is actually negative in reference to the grounded end. By examining the topological profile of a NW and its corresponding output potential, a delay was observed for the voltage output signal (Fig. 35d), which means that there was no electric power output when the tip was first in contact with the NW, but a sharp voltage peak was generated at the moment when the tip was about to leave the contact with NW. This delay is a key signature about the power output process.

5.6.1. Physical principle: n-type ZnO nanowire

The physical principle of the nanogenerator is a coupling of piezoelectric and semiconducting properties [92]. The energy generation is a flow of charge carriers under the driving of piezoelectric potential, and the current direction is defined by the polarity of the Schottky barrier at the metal and nanowire interface. For a vertical, straight ZnO NW, the deflection of the NW by AFM tip creates a strain field, with the outer surface being tensile (positive strain ε) and inner surface compressive (negative strain ε). The asymmetric strain introduces an asymmetric potential at the two surfaces, with the compressed surface negative V^- and the tensile surface positive V^+.

An as-synthesized ZnO NW is generally n-type. The presence of oxygen vacancies and impurities and a large portion of surface atoms (surface states) naturally introduces a moderate conductivity for the NW. These free carriers can partially screen the piezoelectric charges at the positive potential side, but they cannot entirely neutralize the charges. Therefore, the piezoelectric potential still preserves, at a reduced magnitude, even with consideration the moderate conductivity of ZnO.

We now present an understanding about the charge releasing process for a NG based on band structure model [91]. The AFM tip (T) has a Schottky contact (barrier height Φ_{SB}) with the NW, while the NW has an Ohmic contact with the grounded side (G) (Fig. 36a). When the tip slowly pushes the NW, a positive piezoelectric potential V^+ is created at its tensile surface. As the tips continue to push the NW, electrons slowly flow from the grounded electrode through the external load to reach the tip, but the electrons cannot across the tip–NW interface due to the presence of a reversely biased Schottky barrier at the contact (Fig. 36b). In such a case, the accumulated free charges at the tip may affect the piezoelectric potential distribution in the NW owing to the screening effect of

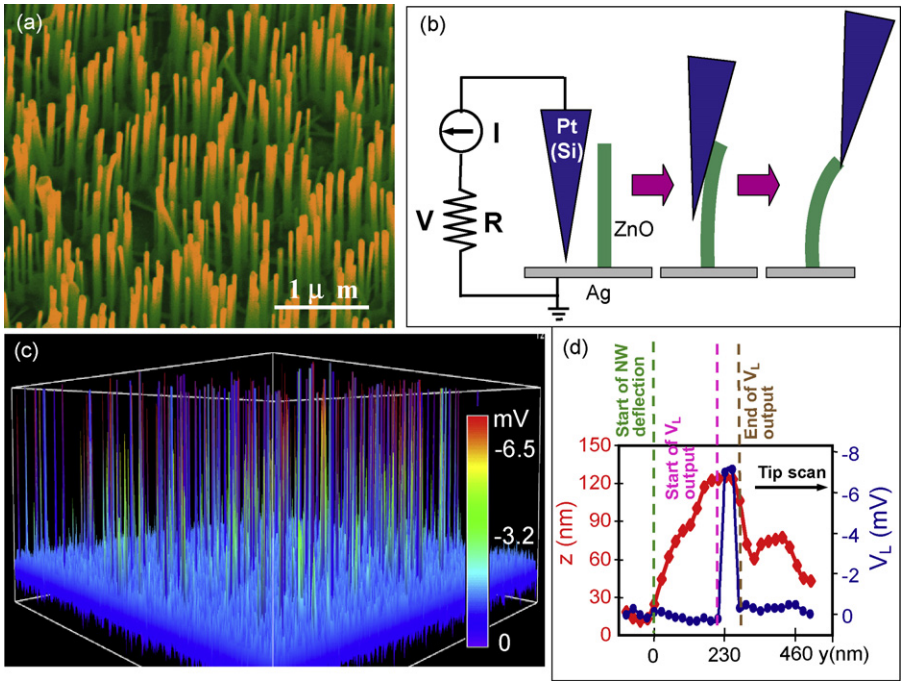

Fig. 35. (a) Scanning electron microscopy images of aligned ZnO NWs grown on GaN/sapphire substrate. (b) Experimental set up and procedures for generating electricity by deforming a piezoelectric NW using a conductive AFM tip. The AFM scans across the NW arrays in contact mode. (c) Output voltage image of the NW arrays when the AFM tip scans across the NW arrays. (d) An overlap plot of the AFM topological image (red line) and the corresponding generated voltage (blue line) for a single scan of the tip across a NW. A delay in the electricity generation is apparent. From [92].

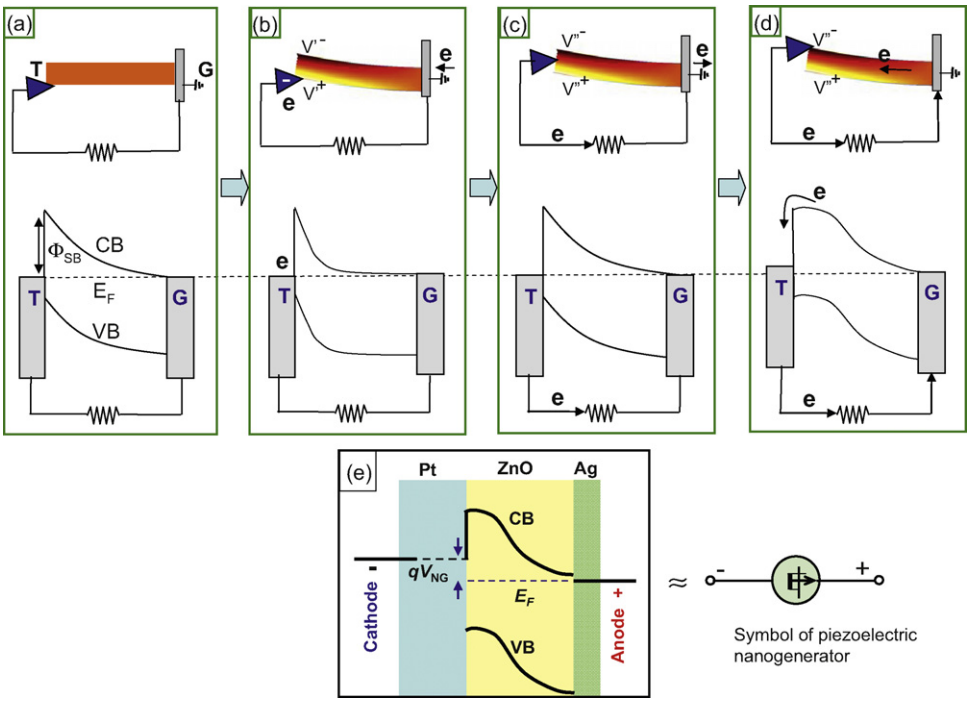

Fig. 36. Band diagram for understanding the charge outputting and flowing processes in the nanogenerator. (a) Schematic and energy diagram of a NW with one end grounded (G) and the other end to be pushed by a conductive AFM tip (T). A Schottky barrier is at the tip–NW interface. (b) Once being slowly deflected, the asymmetric piezoelectric potential in the NW changes the profile of the conduction band (CB). The local positive piezoelectric potential at the contact area results in a slow-flow of electrons from ground through the load to the tip. The electrons will be accumulated in the tip. (c) When the tip scans across the NW and reach its middle point, a drop in local potential to zero results in a back flow of the accumulated electrons through the load into ground. (d) Once the tip reaches the compressive surface, a local negative piezoelectric potential raises the profile of the conduction band. If the piezoelectric potential is large enough, electrons in the external circuit can be driven to flow. This circular motion of the electrons in the circuit is the output current. (e) Energy band diagram for the NG, presenting the output voltage and the role played by the piezoelectric potential. The diagram on the right-hand side is the symbol designed for representing a piezoelectric nanogenerator. From [91].

the charge carriers. The piezoelectric potential is generated due to the rigid and non-mobile ionic charges in the NW, it cannot be completely depleted by the free carriers. The local newly established potential V'^{+} lowers the conduction band (CB) slightly.

When the tip scans in contact mode across the NW and reaches the middle point of the NW (see Fig. 36c), the local piezoelectric potential is zero. In such a case, with a sudden drop in local potential, the originally accumulated electrons in the tip back flow through the load to the ground. This is a process faster than the charge accumulation process presented in Fig. 36b. An alternative but the same result case is that the tip temporarily lifts off from the NW, which also leads to the back flow of the accumulated electrons to the ground.

When the tip reaches the compressive side of the NW (Fig. 36d), the local potential drops to V''^{-} (negative), which results in the high raising of the conduction band near the tip. If the raise in local potential energy is large enough as determined by the degree of NW bending, the piezoelectric potential can drive the flow of electrons in the external circuit, thus producing a current. This process is a lot faster than the charge accumulation process, thus, the created transient potential at the external load is large enough to be detected beyond noise level.

The next question is how large is the output voltage? This question can be answered by the energy band diagram shown in Fig. 36e for the NG. The role played by the piezoelectric potential is to drive the electrons from the ZnO NW to overcome the threshold energy at the metal–ZnO interface into the Pt electrode, but it does not directly determine the magnitude of the output voltage. As more electrons are being "pumped" into the Pt electrode, the local Fermi surface in raised. Therefore, the output voltage is the difference between the Fermi energies for Pt and the bottom electrode Ag.

We have investigated the electricity generation for as-synthesized n-type nanowires of GaN, CdS [94,95], ZnS [96] and AlGaN. All of which showed the same behavior as that of ZnO. Fig. 37a–c shows the data received from n-type GaN nanowires. Negative output voltage was received once the nanowires being deflected by Pt metal tip, which forms a Schottky contact with GaN (Fig. 37d).

5.6.2. Physical principle: p-type ZnO nanowire

We have recently measured the electricity generation of p-type ZnO nanowires, and the results are shown in Fig. 38a and b [97]. In contrast to the result received for n-type ZnO nanowires, the output voltage at the external load is always positive in reference to the grounded nanowire root. To confirm this result, we used the same AFM tip and under identical experimental conditions at almost at the same time, we measured the electricity generation of n-type ZnO nanowire, and the results are shown in Fig. 38d and e, clearly showing negative output voltage. More importantly, in reference to the morphological image of the nanowire, the output voltage peak occurs at the first half of the contact between the tip and the nanowire for the p-type nanowire (Fig. 38b), while it occurs at the last half of the contact between the tip and the nanowire for the n-type nanowire (Fig. 38f). This distinct difference is directly related to the mechanism of the nanogenerator.

As for the p-type of nanowires, the Fermi level is located more close to the valence band edge. The metal–semiconductor is forward biased if the semiconductor has a higher potential, otherwise the junction is reversely biased. When the tip is in contact with the nanowire, as shown in Fig. 38, the negative piezoelectric charges created at the compressed side of the nanowire is partially screened by the positively charged holes.

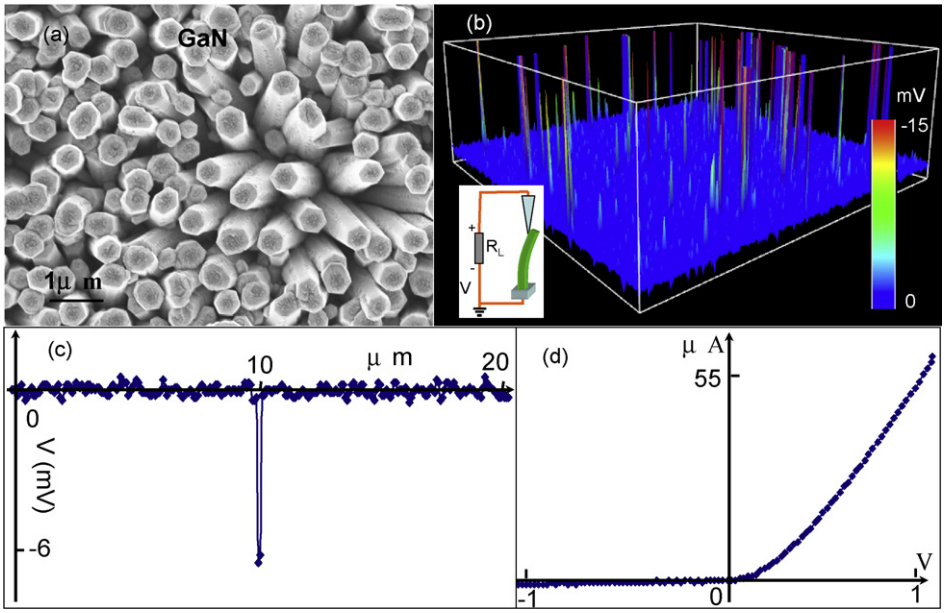

Fig. 37. (a) SEM image of GaN nanowires. (b) 3D voltage output profile across the nanowire array when an AFM tip was scanned in contact mode for generating electricity. (c) A single output voltage peak selected from (b) showing typical negative voltage output of ~−6 mV. (d) The I–V characteristic curve between the Pt tip and the n-type GaN nanowires (sample courtesy of Prof. Zheng Hu, Nanjing University).

Once the magnitude of the positive piezoelectric potential at the stretched side exceeds a value that can either drive the p-type carriers or the electrons in the metal tip across the junction, a positive output voltage would be observed at the external load. This event occurs at the first half of the contact between the metal tip and the nanowire.

As for the n-type of nanowires, the metal–semiconductor is forward biased if the metal has a higher potential, otherwise the junction is reversely biased. When the tip is in contact with the nanowire, as shown in Fig. 38, the positive piezoelectric charges created at the stretched side of the nanowire is partially screened by the electrons. A potential different is established between the

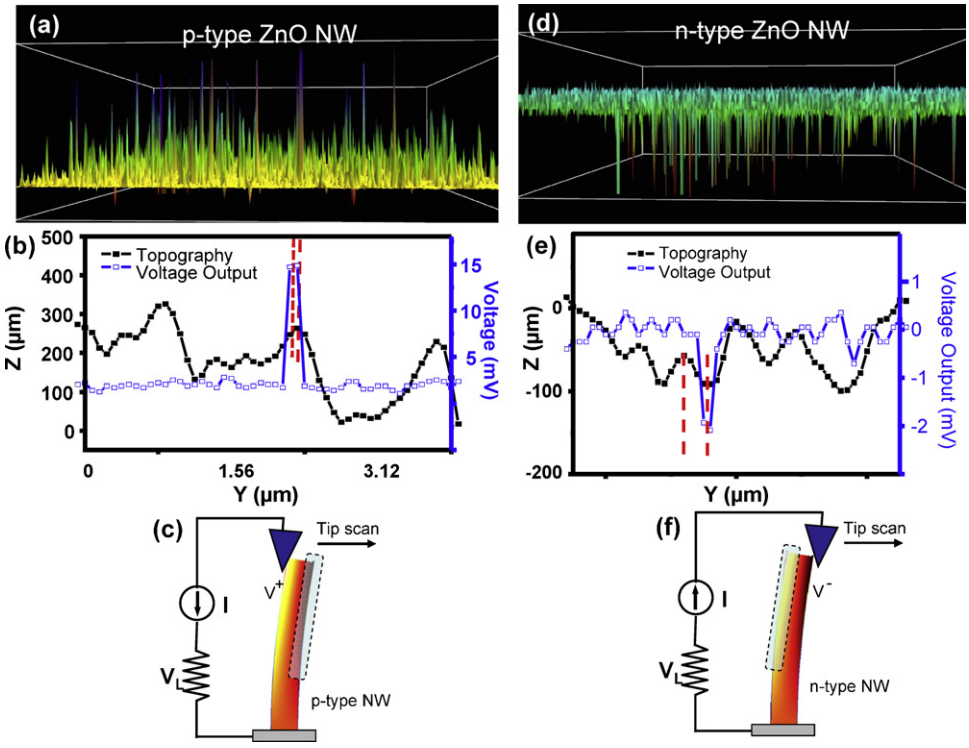

Fig. 38. A comparison of nanogenerators based on n-type and p-type ZnO nanowires. (a) 3D voltage output profile across the n-type ZnO nanowire array when an AFM tip was scanned in contact mode for generating electricity and (b) a corresponding comparison between the topological scan and output voltage scan, showing the negative output voltage was generated when the tip reached the compressed side of the nanowire. (c) The mechanism for the n-type nanowire nanogenerator. (d) 3D voltage output profile across the p-type ZnO nanowire array when an AFM tip was scanned in contact mode for generating electricity and (e) a corresponding comparison between the topological scan and output voltage scan, showing the negative output voltage was generated when the tip reached the stretching side of the nanowire. (c) The mechanism for the p-type nanowire nanogenerator.

tip and the nanowire once the tip is in contact with the compressed side of the nanowire, which has negative piezoelectric potential. This piezoelectric potential at the compressed side drives the electrons to flow across the junction, resulting in a negative voltage at the external load. This event occurs at the last half of the contact between the metal tip and the nanowire.

5.6.3. Direct-current nanogenerator driven by ultrasonic wave

To make the tip driven energy harvesting approach into a viable technology, we need to overcome three obstacles. First, we must eliminate the use of AFM for making the mechanical deformation of the NWs so that the power generation can be achieved by an adaptable, mobile and cost-effective approach over a larger scale. Secondly, all of the NWs are required to generate electricity simultaneously and continuously, and all the electricity can be effectively collected and output. Finally, the energy to be converted into electricity has to be provided in a form of wave/vibration from the environment, so the NG can operate "independently" and wirelessly.

Our approach was to use a zigzag electrode to replace the role played by thousands of parallel AFM tips [98]. Such an electrode can be made by etching a silicon wafer; orientation dependent etching rate produces pyramid type of structures. Fig. 39c shows four possible configurations of contact between a NW and the zigzag electrode. NWs I and II are being deflected towards left- and right-hand side, respectively, by the electrode. Regardless their deflection directions, the currents produced by the NW I and II constructively add up. NW III is chosen to elaborate the vibration induced by an ultrasonic wave. As shown in Fig. 39 when the compressive side of NW III is in contact with the electrode, the same discharge process as for NW I occurs, resulting in the flow of current from the electrode into the NW. NW IV, short in height, is in compressive strain by the electrode without bending. In such a case, the piezoelectric voltage created at the top of the NW is negative. Thus, across the electrode–ZnO interface, a positively biased Schottky barrier is formed; hence, the electrons can freely flow across the interface. As a result, electrons flow from the NW into the top zigzag electrode as the deformation occurs. This discharging process, if significant, may also contribute to the measured current. The output current is a sum of those NWs that actively contributing output power, but the voltage of the NG is determined by a single NW because all of the NWs are "in parallel".

The packaged NG was placed in the water bath to measure the closed circuit current and open circuit voltage. The ultrasonic wave of frequency 41 kHz was periodically turned on every other 15 s. Fig. 39 shows the closed circuit current when the ultrasonic wave was turned on and off. The data clearly indicate that the current output was originated from the NG as a result of ultrasonic wave excitation, as the output coincided with the working cycle of the ultrasonic wave generator. A similar pattern in the open circuit

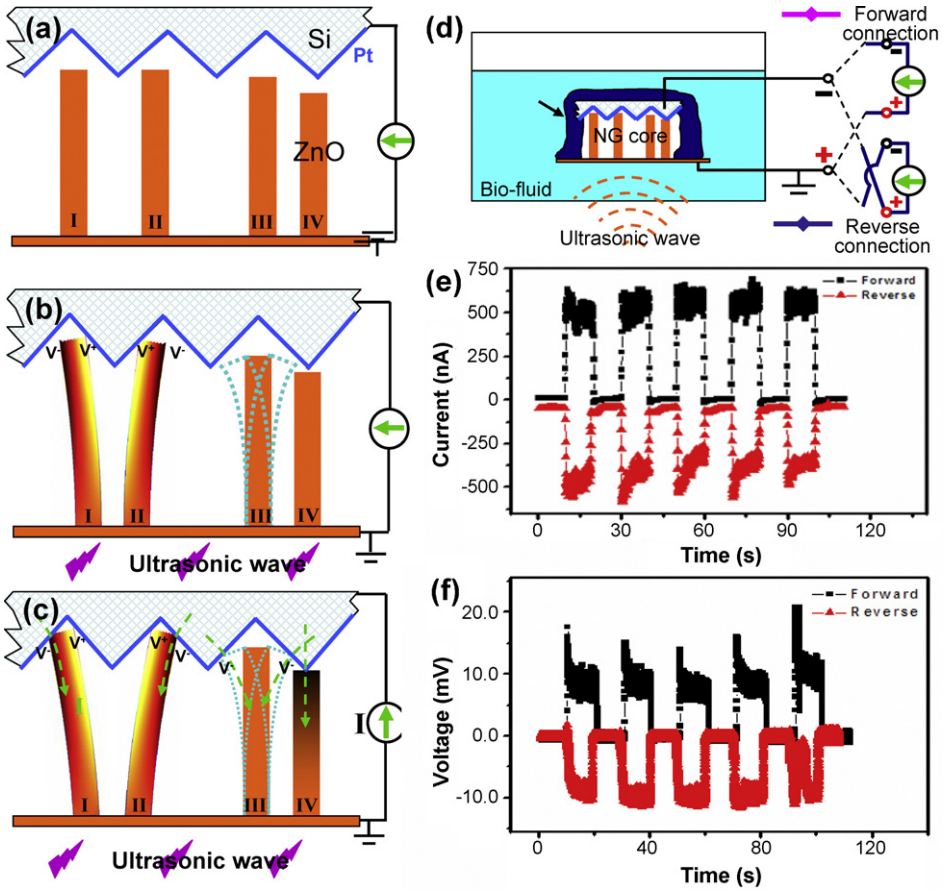

Fig. 39. The mechanism of the nanogenerator driven by ultrasonic wave. (a) Schematic illustration of the zigzag electrode and the four types of representing configurations of the NWs. (b) The piezoelectric potential created across the NW I and II under the push/deflection of the electrode as driven by the ultrasonic wave, but without flow of current due to the reversely biased Schottky barrier at the electrode–NW interface. The NW III is in vibration under the stimulation of the ultrasonic wave. The NW IV is in compressive strain without bending. (c) Once the NWs touches the surface of the adjacent teeth, the Schottky barrier at the electrode–NW interface is forward biased, piezoelectric discharge occurs, resulting in the observation of current flow in the external circuit. (d) Schematic of a NG that operates in bio-fluid and the two types of connections used to characterize the performance of the NG. The pink and blue curves represent signals from forward connected current/voltage (I/V) meter and reversely connected I/V meter, respectively. (e and f) The short circuit current and open circuit voltage measured by the two types of connections when the ultrasonic wave was periodically turned on and off. From [98,99].

voltage output was also observed, as shown in Fig. 39. Both the current and voltage outputs exhibit high levels for this type of NG, with a current ~500 nA and voltage ~10 mV [99]. Considering the effective area of the NG (6 mm^2), it is equivalent to a current generation density of ~8.3 $\mu A/cm^2$. A power generation density of ~83 nW/cm^2 is reported, which shows a great potential to power nanosensors.

It must be pointed out that the operation of the NG does not rely on mechanical resonance as required by some of the energy harvesting technologies, instead it is based on mechanical deflection. Such a design allows the NG to work in a wide range of frequencies, from few Hz, kHz and even to MHz. This large adaptability greatly expands the application of the NG for harvesting various mechanical energies.

5.6.4. Criteria and tests for ruling out artifacts

Measurement of the current and voltage signal generated by a NG is rather challenging, especially at the level of nanoAmpere and milliVolt, because of system and/or environmental interference, such as system capacitance, thermal/instability drifting and the bias of the amplifier. The electrical measurements of NGs is even more complex than conventional transport measurements, because we are looking for the current/voltage that is generated by the NGs rather than the bias current/voltage introduced by the electrical measurement system for detecting the signals. Another challenge comes from the mechanical movement of the components during energy conversion, which could introduce electronic interference and capacitance change. The most frequent cases for an inexperienced researcher are that one observes no output, or with output for any sample. Both unusual cases are likely complicated by artifacts. Extreme caution must be exercised in each step to ensure the signal was generated by the NG instead of the measurement circuits. In many cases, we have built simulating circuits for identifying the sources of artifacts. A key for the measurements is to repeat it for many devices and under different experimental conditions. In the last three years, we have developed three criteria that are consist of 11 tests to identify the true signal from a NG [100].

The first criterion is a transport measurement of the NG. A Schottky or non-symmetric I–V transport property is required for a working NG. A device that has Ohmic transport behavior is ineffective for energy generation.

The second criterion is the "switching-polarity" testing [101]. As illustrate in Fig. 39 the current/voltage meter is first forward connected, e.g., positive and negative probes were connected to the positive and negative electrodes, respectively. Then the connection polarity was reversed, e.g., positive and negative probes connected to negative and positive electrodes, respectively, to the two electrodes of the NG. The corresponding I_{sc} and V_{oc} signals were shown in Fig. 39e and f, respectively. A switch in sign in both current and voltage after switching the connecting polarity is a key test to eliminated the effects from measurement system error and confirm that the power is generated by the NG. Resistors and capacitors are symmetric devices and they cannot produce a reversal in output signal if it is initiated from the measurement system. Diode can only produce one way current signal but zero in the other direction, which cannot result in a reversed current if it is originated from the measurement system.

The third criterion is a linear superposition of the output current/voltage when two or more NGs are connected in parallel/serial. As shown in Fig. 40a and b, two NGs I and II have been measured under the same experimental conditions. The NG I produced an average I_{sc} of ~0.7 nA and NG II generated a signal of 1 nA. These two NGs were then connected in parallel (inset of Fig. 40) and tested under the same condition again. The resultant output current reached an average of ~1.8 nA, which is the sum of the two individual outputs (Fig. 40). This concept was further proved by anti-parallel connecting NG I and NG II (inset of Fig. 40). Since the magnitudes of the I_{sc} of the two NGs were very close, the total current was mostly cancelled out by the "head-to-tail" connection in parallel, and the received signal was around the baseline (Fig. 40), just as expected.

For technological applications, raising the voltage and current output of the NG are essential for raising the output power. The most straightforward way to increase the current/voltage is to put them in parallel/series. This is an approach for raising the output current and voltage. Fig. 41d demonstrates multilayed NGs built on

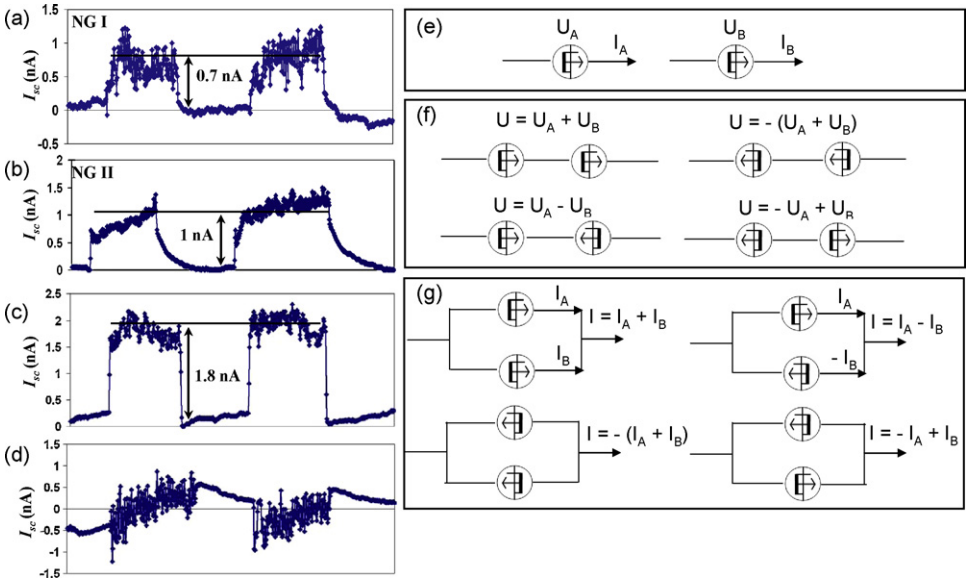

Fig. 40. Criteria adopted for identifying true output signal from artifacts. (a and b) Current signal measured from two individual NG I and II. (c and d) Current signal measured from parallel and anti-parallel connected NG I and NG II, respectively; the connection configurations are schematically shown in the insets. (e) Two NGs with expected output. The symbol presented here represents piezoelectric generator. (f) Four testing configurations for serial connection of two NGs to identify true voltage output signals. (g) Four testing configurations for serial connection of two NGs to identify true current output signals. From [91,101,105].

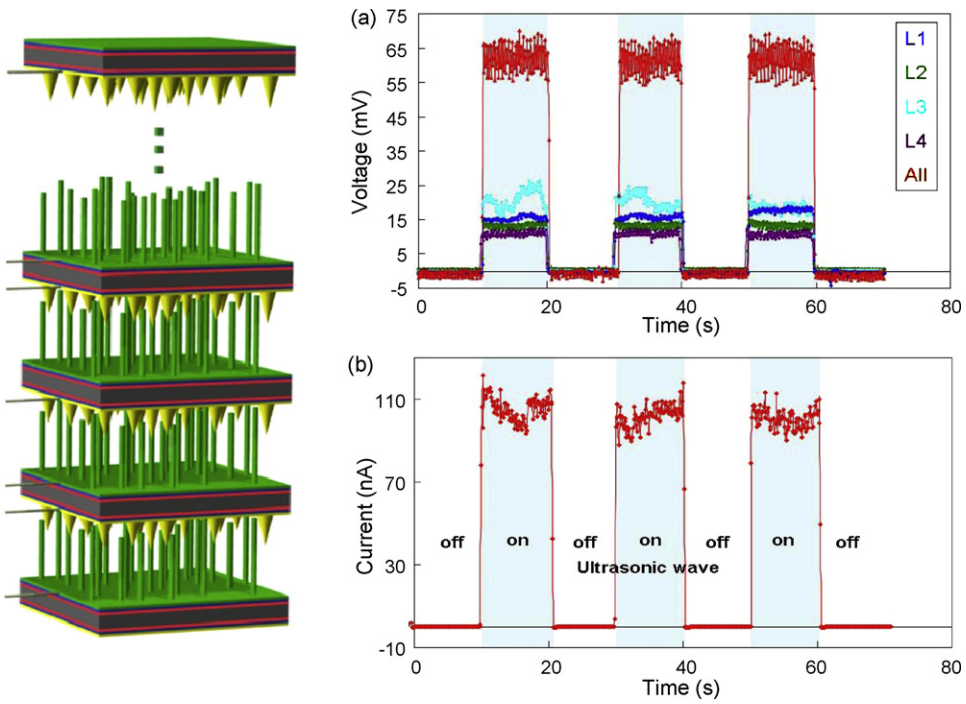

Fig. 41. A multilayered three-dimensional NG integrated by stacking multiple layers of wafer structures. (a) Open circuit voltage output measured from each individual layers and the serially connected four-layer integrated NG. (b) Short circuit current output measured from the serially connected four-layer integrated NG. The regions when the ultrasonic wave was on and off are indicated. The surface area of the NG was 6 mm^2. From [102].

silicon substrates [102]. A series connection of four NGs gives an output voltage of 65 mV. This example also shows the linear superposition of the voltages.

5.6.5. Fiber based nanogenerators

The ceramic or semiconductor substrates used for growing ZnO NWs are hard, brittle and cannot be used in areas that require a foldable or flexible power source, such as implantable bio-sensors in muscles or joints, and power generator built in walking shoes [103]. It is necessary to use conductive polymer/plastics as substrate that is likely to be biocompatible and bio-safe. Two advantages may be offered by this approach. One is the cost-effective, large-scale solution approach used to grow ZnO NW arrays at a temperature lower than 80 °C. The other is the large-degree of choice of flexible plastic substrates used for growing aligned ZnO NW arrays, which could play an important role in the flexible and portable electronics for harvesting low-frequency (~10 Hz) energy from the environment such as body movement (e.g., gestures, respiration, or locomotion).

We have recently demonstrated fiber based NG [104]. The design of the NG is based on the mechanism of utilizing zigzag electrode, but we have replaced the zigzag electrode by an array of metal wires, as shown in Fig. 42. By brushing the metal nanowire arrays across the ZnO nanowire arrays, the metal wires act like an array of AFM tips that induce the mechanical deformation to the ZnO nanowires and collect the charges. A unique advantage for ZnO nanowire arrays is that they can be grown at 80 °C on substrates of any shape and any materials. In reality, the metal nanowire arrays were made by metal coating of ZnO nanowire arrays grown on Kevlar fiber (Fig. 42). In practice, any fiber should work as long as it has a good electrical conductivity. The metal to be coated is required to form a Schottky contact with ZnO. Entangling the two fibers, one coated with Au and one without coating, sets the principle of the fiber based NG (Fig. 42). The NWs on the two fibers are "teeth-to-teeth" (Fig. 42), a relative deflection by a distance as short as a NW size is sufficient to generate electricity. A cycled relative sliding between the two fibers produces output voltage and current owing to the deflection and bending of the ZnO nanowires (Fig. 42). This is the fiber based NG, with potential for harvesting energy from body movement, muscle stretching, light wind and vibration. It establishes the basis for building "power-shirt".

5.6.6. Nanogenerator using laterally packaged nanowires

In the piezoelectric NW generators the vertically aligned ZnO NWs function through a bending motion induced by a zigzag electrode above the NW arrays. The electrode is typically 50–100 nm away from the NW array but through an external force or disturbance, it can move up, down or laterally forcing the nanowires to bend, and thus inducing a voltage. The contact between the electrode and the NWs is transiently on and off for each cycle of the driving action, and a relative scrubbing and sliding between the two is purposely designed, which may result in wearing, increased contact resistance/instability, and liquid/vapor infiltration.

We have recently developed a nanogenerator using a nanowire that is affixed at the two ends on a flexible substrate [105]. In this design, a PFW is laterally lay down on a substrate and is fixed at both ends to electrodes (Fig. 43). To measure the electric energy generated by the PFW when subjected to mechanical deformation, a periodic mechanical bending was introduced to the substrate using a motor driven mechanical arm (Fig. 43). The final bend radius of the substrate was ~2 cm, which is much larger than the length of the PFW. The bending of the substrate film induced a tensile strain of 0.05–0.1% in the PFW attached to its outer surface. Due to the piezoelectric property of ZnO, a piezoelectric potential field was created along the PFW, which drove the flow of electrons in the external circuit (or interconnects). When the substrate was periodically bent and released, the PFW was periodically stretched and released, resulting in an alternating current (Fig. 43). The entire structure has been packaged inside a thin layer of insulating wax or flexible polymer to maintain its physical stability during the deformation of the substrate.

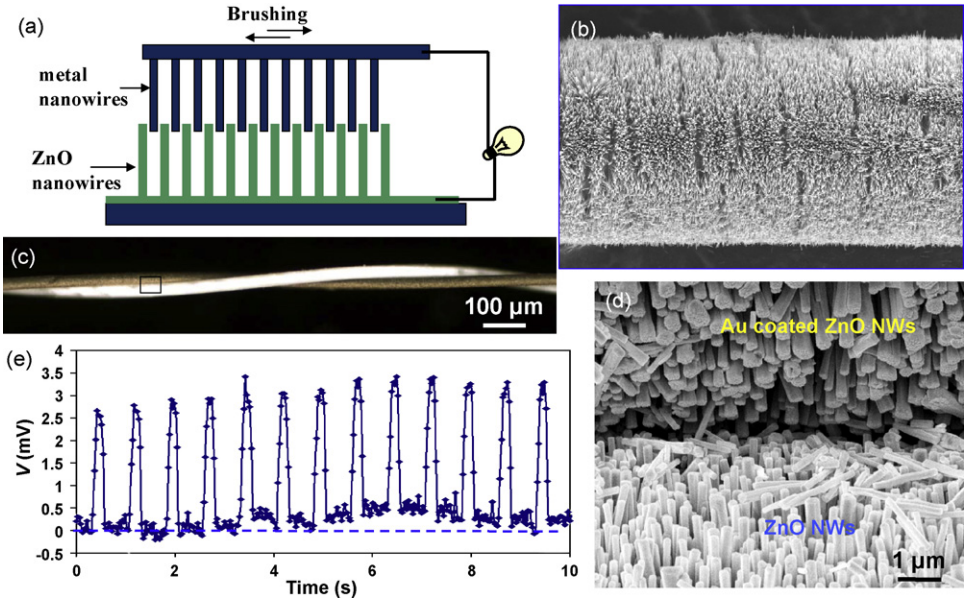

Fig. 42. The design and mechanism of the fiber based nanogenerator as driven by a low-frequency, external vibration/friction/pulling force. (a) Schematic idea of "two-brush" nanogenerator. One brush is made of ZnO nanowires and the other brush is metal nanowires. (b) SEM image showing the distribution of NWs grown on a fiber surface. (c) An optical micrograph of a pair of entangled fibers, one of which is coated with Au (in darker contrast). (d) SEM image at the "teeth-to-teeth" interface of two fibers covered by NWs, with the top one coated with Au. The Au coated NWs at the top serve as the conductive "tips" that deflect/bend the NWs at the bottom, a piezoelectric-semiconducting couple process generates electric current. (e) The piezoelectric potential output by the two-fiber nanogenerator under the pulling and releasing of the top fiber by an external force. From [104].

Before and after a single wire generator (SWG) was tested for generating electricity, its transport property was characterized to understand its performance and signal output. For a working SWG that was effective for producing output power, the I–V characteristic always showed a Schottky behavior (Fig. 43c). This is the most outstanding characteristic of a good SWG. To properly represent the location of the Schottky barrier in the schematic diagram, a diode symbol is introduced at the left-hand side for notation purpose, in reference to which the sign of the output signal is defined. For the discussions hereafter, we define the side that has the Schottky diode as the positive side of the SWG.

The working principle of the SWG is proposed based on the band structure of the system with the presence of a Schottky barrier and the creation of an inner piezoelectric field in the PFW under tensile strain [105]. The ZnO piezoelectric fine wires (PFWs) used in our experiments are oriented along *c*-axis. It is known that

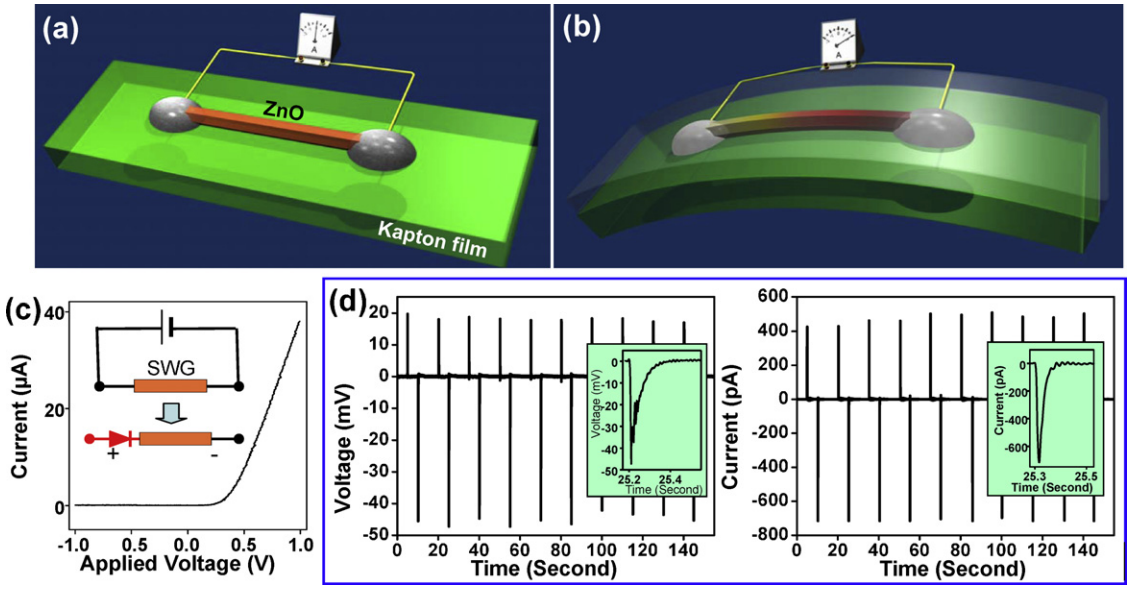

Fig. 43. Design of a piezoelectric fine-wire generator on a flexible substrate. (a) The PFW lays on a polymer Kapton film substrate, and its two ends are tightly bonded to the substrate and outlet interconnects. (b) Mechanical bending of the substrate creates tensile strain and corresponding piezoelectric potential in the PFW, which drives the flow of the electrons through the external load. (c) I–V characteristic of a SWG that is effective for producing output power, showing a typical Schottky diode characteristic. In our study, the end-contact of the SWG that has the Schottky behavior is defined to be positive, where a diode symbol is introduced to represent its presence at the interface (lower diagram). (d) Generated alternating voltage and current of a SWG when repeatedly stretched and released. The insets are an enlarged output voltage and current peak. From [105].

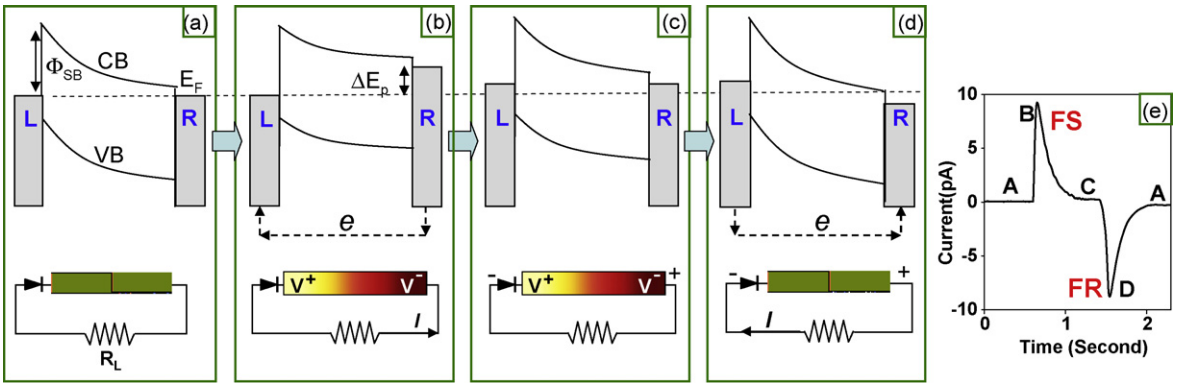

Fig. 44. Charge generation and outputting mechanism of an alternating-current single wire generator illustrated by energy band diagram. (a) Energy band diagram of a ZnO PFW contacted with two metal electrodes, where CB and VB are the conduction band and valence band of ZnO PFW, respectively. The low diagram is a sketch of the realistic measurement circuit, where a small load resistor R_L is introduced, which is much smaller than the resistance of the PFW and/or the contacts. (b–d) Energy band diagrams of the SWG when the PFW is tensile stretched, re-reaches equilibrium, and then released, respectively, showing the generation of a pair of positive and negative voltage/current peaks (see text) for a case in which the piezoelectric potential of the PFW is assumed higher at the side next to the Schottky barrier, while the other side with Ohmic contact has a lower piezoelectric potential. (e) An experimentally measured output current from a SWG, in which the output regions corresponding to the processes shown in subparts a–d are indicated by the corresponding labels a–d. From [105].

the (0 0 0 1) and (0 0 0 $\bar{1}$) facets of ZnO are terminated with Zn and oxygen, respectively. An energy band diagram is shown in Fig. 44a for a ZnO PFW in contacting with metal electrodes of Fermi level E_F, with a Schottky barrier of height Φ_{SB} at the left-hand (L) side and Ohmic contact at the right-hand (R) side. The Schottky barrier is introduced to represent a high local-contact-resistance in the order of ~50–1000 MΩ for "blocking" the flow of electrons through the microwire. The Schottky barrier is represented by a diode symbol. In the first step, once subjecting to tensile strain, a piezoelectric field is created in the PFW (Fig. 44b), which is the result of ionic charges that are associated with the polarization of atoms in the crystal and cannot freely move. The piezoelectric charges remain in the PFW for at least a few seconds or even much longer without "depletion" by the free carriers as long as the strain is preserved. In the first case, we assume that the piezoelectric potential is positive V^+ at the Schottky barrier side and is negative V^- at the Ohmic side (assuming $V^+ > V^-$). In such a case, the conduction band and Fermi level of the electrode at the R side is raised for $\Delta E_p = e(V^+ - V^-)$ in reference to that of the L electrode. Thus, electrons will flow from the R side electrode to the L side through an external load R_L because the resistance across the Schottky barrier is very high when the local voltage is less than the forward threshold voltage of the diode even at positive bias. The electrons accumulate at the interfacial region between the L electrode and ZnO PFW due to the presence of the Schottky barrier. This process continues until the potential created by the accumulated electrons balance the piezoelectric potential, thus, the Fermi levels of the two electrodes reach a new equilibrium (Fig. 44c). This is the process of generating the first positive output current/voltage peak in Fig. 44e.

In the second step, when the polymer substrate is released, the tensile strain in the PFW is released as well. An immediate disappearance of the piezoelectric potential lowers the Fermi surface of the R electrode by ΔE_p, accompanying to which the electrons originally accumulated at the interfacial region between the L electrode and the PFW flew back through the external circuit to the R electrode due to the presence of the Schottky barrier at the interface (Fig. 44d). This process ends when the Fermi levels at the two electrodes are at equilibrium and the system returns to the original status as shown in Fig. 44a. This is the process of generating the negative output current/voltage peak presented in Fig. 44e. The total electrons transported in the two steps are the same regardless the straining process, provided there is no current leakage. A repeat of the last two steps produces an alternating output.

In the current generation process, the role played by the Schottky barrier is as a "gate" that prevents the flow of the electrons in the external circuit through the PFW so that the piezoelectric potential is preserved. The barrier height of the "gate" can be in the order of that for an insulator, which is also effective for directing the electrons to flow in external circuit. The Schottky contact can be at one side or at both sides of the PFW. The PFW acts like a "capacitor" and "charge pump", which drives the back and forth flow of the electrons in the external circuit to achieve a charging and discharging process when the PFW is stretched and released, respectively. This means that the electrons will not flow through the PFW, but back and forth in the external load. Therefore, the generated voltage does not need to exceed a critical value in order for the device to work. When the PFW is stretched as driven by bending of the substrate, a piezoelectric-potential-drop is created along the PFW, which raises the Fermi level of the electrode at the low-potential (LP) side and drives the forward-flow of electrons from the LP side through the external circuit to the high-potential (HP) side to balance the Fermi levels of the two electrodes. When the PFW is released, the disappearance of the piezoelectric potential in the PFW lowers the Fermi level of the LP side, leading to a back-flow of the electrons from the HP side to the LP side. A repeated stretching-releasing of a single PFW creates a transient voltage up to ~50 mV. This is the working mechanism of the generator.

It must be pointed out that the laterally bonded NG can easily generate artifact. Caution must be exercised for identifying true signals. We have developed three criteria and 11 tests that are effective for identifying true signals [100].

5.6.7. Muscle/movement driven nanogenerator

A living species has numerous sources of mechanical energy, such as muscle stretching, arm/leg swings, walking/running, heart beats and blood flow. We demonstrate a piezoelectric nanowire based nanogenerator that converts biomechanical energy, such as the movement of a human finger and the body motion of a live hamster (Campbell's dwarf), into electricity [106]. A single wire generator (SWG) consists of a flexible substrate with a ZnO nanowire affixed laterally at its two ends on the substrate surface. Muscle stretching results in the back and forth stretching of the substrate and the nanowire. The piezoelectric potential created inside the wire leads to the flow of electrons in the external circuit. The output voltage has been increased by integrating multiple SWGs. Utilizing this type of SWG, we have demonstrated energy

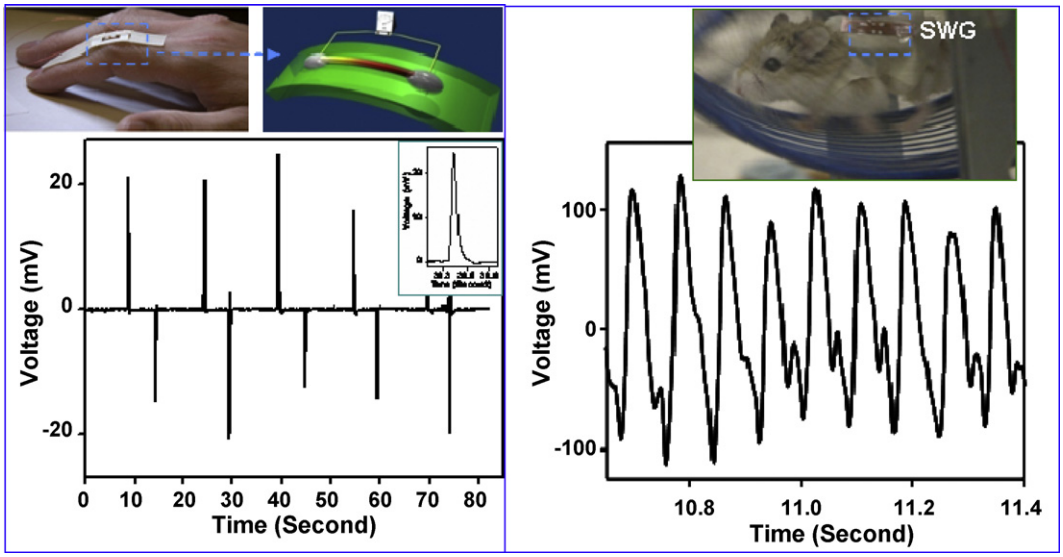

Fig. 45. Dynamic muscle movement driven nanogenerators utilizing the flicking of a single human finger (left) and a running hamster. A repeated mechanical deformation of a piezoelectric wire produces "AC" current/voltage in an external circuit. This demonstrate the potential of using body movement for power small electronic devices [106].

harvesting from finger movement and a running hamster (Fig. 45). A series connection of four SWGs produced an output voltage of up to ~0.1–0.15 V. The success of energy harvesting from a tapping finger and a running hamster reveals the potential of using the nanogenerators for scavenging low-frequency energy from regular and irregular biomotion.

5.7. Nano-piezotronics

The concept of nanopiezotronics was first introduced in December 2006 [107], and its definition and detailed description were published in 2007 [108,109]. The basis of nanopiezotronics is to use the coupled piezoelectric and semiconducting properties of nanowires and nanobelts for designing and fabricating electronic devices and components, such as field effect transistors and diodes. We now illustrate a few components of such devices, based on which we will introduce the principle of piezotronics.

5.7.1. Piezoelectric field effect transistors

Field effect transistor (FET) based on nanowire/nanotube is one of the most studied nanodevices. A typical NW FET is composed of a semiconducting NW that is connected by two electrodes at the ends and is placed on a silicon substrate covered by a thin layer of gate oxide. A third electrode is built between the NW and the gate oxide (Fig. 46). The gate voltage can trap and deplete the carriers in the NW, thus controlling the gate voltage can effectively gate the flow of the current from the source to drain electrode. An NW based sensor is a source-drain structured NW FET without a gate, thus, a large portion of the NW is exposed to the environment. The mechanism of NW sensors for sensing gases, bio-molecules or even virus relies on the creation of a charge depletion zone in the semiconductor NW by the surface adsorbed sensing targets [110].

A piezoelectric potential is created across the NW when it is deflected by an external force. If the potential is large enough, it can play the role as the gate voltage for FET. By connecting a ZnO NW across two electrodes that can apply a bending force to the NW, the electric field created by piezoelectricity across the bent NW serves as the gate for controlling the electric current flowing through the NW (Fig. 46) [111]. Once deformed by an external force, a piezoelectric potential is built across the bent NW, some free electrons in the n-type ZnO NW may be trapped at the positive side surface and become non-mobile charges, thus, lowering the effective carrier density in the NW. It is important to note that the trapped "free-charges" cannot deplete the charges produced by piezoelectric effect, which are rigid, ionic and affixed to the atoms. On the other hand, even the positive potential side could be partially screened by the trapped electrons, the negative potential side remains unchanged. The free electrons will be repulsed away by the negative potential and leave a charge depletion zone around the compressed side surface. Consequently, the width of the conducting channel in the ZnO NW becomes smaller and smaller while the depletion region becomes larger and larger with the increase of the NW bending. The resultant effect is a drastic decrease in conductivity of the NW. This is the proposed piezoelectric-FET (PE-FET).

The experimental demonstration of the PE-FET is shown in Fig. 46. A large ZnO wire was in contact with two electrodes. Its transport property was characterized as the wire was bent. Fig. 46 shows the corresponding I–V curves measured when the wire was bent into shapes shown in Fig. 46(I–V), respectively. It is clear that the conductance of the NW was reduced for more than ten times after bending. Such an effect was attributed to the gating effect of the piezoelectric potential.

5.7.2. Piezoelectric diode

Piezoelectric-field gated diode was demonstrated using a two-probe technique [112]. One probe held one end of a NW that laid on an insulator substrate, the other probe pushed the NW from the other end by in-contact with the tensile surface. The W tips had Ohmic contact with the NW. The I–V curve changed from a linear shape to a rectifying behavior with the increase of the degree of NW bending (Fig. 47a). This is the piezoelectric-diode (PE-diode).

The rectifying/switching behavior of the PE-diode can be explained from the band diagram shown in Fig. 47. Applying an external voltage of V_o between the tip (T) and the root (R) of the NW creates a difference in Fermi levels between the tip and the root-electrode, with the root in positive (Fig. 47b). When the tip pushes the NW from the tensile side, a positive voltage V^+ and negative voltage V^- are generated at the tensile and compressive surfaces, respectively, thus, the energy level of the conduction band of the NW next to the tip was lowed by qV^+, with q the unit charge of the electron (Fig. 47c). In such a case, electrons can easily flow from the tip side to the root side without experiencing any

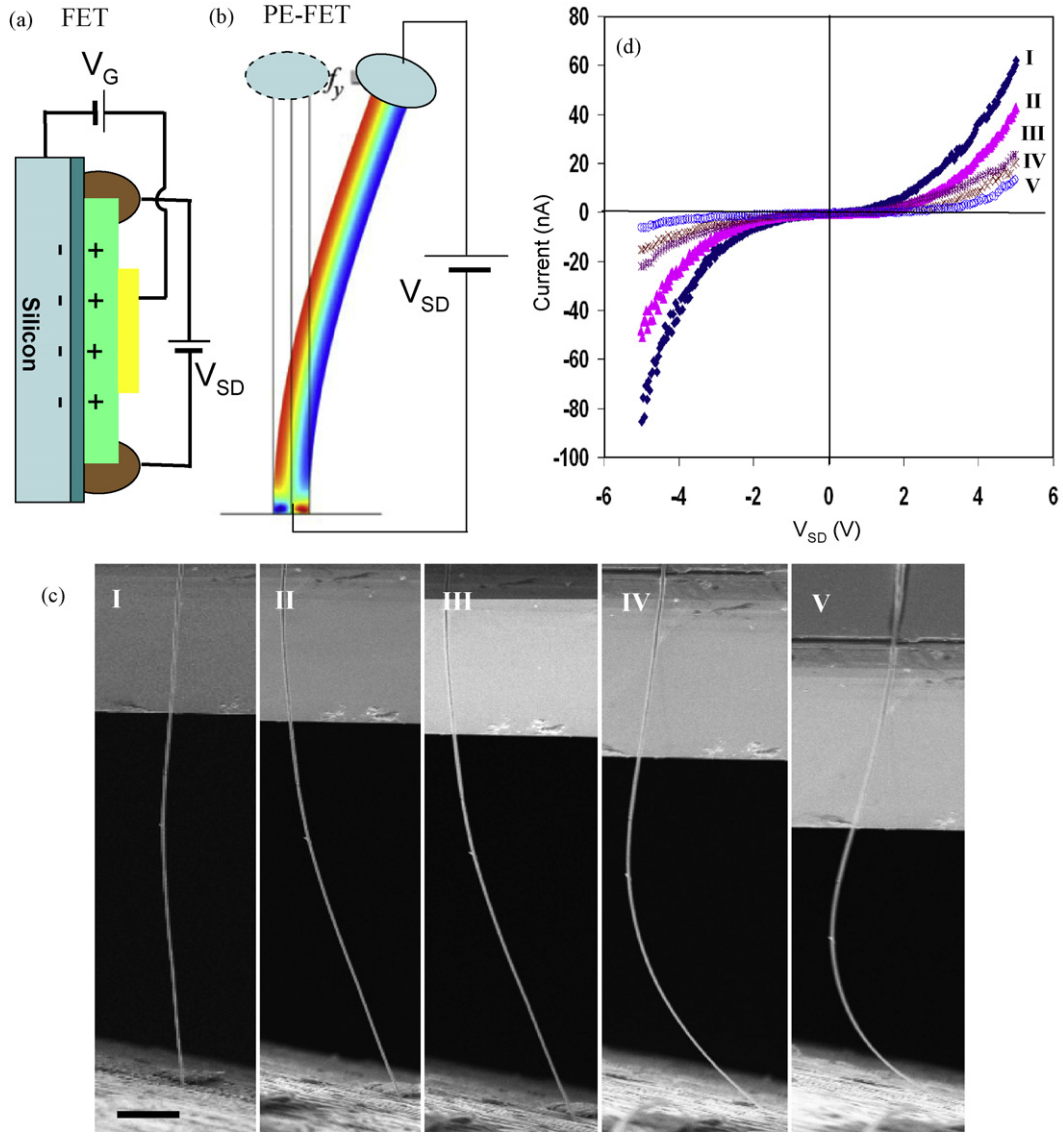

Fig. 46. The physical principle of the piezoelectric-field effect transistor. (a) Schematics of a conventional field effect transistors using a single nanowire/nanobelt, with gate, source and drain. (b) The principle of the piezoelectric-field effect transistor, in which the piezoelectric potential across the nanowire created by the bending force f_y replaces the gate as in conventional FET. The contacts at the both ends are Ohmic. (c) SEM images with the same magnification showing the five typical consecutive bending cases of a ZnO wire; the scale bar represents 10 μm. (d) Corresponding I–V characteristics of the ZnO nanowire for the five different bending cases. From [111].

barrier, thus, the transport preserves the Ohmic behavior. This is the "forward" bias of the PE-diode.

By switching the polarity of the applied voltage so that the tip has a higher voltage, the Fermi level of the tip is lowed by qV_o in reference to that of the root-electrode. Correspondingly, for a case $V_0 < V^+$, a barrier of height $q(V^+ - V_0)$ was created for the electrons to flow from the NW to the tip. The transition probability via thermal emission is $\exp[-q(V^+ - V_0)/kT]$. Thus for $V_0 < V^+$, the current decays quickly. This is the "reversed" bias of the PE-diode. The threshold of the diode increases with the increase of NW bending.

5.7.3. Polarity switchable piezoelectric diode

We have reported a new type flexible piezotronic switch device that is built using a single ZnO piezoelectric fine wire (PFW) (nanowire, microwire) [113]. Its operation mechanism relies on the piezoelectric potential induced asymmetric change in Schottky-barrier height (SBH) at the source and drain electrodes. The device was fabricated by bonding an ultra-long ZnO PFW laterally on a polystyrene (PS) substrate, which has a thickness much larger than the diameter of the PFW, as schematically shown in the upper-inset of Fig. 48a. A single ZnO PFW (typical diameter of several micrometers and length of several hundred micrometers to several millimeters) was placed on PS substrate (typical length of ~3 cm, width of ~5 mm and thickness of 1 mm) by using a probe station under optical microscopy. Then silver paste was applied at both ends of the ZnO PFW to fix its two ends tightly on the substrate, silver paste was also used as the source and drain electrodes. After the silver paste was dried, a thin layer of polydimethylsiloxane (PDMS) was used to package the device.

Before the electromechanical measurements, we have first tested the original I–V characteristic of the device. The corresponding I–V behaviors under each straining condition are shown in Fig. 48b. When the device was under tensile straining, upward diode-like I–V behaviors was observed (red line); downward diode-like I–V behavior (green line) was observed when the device was under compressive straining. The I–V curve (black line in Fig. 48b) fully recovered when the strain was relieved.

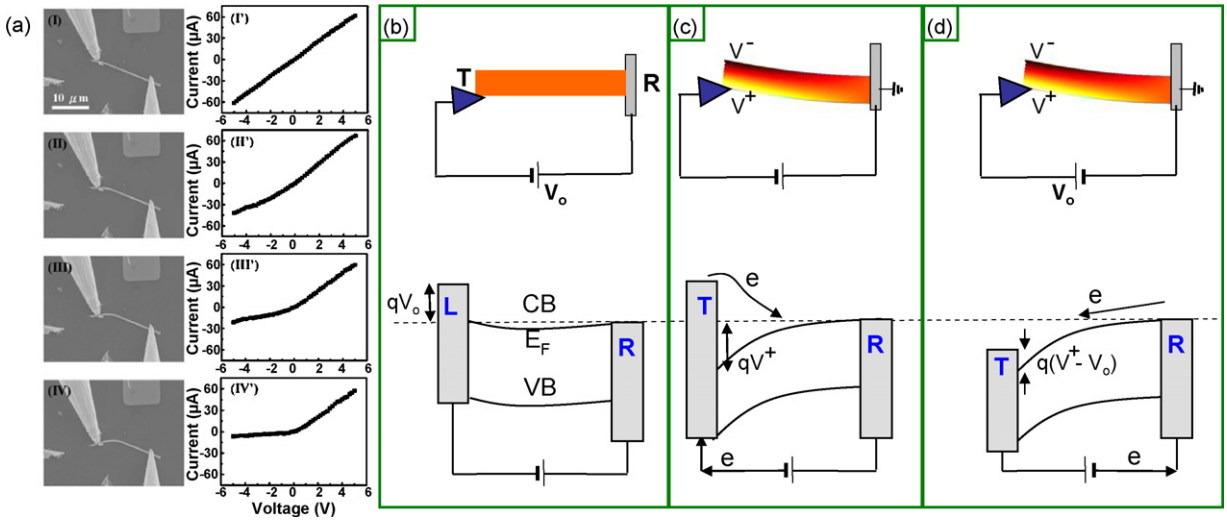

Fig. 47. The principle of the piezoelectric-field diode, in which one end is fixed and enclosed by a metal electrode, and the other end is bent by a moving metal tip. Both ends have Ohmic contact with ZnO. (a) A sequence of SEM images of a ZnO wire at various bending angles and the corresponding I–V characteristic, with the fixed probe at positive and the moving tip negative. (b) Band diagram of a NW that has Ohmic contact at the two ends when a constant voltage V_o is applied, with the tip (T) as negative and root (R) positive. The Fermi level of the tip is raised by qV_o. (c) Once the NW is pushed by the tip, a local positive piezoelectric potential at the tensile surface lows the conduction band next to the tip, resulting in a forward flow of electrons from the tip through the NW to the root. This is the forward bias case. (d) When the applied voltage is switched in polarity, the Fermi level of the tip is lowered by qV_o. A potential barrier of height $q(V^+ - V_o)$ is created. Once the applied voltage $V_o < V^+$, the electrons have to transit over the barrier to reach the tip. This is the reversely biased case. From [91,112].

Here we use a schematic energy band diagrams to illustrate how piezoelectric polarization affect the Schottky barriers at the source and drain contacts [114]. Fig. 48c shows an unstrained device with the *c*-axis of ZnO pointing towards the source. When the device is under compressed strain, a piezoelectric potential is built inside the nanowire. For a case that the drain has a higher piezoelectric potential (see Fig. 48d), a higher SBH is created at the source side, resulting in a diode effect that allows the electrons to

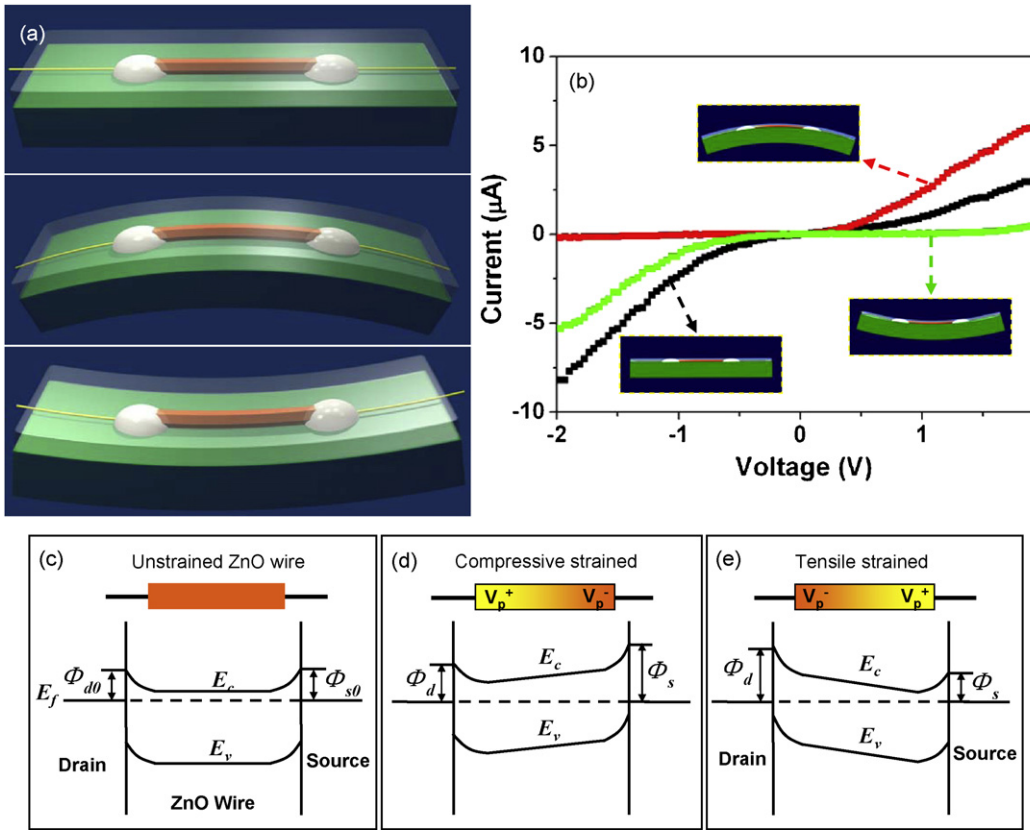

Fig. 48. (a) Polarity switchable piezoelectric diode using a two-end bonded ZnO wire. (b) Typical I–V characteristics of the sensor under different compressive strains. Black line is the I–V curve without strain. The direction of the blue arrowhead indicates the increasing of applied compressive strain. Schematic energy band diagrams illustrating the Schottky barriers at the source and drain contacts of a unstrained (c), compressive strained (d), and tensile strained (e) PFW, which illustrates the effect of switching the piezoelectric potential either by strain or by wire orientation on the local band structure and SBH. From [113].

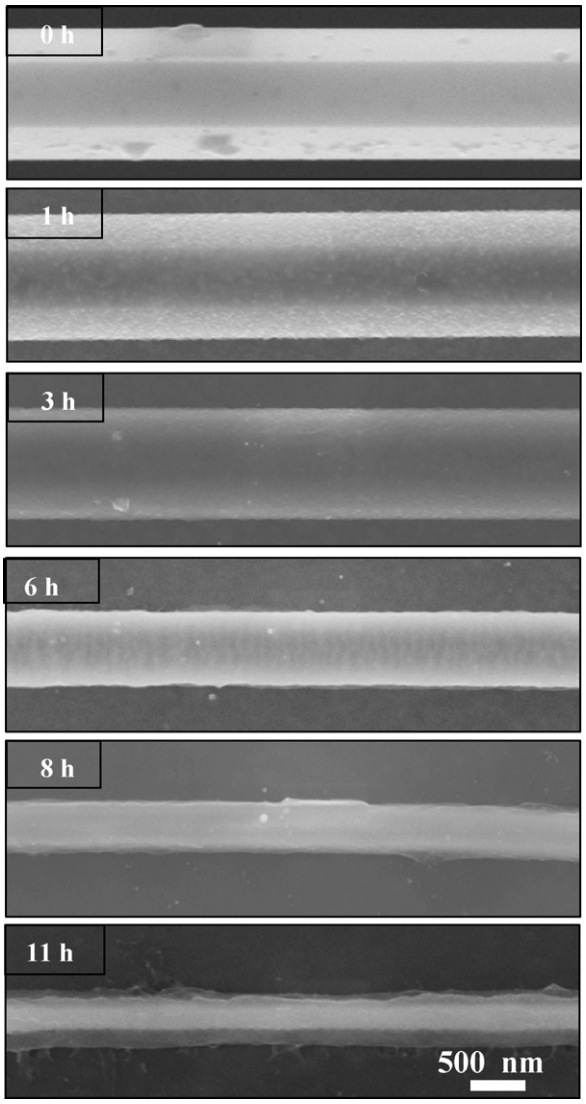

Fig. 49. SEM images of a ZnO wire that has interacted with horse blood serum solution (10% concentration, pH ~7.9–8.2) for different lengths of time. From [115].

flow only from the drain to the source side. Alternatively, by changing the compressive straining to tensile straining simply by changing the bending direction of the PS substrate, the piezoelectric potential-drop in the PFW reverses, as shown in Fig. 48c, leading to a higher SBH at the drain side. This allows the electrons to flow only from the source to drain side.

6. Biodegradability and biosafety

In parallel of exploring the exciting physical and chemical properties of NWs and NBs, it is also required to study their biosafety, biocompatible and bio-degradability. But very limited literatures are available. Recently, we present the first study on bio-degradability and biocompatibility of ZnO wires/belts [115]. A systematic study about the etching and dissolving behavior ZnO wires in various solutions with moderate pH values, including deionized water, ammonia, NaOH solution, and horse blood serum. The result shows that ZnO can be dissolved by deionized water (pH ~ 4.5–5.0), ammonia (pH ~ 6.8–7.1, 8.7–9.0) and NaOH solution (pH ~ 6.8–7.1, 8.7–9.0). The study of interaction of ZnO wires with horse blood serum shows that the ZnO wires can survive in the fluid for a few hours, and then they will degrade in the horse blood serum into mineral ions.

Fig. 49 shows SEM images of an ZnO wire that had been dipped into diluted horse blood serum (10% concentration, pH ~ 7.9–8.2) with NaOH for 0, 1, 3, 6,8 and 11 h, respectively. After 1 h in the solution, there is no visible etching on the wire surface except some adsorbed species (Fig. 49b). The etching became severe after 3 h of interaction, as indicated by the reduced wire diameter. After etching for 11 h, ~94% volume of the ZnO wire was dissolved. We estimated that no more than 12 h, the ZnO wire would be totally etched by the horse blood serum.

Recently, we report the first cellular level study on the biocompatibility and biosafety of ZnO nanowires (NWs) [116]. We found that ZnO NWs are biocompatible and biosafe to the two cell lines (Fig. 50). The viabilities of Hela cells cultured with NWs for 12 and 24 h showed no difference. The 48 h cultured cells showed only a slight reduction in viability at a high concentration of 100 μg/ml (Fig. 50a). More than 95% of the Hela cells were alive after the test, and there was no significant difference in viability among the plates of three time groups. In the 48-h MTT experiment with the highest NW concentration of 100 μg/ml, the viability of the Hela cells was a litter lower than that of the sample without NWs, but the viability was still more than 75% (Fig. 50a). For 96-well plates of planting L929 cells, the viabilities showed some variations (Fig. 50b). For the 12-h plate, the viability of L929 cells was lower than those of the other two 24 and 48 h time-sequence plates, indicating that the L929 cell was in a frail period and more sensitive to ZnO NWs when it was first cultured for less than 12 h. After the culturing time exceeded 12 h, the viability of the cells remained strong and was better than 95% even at relatively high NWs concentration. However, the viability of the cells dropped significantly when the NW concentration reached 100 μg/ml. Therefore, the NWs are considered to be completely biocompatible and biosafe at NWs concentration lower than 100 μg/ml. Our study shows the biocompatibility and biosafety of ZnO NWs when

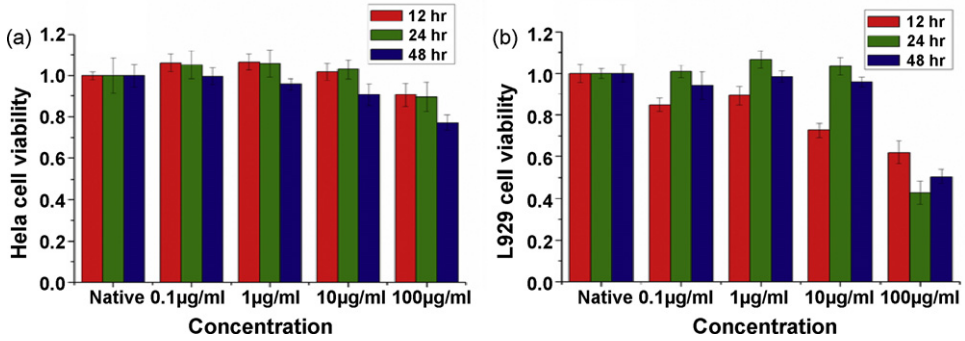

Fig. 50. Cell viability tested by in vitro cellular viability test (MTT) method as a function of ZnO NW concentration and time. (a) Cell viability of Hela cell line in MTT test, cultured with different concentration of ZnO NWs for 12 h, 24 h, 48 h. (b) Viability of L929 cell line in MTT test, cultured with different concentrations of ZnO NWs for 12 h, 24 h, 48 h. From [116].

they are applied in biological applications at normal concentration range.

7. Summary

Nanowires and nanobelts of ZnO are important one-dimensional nanostructures that have important applications in nanotechnology. This review focuses on some updated progresses on the synthesis, characterization and application of ZnO nanowires and nanobelts. Rational synthesis is the fundamental of their technological applications, with a high degree control on the location, the orientation, the distribution, and uniformity. Fundamental understanding about their properties and novel devices can be carried out using single nanowires, which are beautiful illustration of the state-of-art science. For technological applications, a great need is to develop device arrays utilizing the nanowire arrays grown either vertically or laterally. The easy and low cost growth of ZnO nanowires and nanobelts sets the foundation as cutting-edge technologies.

Acknowledgements

Thanks to Y. Ding, P.X. Gao, J.H. Song, X.D. Wang, R.S. Yang, J. Zhou, Y. Qin, S. Xu, Y.G. Wei, C.S. Lao, W.J. Mai, X.Y. Kong, W. Hughes, J. Liu, Y.F. Gao, J.H. He, Z. Li, C. Xu, C. Li and all of our prior and current group members and our collaborators for their contributions to the work reviewed in this article. We acknowledge generous support from DARPA, NSF, DOE, NASA and NIH.

References

[1] T.W. Odom, J.L. Huang, P. Kim, C.M. Lieber, Nature 391 (1998) 62.
[2] H. Dai, J. Kong, C. Zhou, N. Franklin, T. Tmobler, A. Cassell, S. Fan, M. Chapline, J. Phys. Chem. B 103 (1999) 11246.
[3] S.J. Tans, R.M. Verschueren, C. Dekker, Nature 393 (1998) 49.
[4] M.S. Fuhrer, J. Nygrad, L. Shih, M. Forero, Y.G. Yoon, M.S.C. Mazzoni, H.J. Choi, J. Ihm, S.G. Louie, A. Zettl, P.L. McEuen, Science 288 (2000) 494.
[5] P.G. Collins, M.S. Arnold, P. Avouris, Science 292 (2001) 706.
[6] A.M. Morales, C.M. Lieber, Science 279 (1998) 208.
[7] X. Duan, Y. Huang, Y. Cui, J. Wang, C.M. Lieber, Nature 409 (2001) 66.
[8] Y. Cui, C.M. Lieber, Science 291 (2001) 851.
[9] Y. Huang, X. Duan, Y. Cui, L. Lauhon, K. Kim, C.M. Lieber, Science 294 (2001) 1313.
[10] Z.W. Pan, Z.R. Dai, Z.L. Wang, Science 209 (2001) 1947.
[11] Z.R. Dai, Z.W. Pan, Z.L. Wang, Adv. Funct. Mater. 13 (9) (2003) 9.
[12] X.Y. Kong, Z.L. Wang, Nano Lett. 3 (2003) 1625.
[13] Physics World, October (2008) 36.
[14] J. Jagadish, S.J. Pearton (Eds.), Zinc Oxide Bulk, Thin Film and Nanostructures, Elsevier, 2006.
[15] X.Y. Kong, Z.L. Wang, Appl. Phys. Lett. 84 (2004) 975.
[16] X.Y. Kong, Y. Ding, R.S. Yang, Z.L. Wang, Science 303 (2004) 1348.
[17] P.X. Gao, Y. Ding, W.J. Mai, W.L. Hughes, C.S. Lao, Z.L. Wang, Science 309 (2005) 1700.
[18] C.M. Lieber, Z.L. Wang, MRS Bull. 32 (2007) 99.
[19] J.G. Lu, P.C. Chang, Z.Y. Fan, Mater. Sci. Eng. R-Rep. 52 (2006) 49.
[20] Y.W. Heo, D.P. Norton, L.C. Tien, Y. Kwon, B.S. Kang, F. Ren, S.J. Pearton, J.R. LaRoche, Mater. Sci. Eng. R 47 (2004) 1.
[21] N. Wang, Y. Cai, R.Q. Zhang, Mater. Sci. Eng. R 60 (2008) 1.
[22] Z.L. Wang, J. Nanosci. Nanotechnol. 8 (2008) 27.
[23] X.D. Wang, J.H. Song, Z.L. Wang, J. Mater. Chem. 17 (2007) 711.
[24] O. Dulub, L.A. Boatner, U. Diebold, Surf. Sci. 519 (2002) 201.
[25] B. Meyer, D. Marx, Phys. Rev. B 67 (2003) 035403.
[26] P.W. Tasker, J. Phys. C: Solid State Phys. 12 (1979) 4977.
[27] O. Dulub, U. Diebold, G. Kresse, Phys. Rev. Lett. 90 (2003) 016102.
[28] A. Wander, F. Schedin, P. Steadman, A. Norris, R. McGrath, T.S. Turner, G. Thornton, N.M. Harrison, Phys. Rev. Lett. 86 (2001) 3811.
[29] V. Staemmler, K. Fink, B. Meyer, D. Marx, M. Kunat, S. Gil Girol, U. Burghaus, Ch. Woll, Phys. Rev. Lett. 90 (2003) 106102.
[30] R.S. Yang, Y. Ding, Z.L. Wang, Nano Lett. 4 (2004) 1309.
[31] Y. Ding, X.Y. Kong, Z.L. Wang, Phys. Rev. B 70 (2004) 235408.
[32] Y. Ding, Z.L. Wang, Micron, published online.
[33] M.H. Huang, S. Mao, H. Feick, H.Q. Yan, Y.Y. Wu, H. Kind, E. Weber, R. Russo, P.D. Yang, Science 292 (2001) 1897.
[34] X.D. Wang, C.J. Summers, Z.L. Wang, Nano Lett. 3 (2004) 423.
[35] X.D. Wang, J.H. Song, P. Li, J.H. Ryou, R.D. Dupuis, C.J. Summers, Z.L. Wang, J. Am. Chem. Soc. 127 (2005) 7920.
[36] J.H. Song, X.D. Wang, E. Riedo, Z.L. Wang, J. Phys. Chem. B 109 (2005) 9869.
[37] X.D. Wang, J.H. Song, C.J. Summers, J.H. Ryou, P. Li, R.D. Dupuis, Z.L. Wang, J. Phys. Chem. B 110 (2006) 7720.
[38] P.X. Gao, Z.L. Wang, J. Am. Chem. Soc. 125 (2003) 11299.
[39] H.C. Hsu, Y.K. Tseng, H.M. Cheng, J.H. Kuo, W.F. Hsieh, J. Cryst. Growth 261 (2004) 520.
[40] T. Ma, M. Guo, M. Zhang, Y.J. Zhang, X.D. Wang, Nanotechnology 18 (2007) 035605.
[41] S. Xu, C.S. Lao, B. Weintraub, Z.L. Wang, J. Mater. Res. 23 (2008) 2072.
[42] J. Zhang, L.D. Sun, X.C. Jiang, C.S. Liao, C.H. Yan, Cryst. Growth Des. 4 (2004) 309.
[43] L. Vayssiere, Adv. Mater. 15 (2003) 464.
[44] V. Gupta, P. Bhattacharya, Y.I. Yuzuk, K. Sreenivas, R.S. Katiyar, J. Cryst. Growth 287 (2006) 39.
[45] S. Xu, Y.G. Wei, M. Kirkham, J. Liu, W.J. Mai, R.L. Snyder, Z.L. Wang, J. Am. Chem. Soc. 130 (2008) 14958.
[46] Y. Qin, R.S. Yang, Z.L. Wang, J. Phys. Chem. C 112 (2008) 18734.
[47] Z.L. Wang, Z.W. Pan, Z.R. Dai, Microsc. Microanal. 8 (2002) 467.
[48] C. Stampfl, C.G. Van de Walle, Phys. Rev. B 57 (1998) 15052.
[49] T. Murata, I. Yamato, Y. Kakinuma, A.G.W. Leslie, J.E. Walker, Science 308 (2005) 654.
[50] S. Hashimoto, A. Yamaguchi, J. Am. Ceram. Soc. 79 (1996) 1121.
[51] D. Moore, C. Ronning, C. Ma, Z.L. Wang, Chem. Phys. Lett. 385 (2004) 8.
[52] C. Ma, Y. Ding, D. Moore, X.D. Wang, Z.L. Wang, J. Am. Chem. Soc. 126 (2004) 708.
[53] F. Vigue, P. Vennegues, S. Vezian, M. Laugt, J.-P. Faurie, Appl. Phys. Lett. 79 (2001) 194.
[54] Z.L. Wang, X.Y. Kong, J.M. Zuo, Phys. Rev. Lett. 91 (2003) 185502.
[55] E.W. Wong, P.E. Sheehan, C.M. Lieber, Science 277 (1997) 1971.
[56] P. Poncharal, Z.L. Wang, D. Ugarte, W.A. de Heer, Science 283 (1999) 1513.
[57] Z.L. Wang, P. Poncharal, W.A. de Heer, Pure Appl. Chem. 72 (2000) 209.
[58] R.P. Gao, Z.L. Wang, Z.G. Bai, W.A. de Heer, L.M. Dai, M. Gao, Phys. Rev. Lett. 85 (2000) 622.
[59] Z.L. Wang, Z.R. Dai, R.P. Gao, Z.G. Bai, J.L. Gole, Appl. Phys. Lett. 77 (2000) 3349.
[60] L. Meirovich, Elements of Vibration Analysis, 2nd ed., McGraw-Hill, New York, 1986.
[61] X.D. Bai, E.G. Wang, P.X. Gao, Z.L. Wang, Appl. Phys. Lett. 82 (2003) 4806.
[62] J.H. Song, X.D. Wang, E. Riedo, Z.L. Wang, Nano Lett. 5 (2005) 1954.
[63] W.J. Mai, Z.L. Wang, Appl. Phys. Lett. 89 (2006) 073112.
[64] J.P. Salvetat, G.A.D. Briggs, J.M. Bonard, R.R. Bacsa, A.J. Kulik, T. Stockli, N.A. Burnham, L. Forro, Phys. Rev. Lett. 82 (1999) 944.
[65] A. Volodin, M. Ahlskog, E. Seynaeve, C.V. Haesendonck, A. Fonseca, J.B. Nagy, Phys. Rev. Lett. 84 (2000) 3342.
[66] X.D. Bai, P.X. Gao, Z.L. Wang, E.G. Wang, Appl. Phys. Lett. 82 (2003) 4806.
[67] P.X. Gao, W.J. Mai, Z.L. Wang, Nano Lett. 6 (2006) 2536.
[68] H. Qi, C.Y. Wang, J. Liu, Adv. Mater. 15 (2003) 411.
[69] J. Zhou, N.S. Xu, S.Z. Deng, J. Chen, J.C. She, Z.L. Wang, Adv. Mater. 15 (2003) 1835.
[70] X.D. Wang, J. Zhou, C.S. Lao, J.H. Song, N.S. Xu, Z.L. Wang, Adv. Mater. 19 (2007) 1627.
[71] X.D. Wang, Y. Ding, C.J. Summers, Z.L. Wang, J. Phys. Chem. B 108 (2004) 8773.
[72] D.C. Kim, W.S. Han, B.H. Kong, H.K. Cho, C.H. Hong, Phys. B 401–402 (2007) 386.
[73] H. Gao, F. Yan, J. Li, Y. Zeng, J. Wang, J. Phys. D: Appl. Phys. 40 (2007) 3654.
[74] W.I. l Park, G.C. Yi, Adv. Mater. 16 (2004) 87.
[75] X.M. Zhang, M.Y. Lu, Y. Zhang, L.-J. Chen, Z.L. Wang, Adv. Mater., in press.
[76] B. O'Regan, M. Grätzel, Nature 353 (1991) 737.
[77] W.U. Uynh, J.J. Dittmer, A.P. Alivisatos, Science 295 (2002) 2425.
[78] C. Xu, X.D. Wang, Z.L. Wang, submitted for publication.
[79] M. Law, L.E. Green, J.C. Johnson, R. Saykally, P. Yang, Nat. Mater. 4 (2005) 455.
[80] C.S. Lao, M.C. Park, Q. Kuang, Y.L. Deng, A.K. Sood, D.L. Polla, Z.L. Wang, J. Am. Chem. Soc. 129 (2007) 12096.
[81] C. Soci, A. Zhang, B. Xiang, S.A. Dayeh, D.P.R. Aplin, J. Park, X.Y. Bao, Y.H. Lo, D. Wang, Nano Lett. 7 (2007) 1003.
[82] E. Comini, G. Faglia, G. Sberveglieri, Z. Pan, Z.L. Wang, Appl. Phys. Lett. 81 (2002) 1869.
[83] E. Comini, C. Baratto, G. Faglia, M. Ferroni, G. Sberveglieri, J. Phys. D: Appl. Phys. 40 (2007) 7255.
[84] Q. Wan, Q.H. Li, Y.J. Chen, T.H. Wang, X.L. He, J.P. Li, C.L. Lin, Appl. Phys. Lett. 84 (2004) 3654.
[85] Z.Y. Fan, J.G. Lu, Appl. Phys. Lett. 86 (2005) 123510.
[86] L. Liao, H.B. Lu, M. Shuai, J.C. Li, Y.L. Liu, C. Liu, Z.X. Shen, T. Yu, Nanotechnology 19 (2008) 175501.
[87] S.M. Al-Hilli, M. Willander, A. Öst, P. Strålfors, J. Appl. Phys. 102 (2007) 084304.
[88] M. Willander, L.L. Yang, A. Wadeasa, S.U. Ali, M.H. Asif, Q.X. Zhao, O. Nur, J. Mater. Chem. 19 (2009) 1006.
[89] M.H. Zhao, Z.L. Wang, S.X. Mao, Nano Lett. 4 (2004) 587.
[90] Z.L. Wang, Sci. Am. 298 (2008) 82.
[91] Z.L. Wang, Adv. Funct. Mater. 18 (2008) 3553.
[92] Z.L. Wang, J.H. Song, Science 312 (2006) 242.
[93] Z.L. Wang, MRS Bull. 32 (2007) 109.
[94] Y.F. Lin, J.H. Song, D. Yong, S.Y. Lu, Z.L. Wang, Adv. Mater. 20 (2008) 3127.
[95] Y.F. Lin, J.H. Song, D. Yong, Z.L. Wang, S.Y. Lu, Appl. Phys. Lett. 92 (2008) 022105.
[96] M.Y. Lu, J.H. Song, M.P. Lu, C.Y. Lee, L.J. Chen, Z.L. Wang, ACS Nano (2009) published online.
[97] M.P. Lu, J.H. Song, M.Y. Lu, T.C. Chen, L.J. Chen, Z.L. Wang, Nano Lett., published online, doi:10.1021/nl900115y.
[98] X.D. Wang, J.H. Song, J. Liu, Z.L. Wang, Science 316 (2007) 102.
[99] J. Liu, P. Fei, J. Zhou, R. Tummala, Z.L. Wang, Appl. Phys. Lett. 92 (2008) 173105.
[100] R.S. Yang, Y. Qin, L.M. Dai, Z.L. Wang, Appl. Phys. Lett. 94 (2009) 022905.

[101] X.D. Wang, J. Liu, J.H. Song, Z.L. Wang, Nano Lett. 7 (2007) 2475.
[102] S. Xu, Y.G. Wei, J. Liu, R.S. Yang, Z.L. Wang, Nano Lett. 8 (2008) 4027.
[103] P.X. Gao, J.H. Song, J. Liu, Z.L. Wang, Adv. Mater. 19 (2006) 67.
[104] Y. Qin, X.D. Wang, Z.L. Wang, Nature 451 (2008) 809.
[105] R.S. Yang, Y. Qin, L.M. Dai, Z.L. Wang, Nat. Nanotechnol. 4 (2009) 34.
[106] R.S. Yang, Y. Qin, C. Li, G. Zhu, Z.L. Wang, Nano Lett., published online, doi:10.1021/nl803904b.
[107] Chemical and Engineering News, January 15, 2008, p. 46.
[108] Z.L. Wang, Adv. Mater. 19 (2007) 889.
[109] Z.L. Wang, Mater. Today 10 (2007) 20.
[110] G.F. Zheng, F. Patolsky, Y. Cui, W.U. Wang, C.M. Lieber, Nat. Biotechnol. 23 (2005) 1294.
[111] X.D. Wang, J. Zhou, J.H. Song, J. Liu, N.S. Xu, Z.L. Wang, Nano Lett. 6 (2006) 2768.
[112] J.H. He, C.H. Hsin, L.J. Chen, Z.L. Wang, Adv. Mater. 19 (2007) 781.
[113] J. Zhou, P. Fei, Y.D. Gu, W.J. Mai, Y.F. Gao, R.S. Yang, G. Bao, Z.L. Wang, Nano Lett. 8 (2008) 3973.
[114] J. Zhou, Y.D. Gu, P. Fei, W.J. Mai, Y.F. Gao, R.S. Yang, G. Bao, Z.L. Wang, Nano Lett. 8 (2008) 3035.
[115] J. Zhou, N.S. Xu, Z.L. Wang, Adv. Mater. 18 (2006) 2432.
[116] Z. Li, R.S. Yang, M. Yu, F. Bai, C. Li, Z.L. Wang, J. Phys. Chem. C., 112 (2009) 20114.